Université de Lille
Laboratoire de physique des lasers, atomes et molécules (PhLAM)
École doctorale 104: Sciences de la matière, du rayonnement et de l’environnement
(SMRE)

Double clad hollow core fibers for nonlinear micro-endoscopy

A thesis presented for the degree of Doctor of Physics
Defended on the 16th of november 2022 by

Dylan Septier

Defense committee :

Marie-Claire Schanne-Klein	Laboratoire d’optique et de biosciences, Palaiseau	Reviewer
Frédéric Louradour	Institut XLIM, Limoges	Reviewer
Serge Monneret	Institut Fresnel, Marseille	President
Esben Andresen	Laboratoire de physique des lasers, atomes et molécules, Lille	Examiner
Alexandre Kudlinski	Laboratoire de physique des lasers, atomes et molécules, Lille	Co-supervisor
Géraud Bouwmans	Laboratoire de physique des lasers, atomes et molécules, Lille	Co-supervisor
Guillaume Ducourthial	HORIBA Scientific	Invited

Université de Lille
Laboratoire de physique des lasers, atomes et molécules (PhLAM)
École doctorale 104: Sciences de la matière, du rayonnement et de l'environnement (SMRE)

Fibres creuses à double gaine dédiées à la micro-endoscopie non-linéaire

Thèse pour obtenir le diplôme de docteur en Physique
Soutenue le 16 novembre 2022 par

Dylan Septier

Membres du jury :

Marie-Claire Schanne-Klein	Laboratoire d'optique et de biosciences, Palaiseau	Rapporteuse
Frédéric Louradour	Institut XLIM, Limoges	Rapporteur
Serge Monneret	Institut Fresnel, Marseille	Président
Esben Andresen	Laboratoire de physique des lasers, atomes et molécules, Lille	Examinateur
Alexandre Kudlinski	Laboratoire de physique des lasers, atomes et molécules, Lille	Directeur de thèse
Géraud Bouwmans	Laboratoire de physique des lasers, atomes et molécules, Lille	Co-directeur de thèse
Guillaume Ducourthial	HORIBA Scientific	Invité

Double clad hollow core fibers for nonlinear micro-endoscopy

Dylan Septier

Abstract

This thesis presents the development of a highly multimodal flexible nonlinear micro-endoscope. It is based on a negative curvature hollow core fiber, allowing the delivery of ultrashort and intense optical pulses over a wide spectral band without significant temporal nor spectral distortion. A large silica double clad, guiding via a thin layer of low index polymer, surrounds the microstructure and enables the nonlinear signals to be collected and back propagated through the same fiber as the excitation source. The fiber distal tip is functionalized by addition of either a silica bead inserted into its hollow core or a graded index fiber spliced to its endface, allowing to significantly reduce the mode size at the fiber output. Scanning over an area of several hundreds of microns is provided by a doubly resonant piezoelectric tube attached to the fiber tip to create a spiral scan. Along with a fixed objective, it is encased inside a 3 mm large bio-compatible steel tube, making for a compact endoscope head. Endoscopic imaging of biological tissues, including fresh and unlabeled samples, is demonstrated for the first time using three photon excited fluorescence (3PEF), as well as two photon excited fluorescence (2PEF), second (SHG) and third (THG) harmonic generation, and coherent anti-Stokes Raman scattering (CARS). This system is currently commercialized by Lightcore Technologies. A new scheme is also proposed for the separation of excitation and collection signals, based on a hollow-core double clad fiber coupler. Two different glass materials are used, making the fabrication possible, even with a fusion step, without affecting the hollow microstructure. Performances up to 70 % of the currently used scheme are measured, and images of unstained biological tissues are presented to demonstrate its applicability in nonlinear endoscopy.

Fibres creuses à double gaine dédiées à la micro-endoscopie non-linéaire

Dylan Septier

Résumé

Cette thèse présente le développement d'un micro-endoscope non-linéaire flexible et fortement multimodal. Il est basé sur une fibre optique à cœur creux à courbure négative qui rend possible le déport d'impulsions très courtes et intenses pour une gamme étendue de longueurs d'onde, sans distorsion temporelle ni spectrale significative. Une large double gaine de silice, guidant grâce à une fine couche de polymère de bas indice, entoure la microstructure et permet de collecter et contre-propager les signaux non-linéaires par la même fibre que la transmission du signal source. Afin de diminuer grandement la taille du mode en sortie de fibre, son extrémité distale est fonctionnalisée soit par l'insertion d'une bille de silice dans son cœur, soit par la soudure d'une fibre à gradient d'indice. Une surface large de plusieurs centaines de microns est scannée grâce à un tube piezo-électrique doublement résonant attaché à la fibre et donnant lieu à un profil en spirale. En plus d'un micro-objectif, il est inséré dans un tube métallique bio-compatible de 3 mm de large, formant une tête endoscopique compacte. Des images endsocopiques de tissus biologiques, dont des échantillons frais et non marqués, sont démontrées pour la première fois en utilisant la fluorescence par absorption à trois photons (3PEF), mais également la fluorescence par absorption à deux photons (2PEF), la génération de seconde (SHG) ou troisième (THG) harmonique, et la diffusion cohérente Raman anti-Stokes (CARS). Ce système est actuellement en cours de commercialisation par Lightcore Technologies. Une nouvelle méthode de séparation des signaux d'excitation et de collection est également proposée, basée sur un coupleur de fibre creuse à double gaine. L'utilisation de deux verres différents rend la fabrication possible, même avec une étape de fusion, sans affecter la microstructure creuse de la fibre. Des performances jusqu'à 70 % du système utilisé actuellement sont mesurées et des images de tissus biologiques non marqués sont obtenues, démontrant les possibilités d'application pour l'endoscopie non-linéaire.

Remerciements

Je tiens tout d'abord à adresser mes remerciements au CNRS pour son financement, sans quoi ce travail de thèse n'aurait été possible. Je remercie également le directeur du laboratoire PhLAM, Marc Douay puis Cristian Focsa, ainsi que la directrice de l'IRCICA, Nathalie Rolland, pour m'avoir accueilli. Je remercie les membres du jury, Marie-Claire Schanne-Klein, Directrice de recherche au CNRS, Frédéric Louradour, Professeur à l'Université de Limoges, Serge Monneret, Directeur de recherche à l'Université d'Aix-Marseille, Esben Andresen, Maître de conférence à l'Université de Lille, et Guillaume Ducourthial, Ingénieur recherche et développement chez Horiba Scientific, pour avoir accepté d'évaluer ces travaux, et pour les discussions très intéressantes qui en ont découlé.

Un grand merci à Alexandre, pour ton support et ton apprentissage tout au long de ma thèse, ça a été un plaisir d'apprendre à tes côtés. Je garde un très bon souvenir, professionnellement et personnellement, de ses trois années (malgré une pandémie...) et je pense que c'est en grande partie grâce à toi. Merci aussi à Géraud, pour toutes ces discussions très intéressantes qui m'ont beaucoup appris, et toujours ponctuées d'humour.

Je remercie également Damien, Rémi, Arnaud et Sarah sans qui les caractérisations auraient été bien plus compliquées, merci pour votre aide et votre bonne humeur. Merci aussi à Aymeric et Rémy d'avoir partagé votre technique secrète avec moi, votre implication dans le développement des coupleurs a été précieuse. Je remercie également tous les autres collègues, avec qui, à défaut du travail, j'ai partagé de très bons moments, Andrea, Arnaud, Etienne, Jean, Laure, Matteo, Vincent, Zoheir, et bien sûr mes homonymes Eve-Line, Stefano et Thomas. Et un merci en particulier à mon acolyte Guillaume avec qui j'ai eu le plaisir de partager les joies (et pas que...) de la thèse.

Je veux remercier aussi Gaëlle pour tant de discussions intéressantes, grâce à toi j'ai trouvé quelqu'un avec qui partager ma passion pour le métal et les endoscopes, c'était pas gagné ! J'en profite pour souhaiter bon courage et beaucoup de réussite à Eloïse qui nous a rejoint récemment. Je remercie en outre mes collègues de Marseille, de l'Institut Fresnel et de Lightcore, et en particulier Hervé qui m'a beaucoup aidé dans la mise en place du montage d'endoscopie. Je remercie aussi Raoul Torero, Michèle Bastide et Alexandre Barras de m'avoir procuré des échantillons biologiques, et d'avoir pris le temps d'en discuter malgré des communications interdisciplinaires pas toujours simples.

Sur une touche plus personnelle je remercie ma mère de m'avoir donné le goût de la connaissance et de l'accomplissement personnel, c'est grâce à toi si j'en suis là et je ne t'en remercierai jamais assez. Merci aussi à ton mon entourage, mon père, mes frères et

sœurs, qui m'ont toujours soutenu et qui, même s'ils n'ont pas toujours bien compris ce que je faisais, en ont toujours fait la promotion. Enfin je tiens à remercier celle qui me permet de rester serein même quand tout ne va pas bien, qui nous supporte, moi et ma science, depuis maintenant sept ans. Merci pour tout Ameline.

Contents

Introduction

The fast evolution of laser sources initiated the development of nonlinear optics in numerous fields. Concerning biological imaging, nonlinear optical microscopy (NLOM) has emerged in the 1990's [1], and has been the subject of growing interest ever since[2–4]. Ultrashort, typically sub-picosecond, pulses allow to trigger a nonlinear response of the material by reaching high peak power [5], while maintaining a low average power, avoiding photobleaching and damage to the tissue. Because of the high power density required to generate nonlinear effects, a response is inherently localized at the focal spot of the laser. When applied to the imaging field, this localization leads to a higher spatial resolution and an intrinsic optical sectioning. Additionally, typical excitation wavelengths are located in the near infrared (NIR) spectral region, causing a deeper penetration than linear techniques [6]. NLOM also presents a chemical specificity, as a particular electronic or vibrational state can be addressed with a certain nonlinear effect, enabling label-free interrogation of biological tissues.

Several effects can be used individually to image a particular structure or combined in a single multimodal device. The main nonlinear effects are the following : two photon excited fluorescence (2PEF), three photon excited fluorescence (3PEF), second harmonic generation (SHG), third harmonic generation (THG), stimulated Raman scattering (SRS) and coherent anti-Stokes Raman scattering (CARS). Endogenous fluorophores, addressable by one or several of these, are present in various biological tissues. For instance, type I collagen emits a strong SHG signal [7], whereas CH_2 and CH_3 vibrational bonds can be probed using CARS [8], making it a prominent tool for the study of lipids.

Advances in NLOM, and its valuable benefits, granted it an increasing interest as an alternative to traditional histology that could benefit many fields, including early cancer diagnosis [9–11] and neuronal studies [10, 12]. Furthermore, nonlinear imaging effects fulfill all the requirements for *in vivo* analysis. Many clinical situations would benefit from such a probe, for instance during tumor removal surgery. However, NLOM are generally bulky tabletop microscopes, not suited for intraoperative inquiries. To integrate these devices into a miniature endoscope, the main issue is the delivery of high peak power ultrashort pulses in several meter-long optical fibers. Indeed, temporal and spectral broadening occur when propagating in conventional fibers, caused by group velocity dispersion and nonlinear effects respectively. To overcome this drawback, pre-compensation schemes have been employed [13–16], though they make the setup remarkably more complicated, and leads to restrictions on the spectral range of excitation sources. Propagation in air, rather than silica in conventional fibers, would avoid these issues. It was made possible with the rise of hollow core fibers (HCFs) [17], firstly reported with a photonic band gap microstructure. Although, the group velocity dispersion of these fibers is still relatively high, and transmission band too narrow to allow multimodality. Later reports have seen the development of other HCFs, first Kagomé fibers [18, 19], then negative curvature fibers (NCF) [20–22], with wide transmission bands and very low dispersion. Additionally, NLOM miniaturization also requires a scanning mechanism and a collection system that must be integrated in the full scheme to complete the endoscope, as well as a separation instrument for excitation and collection signals.

These issues, particularly concerning the pulse delivery through optical fibers have made difficult the realization endoscopes capable of performing 3PEF because of the high peak power it requires [23–25]. Nevertheless, it provides an improved spatial resolution and imaging depth under the tissue surface, as it was demonstrated in NLOM [26–32].

Chapter 1 briefly describes the nonlinear interactions and different imaging modalities with their respective applications. This description is voluntarily not realized in depth as theoretical matters have already been detailed. Requirements for nonlinear imaging effects generation and miniaturization are then outlined. Particularly, the issues of fiber delivery for short and/or intense pulses is detailed, along with the different reported pre-compensation methods. A state-of-the-art of scanning mechanisms and collection arrangements for nonlinear endoscopy is summarized with attention to their applicability to the desired endoscope scheme.

Chapter 2 is dedicated to the endoscopic hollow core fiber. Design of the fiber microstructure is presented, with simulations to determine the geometrical parameters, providing optimal performances for nonlinear endoscopy applications. A particular attention is given to the transmission bands position, the propagation losses, and the group velocity dispersion. We then depict the fabrication process and full characterization of the fiber, again emphasizing on the transmission properties. Pulse duration measurements are realized as well to ensure no temporal broadening is induced during propagation. Finally, attention is given to the double clad of the fiber, designed to collect the nonlinear signals and propagate them to the proximal end of the fiber.

Chapter 3 describes the endoscope assembly, detailing every element. Two options of distal functionalization of the fiber are proposed, based either on a silica bead or

GRIN lens, to reduce the large optical mode size at the fiber output, leading in term to a resolution enhancement. Correspondingly, two micro-objectives fixed inside the endoscopic head are proposed and specifically chosen to be coupled with each of the functionalization methods mentioned above. Their purpose is to further reduce the spot size and enhance the working distance of the endoscope. A piezoelectric tube is adjoined inside the endoscope head, and its driving signals are detailed, producing an expanding spiral pattern. An active breaking following this expansion, allowing to decrease the acquisition time of each image, is reported as well. Finally, performances of the two endoscope designs are compared against each other to determine the best suited for our requirements.

Chapter 4 provides a comparison of 2PEF and 3PEF imaging, highlighting the improvements in spatial resolution, optical sectioning and signal-to-noise ratio (SNR) provided by 3PEF. The different acquisition parameters, particularly averaging and acquisition rate, are portrayed, including image comparisons. We demonstrate nonlinear imaging of several biological tissues, fixed or fresh and stained or unlabeled, using 2PEF, 3PEF, SHG, THG and CARS to emphasize on the multimodality of the fabricated endoscope.

Chapter 5 investigates the separation of excitation and collection channels, propagating respectively inside the hollow core and silica double clad of the endoscopic fiber. A hollow core double clad fiber coupler design is proposed as a replacement for the dichroic mirror based setup previously used. It provides a simpler and more robust scheme, much more suitable to intraoperative applications. The fabrication process, including fusion of the fibers is achieved by combining a borosilicate glass multimode fiber to the silica double clad hollow core fiber. Afterwards, we adjust the coupler parameters with successive fabrication and characterization until optimal performances are attained. We assemble a full endoscope on the fabricated coupler and demonstrate 2PEF and SHG imaging, even on unlabeled biological tissues.

Chapter 1

Nonlinear optical endoscopy (NLOE)

Nowadays, microscopes are widely used across the world, and have become as common as they are necessary, especially in the biological field. The study of living cells is strongly dependent on imaging through optical microscopes and their performances, but applying classical microscopy techniques to the investigation of their dynamic behavior is not a straightforward process. Therefore, live imaging systems have emerged to be of high importance. Although linear imaging is still the most common technique, nonlinear optical microscopy (NLOM), since its first implementation in 1990 [1], has grown in popularity for its numerous advantages including deep tissue penetration, high resolution, fast scanning, label-free, and quantitative dynamic imaging of biological tissues. Moreover, different nonlinear microscopy techniques can be implemented in a single setup enabling to simultaneously image different structures inside a biological tissue in a so-called multimodal microscope. Nevertheless, applying NLOM to *in-vivo* imaging presents a major drawback as these nonlinear imaging setups are bulky tabletop microscopes, not suited for intraoperative measurements.

Fiber-based endoscopes, with light sent through an optical fiber, has been widely used in medical diagnosis since its first realization in 1958 [33]. The ideal solution in implementing NLOM setups to real-time *in-vivo* imaging lies in these endoscopic techniques, keeping bulky optics at the proximal end of the fiber and leaving the distal end free of movements to be used as a portable probe. However, nonlinear signal generation requires high intensity excitation. Therefore, the endoscope must be able to deliver high power ultrashort pulses which is not compatible with classical fibers. An overview of the different nonlinear processes that can be combined in a multimodal NLOM will be presented in the first part of this chapter. The second part will present the major issues in the propagation of high power short pulses in optical fibers. The third part will introduce the requirements to miniaturize microscopy setups into flexible micro-endoscopes.

1.1 Nonlinear imaging

1.1.1 Nonlinear light/matter interaction

To understand the basics of nonlinear light/matter interaction, we will henceforth consider the materials to be isotropic. For a simple description, it is sufficient to simplify the medium as made of positive and negative charges (ions and electrons respectively). When an electric field $\overrightarrow{E}$ propagates in the medium, ions move in a direction and electrons move in the opposite one, thus creating a dipolar moment. It is defined at the atomic level by $\overrightarrow{p} = \alpha \overrightarrow{E}$ where α is the polarizability, and at the macroscopic level by the electric polarization:

$$\overrightarrow{P} = \epsilon_0 \chi \overrightarrow{E} \tag{1.1}$$

where $\chi = N\alpha$ is the susceptibility of the medium, N the number of polarizable atoms per unit of volume, and ϵ_0 the dielectric permittivity.

When sending an electric field to a dielectric medium, the reaction will become nonlinear providing the electric field reaches a non-negligible value compared to the inter-atomic field[1]. To achieve this, lasers delivering pulses with a duration under the picosecond range (*i.e.* sub-ps pulses) have been used as it increases the peak power by orders of magnitude compared to a continuous wave with the same average power. To take into account the different orders of nonlinearity, the polarization of the medium $P(t)$ can be expanded as a Taylor series of the electric field $E(t)$:

$$P(t) = \epsilon_0(\chi^{(1)}E(t) + \chi^{(2)}E^2(t) + \chi^{(3)}E^3(t) + ...) = P_\mathrm{L}(t) + P_\mathrm{NL}(t) \tag{1.2}$$

where $\chi^{(1)}$ is the linear susceptibility, $\chi^{(2)}$ and $\chi^{(3)}$ are the second and third order susceptibility and so on. The polarization $P(t)$ can then be broken down into linear and nonlinear polarization terms as followed:

$$P_\mathrm{L}(t) = \epsilon_0 \chi^{(1)} E(t) \tag{1.3a}$$

$$P_\mathrm{NL}(t) = \epsilon_0(\chi^{(2)}E^2(t) + \chi^{(3)}E^3(t) + ...) \tag{1.3b}$$

It should be noted that the polarization and electric field are here taken as scalar quantities for a simpler description, but a full vectorial description is possible for a deeper investigation [5].

---

[1] Typically about $10^9 - 10^{10}$ V/m in glasses.

The nonlinear effects can be separated into two categories :

- **Parametric effects** refer to nonlinear effects for which the final electronic state is identical to the initial one. The emission frequency for effects used in imaging is a multiple of the excitation frequency.
- **Non-parametric effects** refer to nonlinear interactions for which the final electronic state is different from the initial one. The emission frequency is not a multiple of the excitation frequency. Non-parametric effects need to be described using a complex susceptibility [5]. For example, the third order susceptibility can be expressed has :
$$\chi^{(3)}(\omega) = Re\{\chi^{(3)}(\omega)\} + i\ Im\{\chi^{(3)}(\omega)\} \tag{1.4}$$

Finally, it is important to note that all even orders of the nonlinear susceptibility are rendered null in materials presenting an inversion symmetry because all the microscopic contributions compensate each other at the macroscopic level. As a result, some effects, like second harmonic generation (SHG) for example, can only occur in non-centrosymmetric media.

1.1.2 Nonlinear fluorescence

The nonlinear fluorescence mechanisms are triggered by the simultaneous[2] interaction of two or three photons with a molecule, usually done with a single excitation laser source (*i.e.* photons then have the same energy).

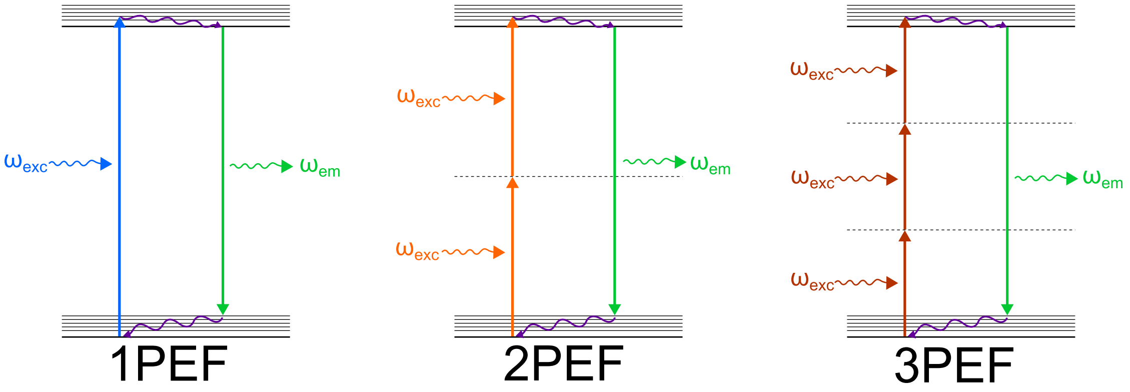

Figure 1.1: *Molecular energy diagrams for fluorescence processes: one (1PEF), two (2PEF) and three (3PEF) photon excited fluorescence.*

---

[2] For a quantum interaction, this means over a period of a fraction of femtoseconds ($< 10^{-15}$ s). Over this period, the molecule can be in a virtual state (i.e. not an eigenstate) because of Heisenberg uncertainty between time and energy.

Figure 1.1 is a schematic representation of the nonlinear fluorescence processes, two (2PEF) and three (3PEF) photon excited fluorescence, compared to the linear one, one photon excited fluorescence (1PEF). After absorption of the photons, the molecule is in an excited eigenstate with many vibrational levels. Afterwards, a part of the energy is transferred to the medium through vibrational relaxation, then the molecule returns to the ground state, emitting a single fluorescence photon. As a result, the fluorescence emission energy has to be smaller than the sum of the absorbed photons because some of it is lost to non-radiative transitions. It causes a spectral shift between the absorption and emission spectra, known as Stokes shift. For a more in depth analysis, the full quantum description was done by Maria Göppert-Mayer in her PhD thesis in 1931 [34].

2PEF is an absorption effect, dependent on the resonant transitions of the material, thus described by the third order nonlinear susceptibility $\chi^{(3)}$, whereas 3PEF originates from $\chi^{(5)}$. Because non-radiative transitions are involved, 2PEF and 3PEF are non-parametric effects, arising from the imaginary part of the nonlinear susceptibility.

The probability of 2PEF and 3PEF to happen is very low in ambient light conditions, hence a very high photon flux is needed on the sample to generate a strong nonlinear fluorescence signal. This condition is fulfilled using a pulsed femtosecond laser tightly focused, which enhances the efficiency by a factor of $\frac{1}{\tau f_{\text{rep}}}$, where τ is the pulse duration and f_{rep} is the repetition rate, compared to a continuous wave (CW) with the same average power. As an example, for the same average power, a pulsed excitation laser with a pulse duration of $\tau = 100$ fs and a repetition rate of $f_R = 100$ MHz will increase the nonlinear fluorescence signal generation by a factor of 10^5 as compared to a CW.

Nowadays, 2PEF is widely used because a lot of fluorescent probes can be excited by this effect. In fact, one major advantage of this technique is that it can exploit the same fluorophores used in confocal microscopy, which makes its implementation a lot easier. In addition, there is a variety of endogenous fluorophores that can be probed using nonlinear fluorescence: elastin, keratine, flavoproteines, NAD(P)H, neurotransmitters [35, 36]. These are naturally present in tissues which makes it possible to image cells without the need to add an exogenous fluorophore to the sample, potentially disturbing its physiology.

1.1.3 Sum frequency

Second (SHG) and third (THG) harmonic generation, like nonlinear fluorescence, are instantaneous scattering processes and can be excited by a single laser source. Nonetheless, they are very different procedures: SHG and THG are parametric processes, which means that the initial and final quantum states are the same. The photons energy and momentum are conserved, hence no energy is transferred to the material. Moreover, sum frequency generation is solely mediated by virtual states.

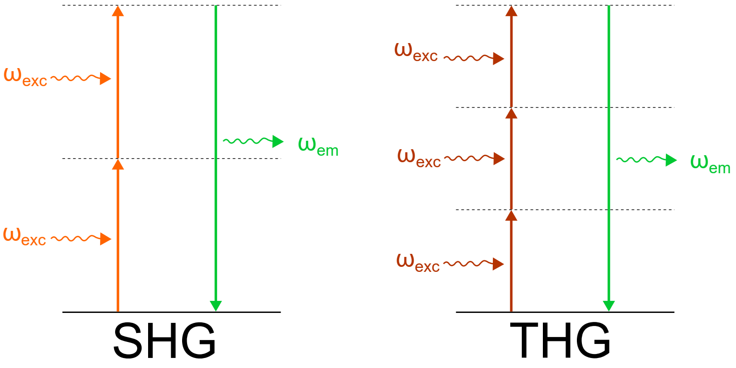

Figure 1.2: *Molecular energy diagrams for sum frequency processes: second (SHG) and third (THG) harmonic generation.*

As stated before, because the physical origin of SHG lies in the real part of the second order susceptibility $\chi^{(2)}$, it consequently happens only in materials without inversion symmetry. THG, however originates from the real part of the third order susceptibility $\chi^{(3)}$.

The mechanism behind SHG and THG is schematically represented on the energy diagrams of figure 1.2. Two or three photons of the same energy, represented by their frequency ω_{exc}, are annihilated to generate a photon of energy $\omega_{\text{em}} = 2\,\omega_{\text{exc}}$ (SHG) or $\omega_{\text{em}} = 3\,\omega_{\text{exc}}$ (THG).

Some strong SHG emitters are naturally present in biological tissues, notably: collagen fibrils [7, 37], myosin heads in muscle [38] and microtubules [39]. This makes SHG imaging a very interesting feature to have in a multimodal nonlinear imaging setup. On the other hand, THG is often used in the investigation of cell membranes [40, 41], because THG is useful to image heterogeneities at a micrometer scale.

1.1.4 Vibrational imaging

Vibrational imaging is based on the molecular vibrations happening when atoms, attached to each other by molecular bonds, oscillate in periodic and synchronous manner. This oscillation can be simplified as a one dimension harmonic oscillator of masses held together by springs [8]. Consequently, each chemical bond has a characteristic resonance frequency that depends on the atoms involved and the environment (equivalent to the spring constant).

Spontaneous Raman scattering

Sending visible or near-infrared (NIR) light on a material can spontaneously generate two different scattering processes: Rayleigh and Raman scattering. Both are schematically represented on the molecular energy diagrams of figure 1.3 (a).

Rayleigh scattering: When photons are penetrating a medium made of molecules whose size is much smaller than the wavelength associated with these photons, they will keep their energy but their direction of propagation will be altered. The unchanged energy, and therefore frequency, of the incoming photons causes this process to be called elastic. Consequently, Rayleigh scattering induces scattering of photons in all directions but with unchanged frequency.

Raman scattering: Conversely, Raman scattering is an inelastic process, as the photon energy changes upon interaction with the medium. This is caused by an energy transfer from the medium to the scattered photon, or from the incoming photon to the medium (*i.e.* scattered light is blueshifted or redshifted respectively). Considering a specific molecular bond of resonance frequency Ω_R, the frequency of an incoming photon ω can be changed to:

$$\omega_S = \omega - \Omega_R \qquad \text{(Stokes)} \tag{1.5a}$$

$$\omega_{AS} = \omega + \Omega_R \qquad \text{(Anti-Stokes)} \tag{1.5b}$$

As schematically presented in the figure 1.3 (b), the Stokes process will cause the scattered photons to be redshifted, whereas the anti-Stokes photons will be blueshifted. Because of the Ω_R gap difference between excitation and emission frequencies, Raman scattering is a non-parametric process, and derives from the imaginary part of the third order nonlinear susceptibility $\chi^{(3)}$.

In principle, both Stokes and anti-Stokes scattering have the same efficiency. Moreover, because of the Boltzmann distribution, the probability for a particle to be in a state of energy E is proportional to $e^{\frac{-E}{k_\mathrm{B}T}}$, where k_B is the Boltzmann constant and T is the temperature. Hence, at room temperature, almost all population is on the fundamental level because $k_\mathrm{B}T$ is much smaller than the energy needed for the molecule to be on the vibrational excited state, starting point for the anti-Stokes scattering process. For this reason, the anti-Stokes process is far less probable to happen than the Stokes one. In fact, spontaneous processes have a low efficiency compared to Rayleigh scattering. For example, Raman scattering has a cross-section[3] 14 orders of magnitude lower than the fluorescence one [35, 42], and only one out of 10^5 photons will be back-scattered, making it hardly applicable for microscopy. Using coherent Raman scattering instead

---

[3] Probability for a process to happen upon interaction.

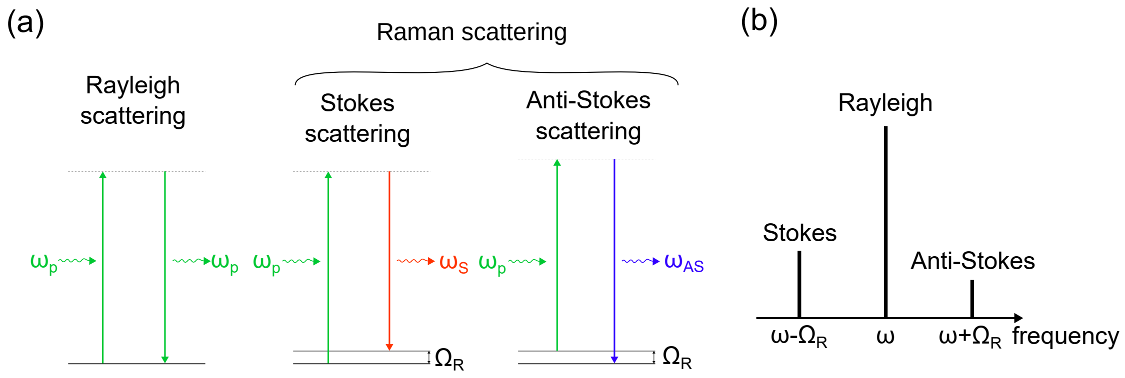

Figure 1.3: *(a) Molecular energy diagrams for Rayleigh and Raman scattering. (b) Schematic representation of the scattered photons energy.*

will present the advantages of greatly improving the efficiency as well as allowing to probe a specific molecular bond.

Coherent Raman scattering

Unlike the spontaneous processes, in coherent Raman scattering (CRS), two laser beams, at two different frequencies, are sent to the medium: they are typically called pump and Stokes, with frequencies ω_P and ω_S respectively. These beams will interfere and produce a beating at frequency $\Omega = \omega_\mathrm{P} - \omega_\mathrm{S}$. If it matches the resonant frequency of a molecular bond (*i.e.* $\Omega = \Omega_\mathrm{R}$), then the vibration of this bond will be greatly enhanced compared to other ones. Moreover, if light is sent to the sample in a coherent fashion, all bonds identical to this one will oscillate in phase, enhancing even more the scattered light. Using this method for microscopic purposes can improve cross-section by 6 orders of magnitude compared to spontaneous Raman scattering [42]. CRS leads to the creation of new fields, originating from the nonlinear polarization induced by interaction of the pump and Stokes fields with the material nonlinear third order susceptibility $\chi^{(3)}$ [8]. The four major CRS processes and the associated frequencies are the following:

SRL (Stimulated Raman loss) $\omega_S = \omega_P - \Omega_R$ (1.6a)

SRG (Stimulated Raman gain) $\omega_P = \omega_S + \Omega_R$ (1.6b)

CARS (Coherent anti-Stokes Raman scattering) $\omega_{AS} = \omega_P + \Omega_R = 2\,\omega_P - \omega_S$ (1.6c)

CSRS (Coherent Stokes Raman scattering) $\omega_{CS} = \omega_S - \Omega_R = 2\,\omega_S - \omega_P$ (1.6d)

The firs two processes generate fields that interfere with incident ones (pump and Stokes), and leading either to a depletion of the pump beam, called stimulated Raman

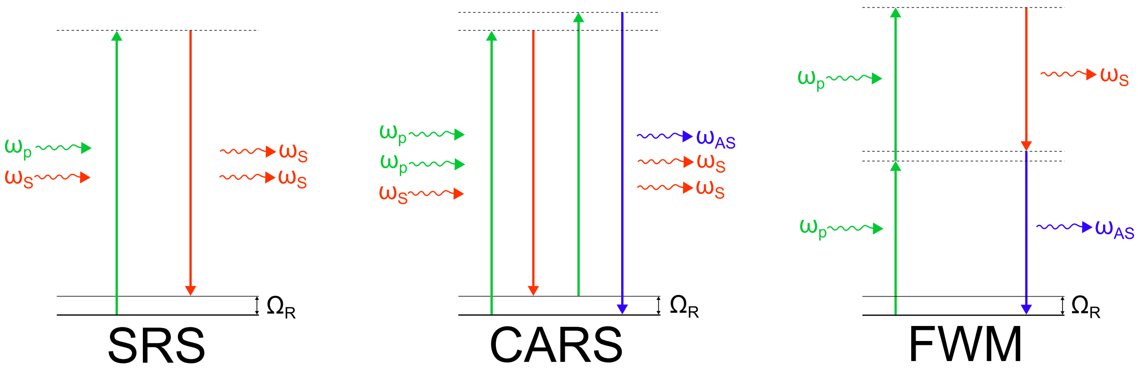

Figure 1.4: *Molecular energy diagrams for coherent Raman scattering: stimulated Raman scattering (SRS), coherent anti-Stokes Raman scattering (CARS), and four wave mixing (FWM)*

loss (SRL), or a gain in the Stokes beam, called stimulated Raman gain (SRG), and are grouped under the appellation of stimulated Raman scattering (SRS). The third process presented in equation 1.6 induces the creation of an anti-Stokes radiation and is therefore called coherent anti-Stokes Raman scattering (CARS). SRS and CARS molecular energy diagrams are presented in the figure 1.4. Finally, the fourth process, coherent Stokes Raman scattering (CSRS), is rarely used in imaging applications because the scattered radiation is redshifted with respect to the excitation beams. The emission would then usually be in the NIR, away from the spectral window where most signals are detected in such a multimodal imaging setup (around 400 to 700 nm), and where detectors are less sensitive. This process will consequently not be investigated further here.

CARS can be applied to spectroscopy by changing the frequency of one of the excitation fields over a certain spectral range, thus scanning the vibrational spectrum of molecules. On the other hand, CARS can also be used in microscopy by tuning the frequency difference between pump and Stokes so that it matches the resonant frequency of a targeted molecular bond. The vibration then generates the observed signal, forming a map of the target inside the sample.

It is important to mention that the four waves involved in CARS can also be arranged to form a different process called four wave mixing (FWM) [43], also represented in figure 1.4. This non-resonant mechanism limits the contrast of CARS, and different schemes for limiting the parasitic FWM background have been proposed [44–47].

SRS has ever since been investigated for vibrational imaging applications free of non-resonant background. The principle is to detect the intensity variation in the pump or Stokes beam after interaction with the material. This energy variation comes from the interference of the newly generated fields with the excitation ones.

1.1.5 Nonlinear optical microscopy (NLOM)

Figure 1.5 (a) shows a typical setup scheme to realize nonlinear imaging. Because the targeted processes require a simultaneous interaction of multiple photons, the probability for it to happen is quite low. Consequently, a high peak power[4] is required to reach an emission comparable to linear imaging. In practice, this level is achieved with femtosecond pulsed lasers, as shorter pulses increase the peak power while maintaining the pulse energy. This excitation beam is then tightly focused onto the sample using a microscope objective, also used to collect the nonlinear signal that is either generated backwards or scattered inside the sample to propagate in this direction.

Because the excitation wavelengths are in the near infrared (NIR)[5] and the collection

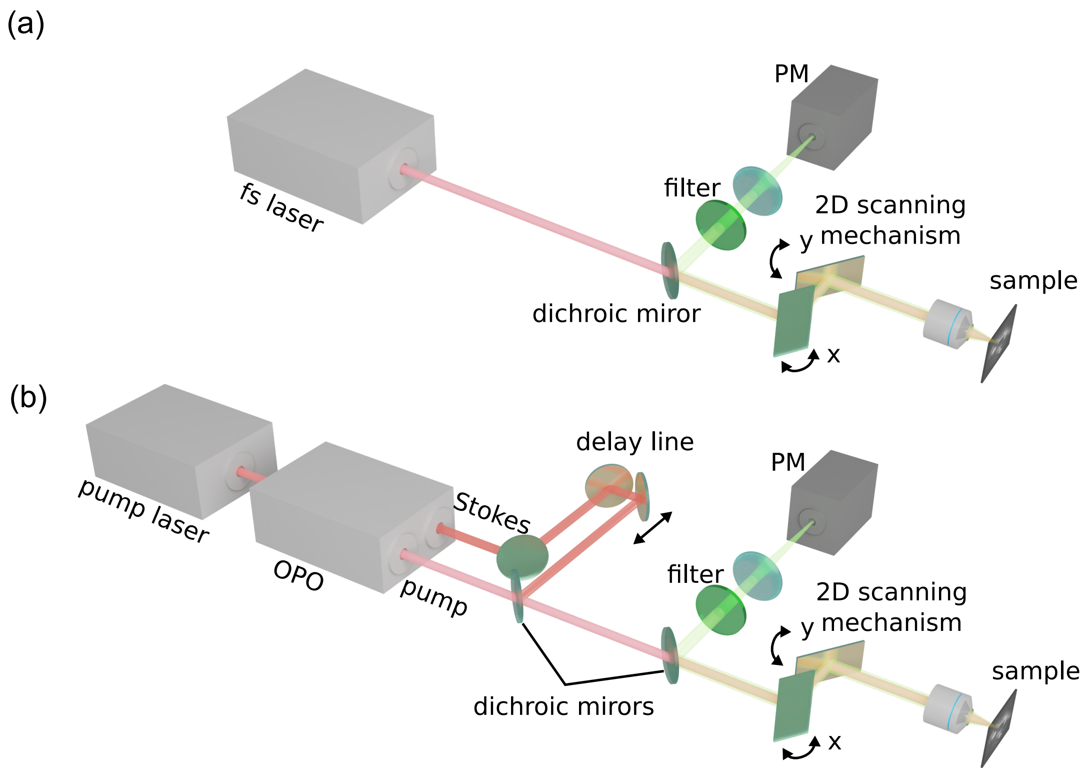

Figure 1.5: *Typical NLOM setup for (a) multiphoton and (b) vibrational imaging. Multiphoton imaging is generally realized using a femtosecond (fs) Titanium-Sapphire (Ti:Sa) laser. Vibrational imaging usually involves a picosecond (ps) or femtosecond (fs) pump laser with an optical parametric oscillator (OPO) to generate the Stokes beam.*

---

[4] Typically in the range of $10^3 - 10^5$ W

[5] Typically in the range of 800 – 2000 nm

ones in the visible range[6], they can be separated using a dichroic mirror. The nonlinear signal collected is then sent to a detection channel with appropriate filters to insure only the targeted effect is detected. It is noteworthy to mention that different effects can be generated using the same excitation signal, and detected simultaneously by cascading dichroic mirrors and duplicating the detection channel.

Moreover, a two-dimensional scanning mechanism, for instance two galvo mirrors set on orthogonally oriented rotation motors as represented in figure 1.5 (a), must be added for the focused excitation spot to probe the sample and obtain an image.

Finally, to perform vibrational imaging, two excitation beams, pump and Stokes, must be delivered and spatially overlapped with an appropriate dichroic mirror, as shown in figure 1.5 (b). Pump and Stokes pulses are then temporally overlapped by adding a delay line on one of the beams paths.

1.1.6 Applications

Currently, the typical protocol in cancer diagnosis involves a preparation phase during which the biological tissue is extracted and prepared in thin slices in order to be observed using conventional microscopy techniques. These biopsies present a non-negligible risk and can cause damage to surrounding tissues, especially in the case of neurological interventions. Moreover, getting histology samples prepared for observation is a time demanding procedure. Conventionally, it takes up to several hours of preparation before a pathologist can examine the sample.

Besides, tumor removal is a very delicate surgery act, and it is essential to locate tumor margins, as failure in complete removal is one of the main causes for cancer recurrence in patients [2]. In this direction, multiphoton microscopy appears as a very promising technique for cancer diagnosis in what is now called multiphoton histopathology. Indeed, it allows label free imaging with chemical specificity. In addition, the multimodality enables the simultaneous observation of different tissue components.

Even for label free imaging, typical fluorophores serve as a reference for absorption wavelengths commonly found in microscopy. In this scope, absorption and emission spectrum of GFP (green) and mCherry (red) are represented in figure 1.6 (a). It illustrates why 2PEF imaging is often performed in the green spectral range with an excitation at 920 nm. Likewise, 3PEF imaging is commonly achieved with excitation at 1300 nm and 1700 nm in the green and red spectral ranges respectively. Moreover, these wavelengths take advantage of a compromise between water absorption and tissue scattering[6], allowing to increase 3PEF imaging depth.

---

[6] Typically in the range of 400 – 700 nm

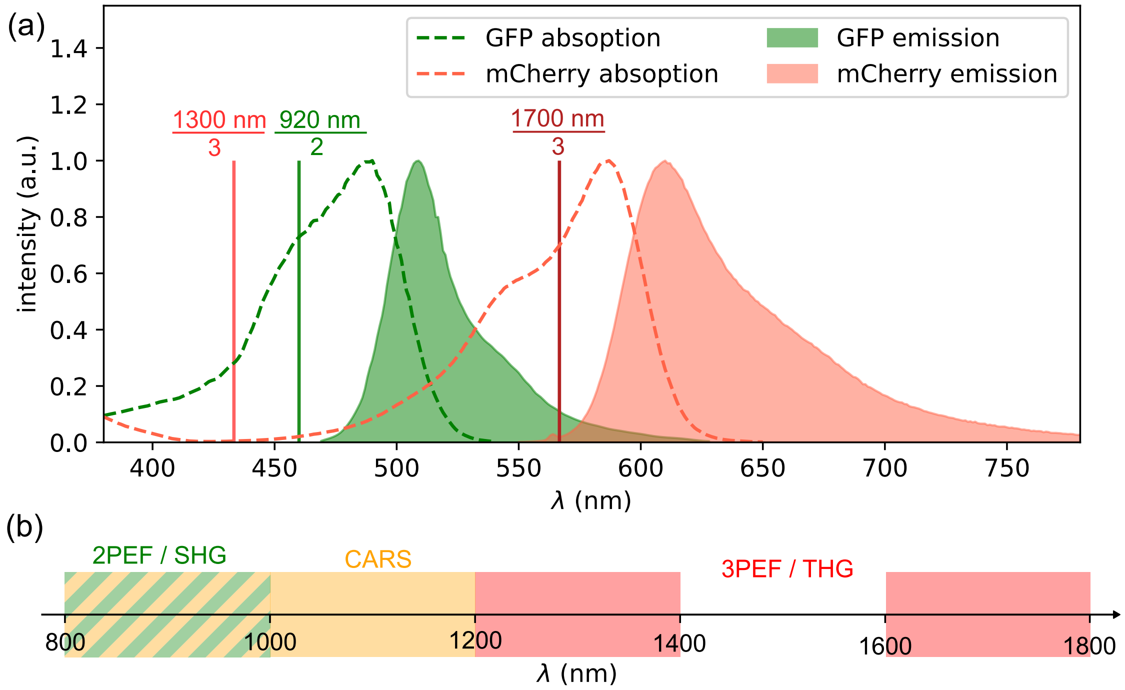

Figure 1.6: *(a) Absorption (dashed curves) and emission (filled curves) spectra of a green fluorescent protein (GFP, green) and mCherry protein (red), using data from [48]. Vertical lines represent the corresponding wavelengths for 2PEF at* $\lambda_{\mathrm{exc}} = 920$ *nm (green), and 3PEF at* $\lambda_{\mathrm{exc}} = 1300$ *nm (light red) and* $\lambda_{\mathrm{exc}} = 1700$ *nm (dark red). (b) Commonly used excitation wavelength ranges for the different nonlinear effects.*

A schematic representation of typical excitation spectral ranges for most nonlinear imaging effects is provided in figure 1.6 (b). For reasons stated above, 2PEF as well as SHG will be targeted with excitation wavelengths in the range of 800 – 1000 nm, whereas excitation for 3PEF and THG will be in the range of 1200 – 1400 nm and 1600 – 1800 nm. For CARS imaging, it is common to target CH_2 and CH_3 vibrational bonds, with an energy around 2850 cm^{-1}, which is accomplished with excitation wavelengths in the range of 800 – 1000 nm for the pump and 1000 – 1200 nm for the Stokes.

1.2 Pulse delivery with optical fibers

Although NLOM presents a lot of advantages, its implementation for *in-vivo* imaging remains challenging because of microscopes bulky size. To avoid the tissue extraction step before imaging, optical fibers have been added to the setups, simplifying the schemes and allowing its excitation end to be moved freely. For this to be possible, the fiber used must be able to deliver sub-picosecond pulses onto the biological sample under study.

The following sections present a description of typical optical fibers and their properties, with a focus on the temporal and spectral shape of a pulse during propagation.

1.2.1 Guidance mechanism

The fairly straightforward aim of an optical waveguide to bring light from one point in space to another has found many applications over the years, rendering it an essential tool in many scientific fields. Guided light propagation presents numerous advantages when compared to free space propagation, including a protected path of light, a possible long distance propagation, particularly important for telecommunication applications, avoidance of diffraction problems over such distances, and possible mechanical flexibility. Many waveguides can be created, although the most common form is the optical fiber, a cylindrical dielectric structure inside which light can propagate at optical frequencies.

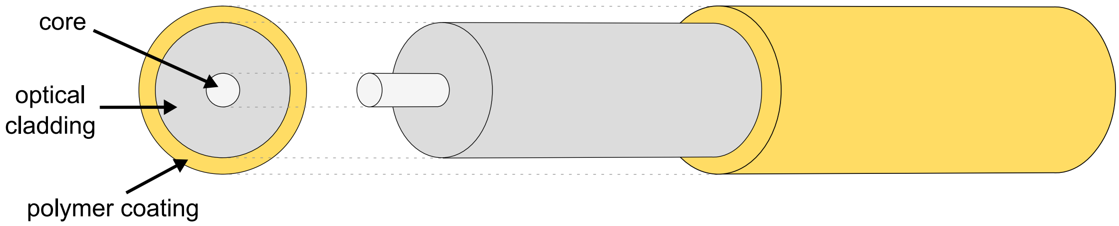

Figure 1.7: *Schematic representation of a typical optical fiber structure. The optical cladding is designed to confine light inside the fiber core, whereas the polymer coating protects the fiber from any outside activity.*

The typical design of an optical fiber is presented in figure 1.7. Most of the light is confined inside the fiber core, which can be solid or hollow, under the effect of total internal reflection (TIR), modified TIR (MTIR), photonic bandgap (PBG), or inhibited coupling (IC), depending on the fiber type. To create such effects, an optical cladding is present around the core, and can either be a simple homogeneous material or a more or less complex two-dimensional microstructure. For mechanical protection and flexibility of the fiber, another cladding layer, usually a polymer coating, is added to the arrangement.

From the diversity of applications, telecommunication is surely the most common one, with a mass production of optical fibers across the globe, but many others have arisen such as powerful light transmission, lasers and amplifiers, medical imaging, sensing, and even entertainment.

Conventional fibers refer to optical fibers guiding light through the simplest and

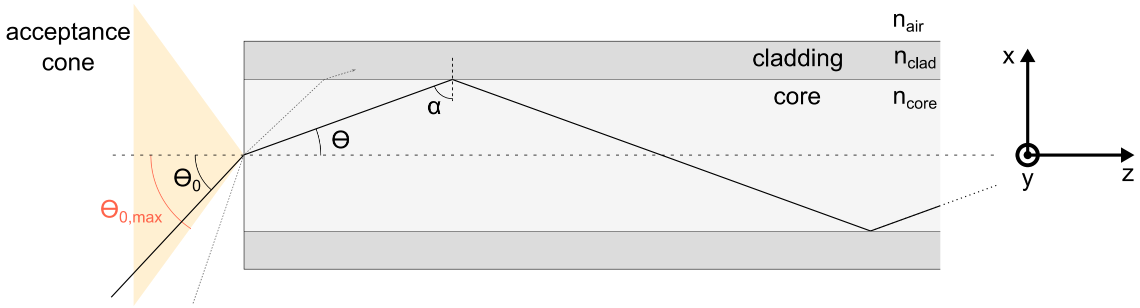

Figure 1.8: *Geometrical representation of light propagation inside a conventional fiber (via total internal reflection). For an incident angle included in the acceptance cone, light will be reflected at the core/cladding interface. If the incident angle is not inside this cone, most of the energy will be refracted at the interface and light will quickly dissipate inside the cladding.*

most common guiding mechanism: total internal reflection (TIR). These fibers also have the simplest geometrical structure, with a high index solid core and a homogeneous material for the optical cladding. Two different approaches allow us to understand the underlying principles of light guiding: first the geometrical approach, although not always relevant, allows to form a mental image of the guidance mechanism, then the electromagnetic approach brings a more rigorous and complete description.

Geometrical approach

The notion of ray optics can be an appropriate way to describe light propagation inside an optical fiber only when the core size is much larger than the wavelength of interest. Otherwise, the use of optical rays is completely irrelevant.

The most common fiber structure is called step-index fiber. Its core and cladding have a uniform refractive index and the structure presents a discontinuous index profile. The vast majority of fibers are made of silica (amorphous silicon dioxide S_iO_2) with dopants added to the core material to slightly increase its refractive index. The index difference between the core (n_{core}) and cladding (n_{clad}) is then usually very low (*i.e.* $n_{\text{core}} - n_{\text{clad}} << n_{\text{core}}$).

Figure 1.8 represents the confinement of light by total reflection at every core-cladding interface. Therefore, two conditions arise from Snell's law:

$$n_{\text{core}} > n_{\text{clad}} \tag{1.7a}$$

$$\alpha > \alpha_{\text{min}} = sin^{-1}(\frac{n_{\text{clad}}}{n_{\text{core}}}) \tag{1.7b}$$

where α is the angle between the optical ray and the normal to the core-cladding interface, and α_{min} is its minimum value to provide total internal reflection. The first condition is fulfilled by doping the silica core using a dopant that raises the refractive index. For example, germanium is commonly used for that purpose. For the second condition to be met, as evidenced by figure 1.8, the incident ray at the input of the fiber has to be contained inside an acceptance cone defined by the condition:

$$\theta < \theta_{\text{max}} = \frac{\pi}{2} - \alpha_{\text{min}} \tag{1.8}$$

where θ is the angle between the ray and the normal to the core / cladding interface, and θ_{max} is the maximal value for which there is still total reflection. For an incident ray outside this cone, light will then leak to the cladding by refraction. Using these conditions, the acceptance cone will define the numerical aperture (NA) of the fiber by

$$\text{NA} = n_{\text{air}} \sin(\theta_{0,\text{max}}) = \sqrt{n_{\text{core}}^2 - n_{\text{clad}}^2} \tag{1.9}$$

Electromagnetic approach

To fully understand the propagation of light inside an optical fiber, the need to use the electromagnetic theory of light and solve Maxwell's equations becomes necessary. In this context, we define the propagation constant $\beta = n_{\text{core}}\, k_0 \cos(\theta)$ as the projection of the wave vector $|\vec{k}| = k = n_{\text{core}}\, k_0 = n_{\text{core}}\, \frac{2\pi}{\lambda_0}$ on the propagation axis z, where θ is the angle between these two, whereas k_0 and λ_0 are the wavenumber and wavelength in vacuum respectively.

Using this, we can define different types of modes depending on the propagation constant:

- **Guided modes** correspond to light that remains confined inside the fiber core throughout the propagation. In this case, the number of modes guided inside the fiber core is finite. As we have seen, guided modes follow the condition $0 < \theta < \theta_{\text{max}} = \frac{\pi}{2}\ \alpha_{\text{min}}$ (see figure 1.8), which translates to a condition on the propagation constant:

  $$n_{\text{clad}}\, k_0 < \beta < n_{\text{core}}\, k_0 \tag{1.10}$$

  From equation 1.10 we can see that it becomes relevant to define an effective index specific to the mode as

  $$n_{\text{eff}} = \frac{\beta}{k_0} \tag{1.11}$$

  The condition for guided modes then becomes

  $$n_{\text{clad}} < n_{\text{eff}} < n_{\text{core}} \tag{1.12}$$

- **Cladding modes** propagate inside the cladding and find their origin in incident light outside the acceptance cone then refracted at the core-cladding interface. These modes have an effective index lower than the cladding index:

  $$0 \leqslant n_{\text{eff}} < n_{\text{clad}} \tag{1.13}$$

  At this point, reflection is only partial (*i.e.* there is no more TIR) and the resonance condition is not necessary. Therefore, n_{eff} can take every value hence the term continuum of radiation modes.

  Generally, these modes are of no interest, hence the polymer coating outside the cladding is chosen with a refractive index higher than silica. Thus, its purpose is not only mechanical but also optical, to discard these modes by leaking them out of the cladding.

1.2.2 Optical fiber properties

When describing the characteristics of an optical fiber, it is conventional to introduce the V parameter, called normalized frequency and defined as

$$V = \frac{2\pi a}{\lambda_0}\sqrt{n_{\text{core}}^2 - n_{\text{clad}}^2} \tag{1.14}$$

where a is the radius of the fiber core. The guided mode with the highest effective index n_{eff} (*i.e.* closest to n_{core}) is called fundamental mode (FM) and is always present in an optical fiber. Then higher order modes (HOM) will appear with decreasing n_{eff} until $n_{\text{eff}} = n_{\text{clad}}$ from where all higher modes are cut off. This will depend on the value of V. For example, for a step index fiber, the first HOM's cut-off frequency is $V_c = 2.405$. Under this value, only the FM is present, and the fiber is then called singlemode. Otherwise, the fiber is multimode. During propagation in an optical fiber (along the direction z), the power $P(z)$ will inevitably decrease as followed :

$$P(z) = P(0)\exp(-\int_0^z \alpha'(z)\,dz) \tag{1.15}$$

where $P(0)$ is the input power, and $\alpha'(z)$ is the attenuation linear coefficient, expressed in [m^{-1}]. It measures the amount of light power lost during propagation between input and output of the fiber. However, it is convenient to express the fiber attenuation in [dB/km]. Therefore, and assuming the losses are evenly distributed, the loss coefficient is generally expressed as :

$$\alpha(\text{dB/km}) = -\frac{10}{L(\text{km})}\log_{10}(\frac{P(L)}{P(0)}) \tag{1.16}$$

where L is the propagation length, $P(0)$ and $P(L)$ are the input and output power respectively. Losses in optical fibers can have many origins, and from the perspective of a user, it is common to separate them into the following categories:

- **Intrinsic losses** are caused by the fiber material and/or structure, and can be due to absorption, scattering or material inhomogeneity.
- **Extrinsic losses** arise from sources outside the fiber and can theoretically be avoided. For instance, origin can be bending of the fiber, splice between fibers or impurities at the endface of the fiber.

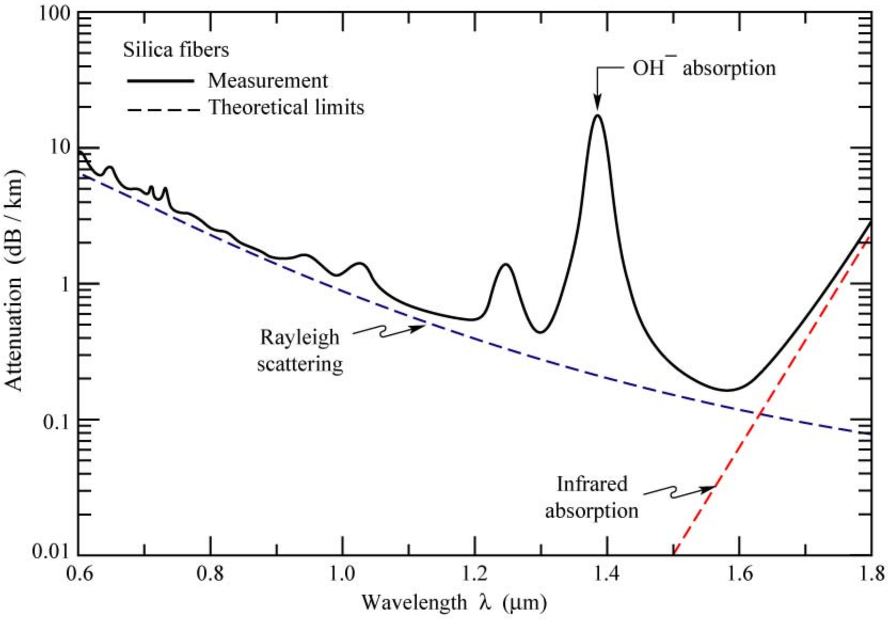

Figure 1.9: *Measured attenuation of silica fibers (solid line) compared with theoretical limits from Rayleigh scattering (dashed blue line) and infrared absorption (dashed red line), taken from [49].*

The ease of fabrication for low loss singlemode propagation in all-solid fibers guiding via TIR makes it the most widely used today, especially in telecommunications. Figure 1.9 shows the typical loss spectrum of an optical fiber used in telecommunication. $\lambda = 1550$ nm is the most commonly used wavelength because it offers the best compromise between Rayleigh scattering and infrared (IR) absorption caused by molecular vibrations, with a record loss of about 0.14 dB/km [50]. However, when short and/or intense pulses propagate in such a fiber, other effects can emerge and affect their shape.

1.2.3 Group velocity dispersion (GVD)

Group velocity dispersion (GVD) is a linear effect arising from the dependence of the group velocity v_g[7] with the wavelength. Consequently, the different spectral components of the optical pulse will propagate at different velocities, eventually inducing a temporal broadening of the optical pulse. GVD is generally described by the following parameter, expressed in [s^2/m]:

$$\beta_2 = \frac{d^2}{d\omega^2}\beta = \frac{d}{d\omega}\frac{1}{v_\mathrm{g}} = \frac{d}{d\omega}\beta_1 \tag{1.17}$$

where $\beta = \beta(\omega)$ is the frequency dependent propagation constant. It can also be useful to represent GVD using a derivative with respect to the wavelength λ. Hence, in the context of optical fibers, the following parameter is also often used:

$$D = \frac{\partial}{\partial\lambda}\beta_1 = -\frac{2\pi c}{\lambda^2}\beta_2 \tag{1.18}$$

expressed in [ps/(nm.km)]. Since longer wavelength corresponds to shorter frequency, D and β_2 have opposite signs. For a transform-limited pulse, meaning with the smallest time - bandwidth product[8] $\delta t.\delta\nu$, where δt and $\delta\nu$ are measured as the full width at half maximum (FWHM), GVD introduces an instantaneous frequency variation called chirp that has the effect of widening the pulse duration. Two different situations are possible depending on the material as illustrated by the figure 1.10 (a):

- $\beta_2 > 0$ ($D < 0$): **normal dispersion** regime, longer wavelengths travel faster than shorter ones.
- $\beta_2 < 0$ ($D > 0$): **anomalous dispersion** regime, shorter wavelengths travel faster than longer ones.

After propagation over a distance z in a dispersive medium, like a typical optical fiber described above, a Gaussian pulse initially transform-limited will have a pulse duration (FWHM of the temporal envelope) of:

$$\tau(z) = \tau_0\sqrt{1 + (\frac{z}{L_\mathrm{D}})^2} \tag{1.19}$$

where τ_0 is the initial pulse duration and L_D, the dispersion length, is defined as the propagation distance over which the pulse duration has been increased by a factor $\sqrt{2}$:

$$L_\mathrm{D} = \frac{\tau_0^2}{2.772\,|\beta_2|} \tag{1.20}$$

---

[7] Propagation speed of the wave packet center.

[8] For a Gaussian pulse $\delta t.\delta\nu \approx 0.44$.

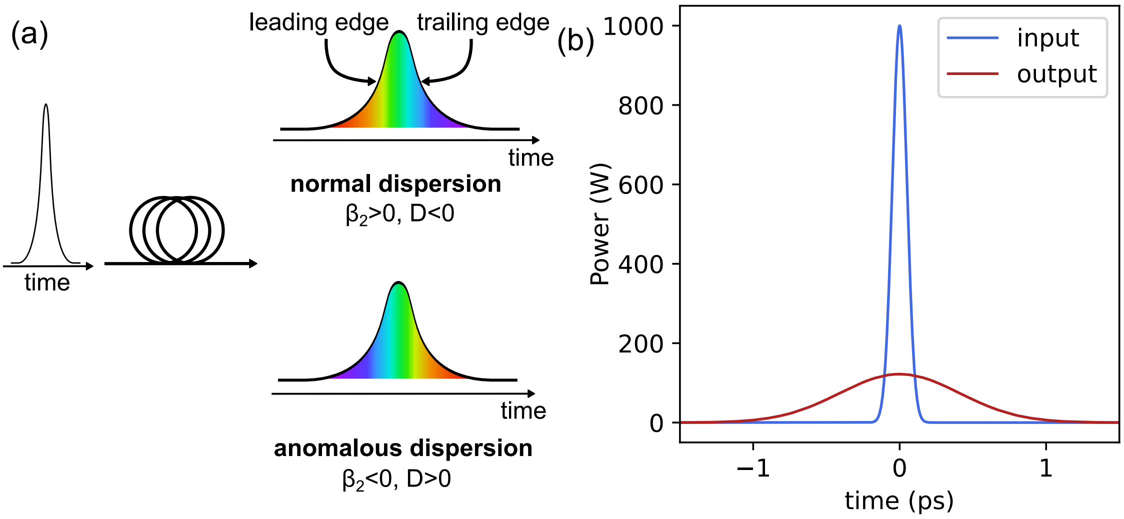

Figure 1.10: *(a) Schematic representation of the effect of group velocity dispersion (GVD) on a short pulse after propagation in a fiber. In the normal dispersion regime ($\beta_2 > 0$), red frequency components lead the pulse envelope, while in the anomalous dispersion regime ($\beta_2 < 0$), blue frequency components lead the pulse envelope. (b) Numerical simulations of a* 100 *fs and* 1 *kW peak power input pulse, at $\lambda = 800$ nm, propagating inside a* 1 *m long Corning HI780 fiber, considered as a purely linear medium (i.e. neglecting nonlinearity and losses).*

Considering the same GVD parameter, a shorter pulse has a smaller dispersion length as evidenced by equation 1.20. From equation 1.19 we see that the temporal broadening is more pronounced for shorter pulses, assuming the same propagation distance. The physical origin of these effects lies in the spectral width, which is larger for pulses of smaller temporal width.

Because nonlinear imaging processes are generally triggered with sub-ps excitation pulses, a numerical simulation of an optical pulse with an initial duration of 100 fs propagating inside an optical fiber with $\beta_2 = 4.07.10^{26}$ s^2/m is represented in figure 1.10 (b). The calculations were performed using the split-step Fourier method described in [51]. The fiber parameters correspond to a standard fiber that is singlemode at $\lambda = 800$ nm (Corning HI780 fiber). For this example, the material is considered purely linear, meaning that we neglect all nonlinearity, and without losses. Figure 1.10 (b) shows a significant peak power reduction because of the temporal broadening caused by GVD after only 1 m of propagation.

It is then clear that GVD is a major issue in the delivery of ultrashort pulses, causing temporal broadening and therefore a reduction of the peak power whereas this is the key parameter in the nonlinear signal generation on biological tissues.

1.2.4 Self phase modulation (SPM)

Unlike GVD, self phase modulation (SPM) is a nonlinear broadening effect, whose origin lies in the intensity dependence of the refractive index, also called optical Kerr effect[9]. SPM induces a spectral broadening of a pulse, under the condition that the intensity of light is high enough to modify the optical properties of the material it is propagating in. The refractive index can then be expressed as:

$$n(t) = n_0 + n_2\, I(t) \tag{1.21}$$

where n_0 and n_2 are the linear and nonlinear refractive indices respectively, and $I(t)$ is the intensity of the optical field. The pulse experiences then a nonlinear shift of its phase:

$$\Phi_{\mathrm{NL}}(t) = n_2\, I(t)\, \frac{\omega_{\mathrm{o}} L}{c} \tag{1.22}$$

The maximum phase shift is attained at the center of the pulse and can be expressed, after propagation over a distance z:

$$\Phi_{\max}(z) = \gamma\, P_0\, z \tag{1.23}$$

where P_0 is the peak power of the pulse, related to the average power P_{avg}, the repetition rate f_{rep} and the time duration of the laser pulse τ:

$$P_0 = \frac{P_{\mathrm{avg}}}{f_{\mathrm{rep}}\, \tau} \tag{1.24}$$

The time dependence of the phase Φ_{NL} induces a spectral broadening, calculated as:

$$\delta\omega(z,t) = -\frac{\partial \Phi_{\mathrm{NL}}}{\partial t} = -n_2\, \frac{\partial I}{\partial t}\, \frac{2\pi z}{\lambda} \tag{1.25}$$

If we consider an unchirped Gaussian pulse and neglect the effect of dispersion ($\beta_2 = 0$), the spectral broadening can be approximated as follows:

$$\delta\omega_{\max} = 0.86\, \frac{\Phi_{\max}}{T_0} \tag{1.26}$$

where T_0 is the initial pulse duration, calculated for an unchirped Gaussian pulse using the initial spectral width $\Delta\omega_0$ by $T_0 = (\Delta\omega_0)^{-1}$. For the same reason as for the GVD, it can be highly useful to express the effect of SPM using a characteristic nonlinear length:

$$L_{\mathrm{NL}} = (\gamma P_0)^{-1} \tag{1.27}$$

---

[9] Because of its similarities with the Kerr electro-optic effect.

This length defines the distance over which the phase shift is $\Phi_{\max} = 1$. Another way to approach it is to use the nonlinear length to express the phase shift $\Phi_{\max} = \frac{z}{L_{\mathrm{NL}}}$.

As evidenced by equation 1.26, the spectral broadening induced by SPM is inversely proportional to the initial pulse duration, meaning that a short pulse under this effect will experience a wide spectral broadening. This strong issue is also illustrated by equation 1.27, accentuating the intense SPM (i.e. short nonlinear length L_{NL}) induced by a high peak power P_0.

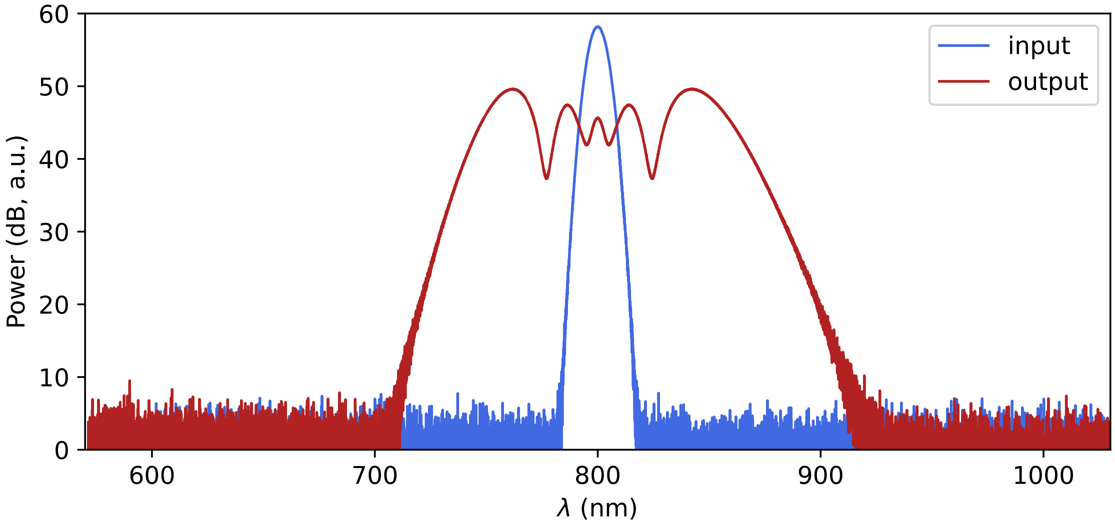

Figure 1.11: *Numerical simulations of a 100 fs and 1 kW peak power input pulse, at* $\lambda = 800$ *nm, propagating inside a 1 m long Corning HI780 fiber, with* $\gamma = 0.013\ (\mathrm{W.m})^{-1}$ *and considering the material purely nonlinear (i.e. neglecting GVD and losses).*

Finally, figure 1.11 shows a numerical simulation of an optical pulse with initially 1 kW peak power and 100 fs pulse duration, before and after 1 m of propagation inside a Corning HI780 fiber. This is again performed using the split-step Fourier method [51]. This time, the fiber is considered purely nonlinear, which means that the dispersion and losses are neglected. The spectral broadening of the pulse is very pronounced and induces an important peak power reduction (note the log scale).

Consequently, SPM is also a major issue in the delivery of sub-ps pulses in optical fibers as a strong pulse distortion is generated, meaning a decrease in the peak power.

1.3 Microscope miniaturization

All advantages of nonlinear imaging techniques have made NLOM a serious candidate for live investigation of biological processes and structures. However, as asserted before, the bulky size of nonlinear microscopes has made it problematic to be employed for *in-vivo* studies. Indeed, a flexible micro-endoscope capable of performing nonlinear imaging would solve this problem. In this scope, the following sections present the requirements and various options to miniaturize the different NLOM elements.

1.3.1 Requirements

One major advantage of nonlinear imaging is the improvement in excitation localization. It requires the simultaneous interaction of multiple photons with the material, which is reached in practice only with focalized laser beams, where the peak power is high enough. Figure 1.12 provides a schematic comparison of the emission volumes in (a) linear and (b, c) nonlinear fluorescence. In the case of 1PEF, every incoming excitation photon can be absorbed to generate a fluorescence photon, hence the emission volume generally is the intersection between the excitation light and the sample, and thin slices are required in order to image a cell layer. However, for nonlinear fluorescence, only a small volume at the focalization spot will emit the signal. It results in a higher spatial resolution, as well as an optical sectioning that could be described as a natural confocality.

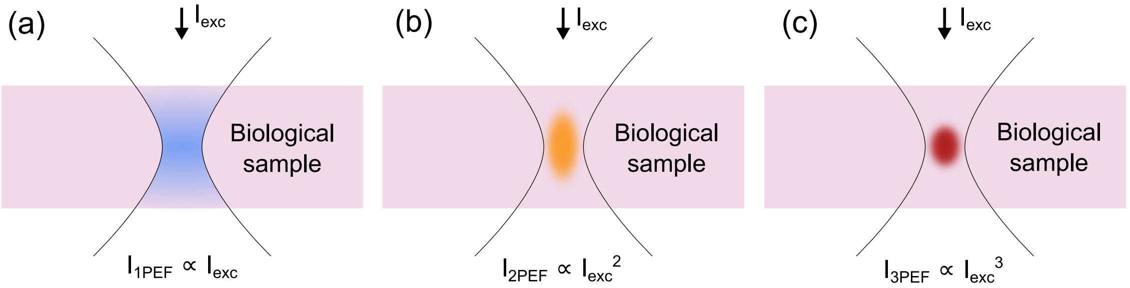

Figure 1.12: *Schematic representation of the fluorescence emission volume at the excitation laser focal spot for (a) 1PEF, (b) 2PEF, and (c) 3PEF.*

Nonlinear processes can be divided into two categories depending on the number of excitation photons absorbed : 2PEF and SHG require the absorption of two photons, whereas three photons are absorbed to generate 3PEF and THG. In this regard, a higher peak power is needed to generate 3PEF and THG, leading to an even higher optical sectioning.

In fact, in 1PEF, the signal generation is identical for all planes along the z axis. In 2PEF or SHG, it decays as $\frac{1}{z^2}$, and $\frac{1}{z^4}$ in 3PEF or THG [6], z being the distance from the focus plane. This much faster decrease reduces greatly the out-of-focus background, thus increasing the optical sectioning.

Moreover, the wavelengths used to excite fluorophores with 3PEF or THG are higher than for other imaging techniques, especially in the 1300 – 1700 nm range where water absorption and tissue scattering drops down [31, 52]. This allows to image much deeper into the sample, to the millimeter range [32]. It makes 3PEF (as well as THG) very attractive for *in-vivo* imaging, although higher peak power, and therefore shorter pulses are required, typically sub-ps pulses with a peak power in the kW range. As it was mentioned, this is not trivial with optical fibers, especially when a wide range of wavelengths is needed as well.

1.3.2 State-of-the-art of ultrashort pulse delivery for nonlinear endoscopy

High peak power short pulse delivery via optical fibers is troublesome because of dispersion and nonlinear effects (in particular SPM) that broaden the pulse temporally and/or spectrally. Nevertheless, different approaches have been employed to bypass this issue in the context of nonlinear endoscopy.

Dispersion

Because a typical fiber will induce a strong dispersion, generally in the normal regime, to short pulses propagating inside its core, the general idea to obtain a short pulse[10] at the output of the fiber is to pre-compensate the dispersion that it will cause [53]. It is realized by adding a negative chirp to the pulse in order to achieve :

$$\beta_{2\ \mathrm{pre-comp}}\, L_{\mathrm{pre-comp}} + \beta_{2\ \mathrm{fiber}}\, L_{\mathrm{fiber}} = 0 \tag{1.28}$$

for a stretcher composed of an optical fiber, or more generally defined with the second order spectral phase $\Phi^{(2)}$:

$$\Phi^{(2)}_{2\ \mathrm{pre-comp}} + \Phi^{(2)}_{2\ \mathrm{fiber}} = 0 \tag{1.29}$$

This pre-compensation can be realized by various procedures, of which the most common are :

- **Anomalous dispersion fiber:** We can manage to compensate completely the dispersion induced by the endoscopic fiber by first propagating in a specific anomalous dispersion fiber that satisfies equation 1.29 [13], as schematically represented by figure 1.13 (a). Although, because the dispersion of a fiber is dependent on the wavelength, this would only apply to a specific wavelength, causing it to be hardly applicable for a multimodal endoscope. Also, nonlinear effects causing a spectral broadening can appear in the process, making it harder to obtain a Fourier transform pulse at the output of the endoscope.

---

[10] As close as possible to a Fourier transform pulse.

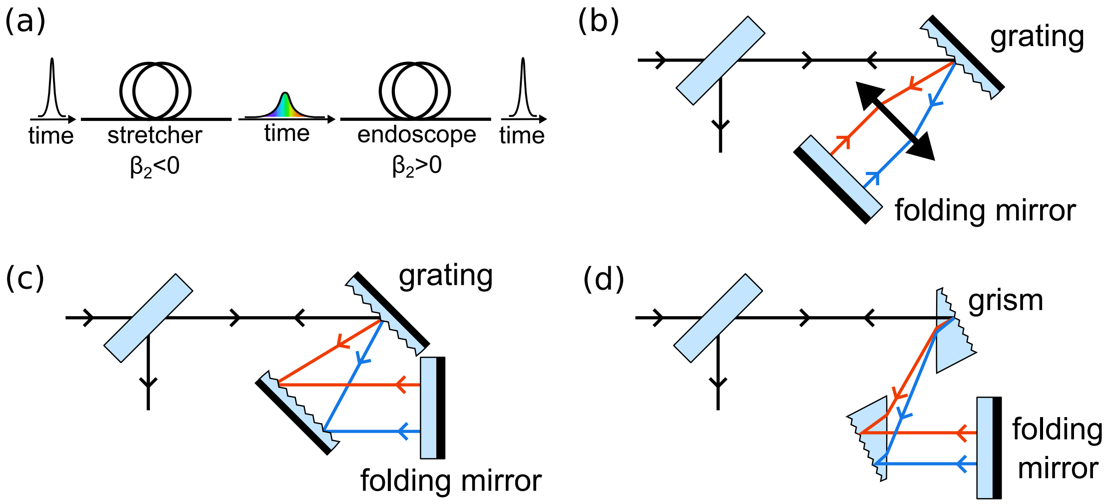

Figure 1.13: *Schematic representation of the different techniques used to deliver ultrashort pulses with optical fibers using pre-compensation schemes to add a negative chirp before injection in the fiber with (a) another optical fiber or a setup with (b) one or (c) two gratings, or (d) a pair of grisms.*

- **Single grating stretcher:** Figure 1.13 (b) shows a pre-compensation scheme using a grating and a folding mirror. A chirp is added to the pulses with a phase mask by either adjusting the distance between the grating and the collimating lens [54] or adding a cylindrical lens before the folding mirror [55]. This technique allows to adjust the compensation regarding the wavelength but only over a rather narrow range, and it needs to be tuned again every time the wavelength is changed. It can also be complicated to correctly recombine the different spectral component before injecting into the fiber.

- **Double grating stretcher:** By using two gratings to separate the spectral components of the pulse, each ends up having a different optical path, thus allowing to adjust the chirp imposed on the pulse [56], as represented in figure 1.13 (c). Again, this allows tuning the chirp with the wavelength but with constraints on the spectral range and the need to adjust it for every wavelength change. Some loss in power are also added which could be problematic.

- **Grism stretcher:** The grating stretcher method allows compensating dispersion of the second order but adds a third order contribution. On the other hand, another stretching technique using prisms [57, 58] can compensate second order dispersion, but over-compensate the third order [59]. Combining both element in one optical component, as shown in figure 1.13 (d), enables to fully compensate second and third order dispersion [60–64]. It is a very efficient pre-compensation method [65], but the downside is an even more complicated setup that is delicate to align, and the cumulated fourth order dispersion of the stretcher combined with the endoscope that can arise.

- **Solitons:** By adjusting the fiber design (for example with a photonic crystal fiber (PCF)), GVD and SPM can compensate each other in order to maintain the pulse shape. These pulses are called solitons, and have been applied to nonlinear endoscopy because they can, by definition, propagate without being affected by pulse broadening effects [6, 52, 66]. The downside of using this technology is the weak soliton conversion, leading to a limitation of the pulse energy [67].

SPM

Self-phase modulation (SPM) happening inside the endoscopic fiber tends to compress the pre-chirped pulses, hence a larger temporal pulse at the output. Reducing the peak power inside the fiber could limit this effect, which can be realized by using a fiber with a larger mode size, spreading the power over a larger surface to reduce the power density. However, two major issues arise from this: the resolution of imaging decreases as the mode size increases, and it becomes harder to reach the peak power required to generate nonlinear effects, especially 3PEF and THG.

Pre-compensation of SPM can also be performed by first generating SPM voluntarily inside a single mode fiber before pre-compensating GVD, *i.e.* inverting the chirp sign, then inject inside the endoscopic fiber [15, 58, 63, 68]. The temporal shape of the pulse is controlled by the pre-compensation scheme used, and the spectrum of the pulse is wide enough before injection in the fiber to avoid SPM altogether. However, a larger spectrum makes the pulses more sensitive to chromatic dispersion. In addition, the use of two separate pre-compensation devices makes the overall setup more complicated and less flexible in terms of quickly switching wavelength or replacing the endoscopic fiber.

1.3.3 Scanning mechanism

To probe the sample under investigation and obtain an image, an endoscopic head must be added at the output of the optical fiber and contain a scanning device. A variety of mechanisms have been used, and the most commonly found are microelectromechanical system (MEMS) mirrors, spectral encoding and piezoelectric tubes.

MEMS mirror

A MEMS mirror is a small mirror mounted on a 2D rotating motor that can be programmed to quickly move the focused spot in order to form a scanning pattern

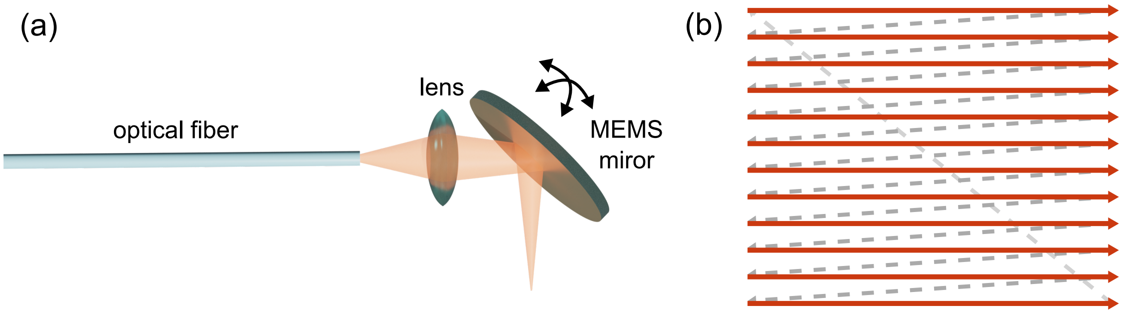

Figure 1.14: *(a) Schematic representation of a microelectromechanical system (MEMS) mirror used to scan the sample at the output of an endoscope. (b) Illustration of a raster scanning pattern.*

on the sample, as showed by figure 1.14 (a). It has been used in the past for *in-vivo* endoscopy [69–71], although it requires some distal optics and leads to relatively bulky heads. It is therefore generally found in endo-microscopes [31] (*i.e.* microscopes with a small deported imaging head) rather than real endoscopes.

A typical scanning pattern, although not exclusive to MEMS mirrors and not the only one used with MEMS mirrors, is the raster scan, is represented in figure 1.14 (b). The pattern firstly forms a straight line in x direction, then comes back to the original position with a small shift in the orthogonal direction y to form a second straight line, and so on until the full image is produced. The focused spot is then moved back to the original position to start the next image acquisition.

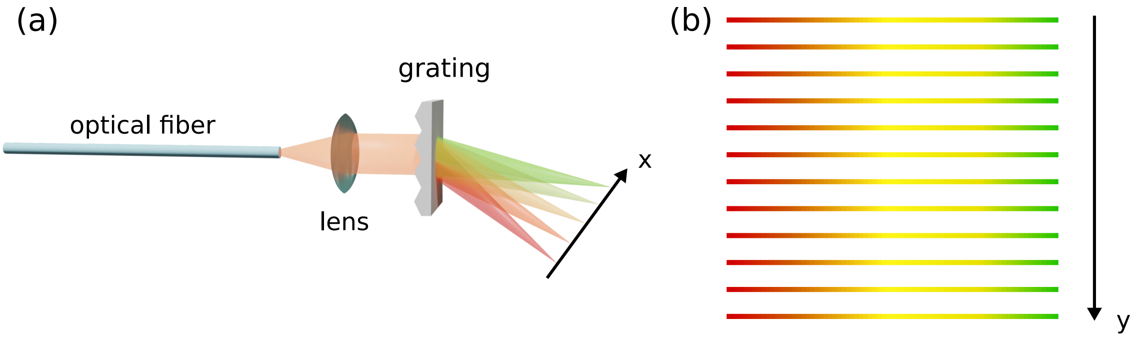

Figure 1.15: *(a) Schematic representation of spectral encoding scan with a grating to probe the sample at the output of an endoscope. (b) Illustration of a spectral encoding scanning pattern.*

Spectral encoding

The spectral encoding technique is schematically represented in figure 1.15 (a). The spectral components of the excitation pulse are spatially separated along one direction, x axis, using a grating [72–75]. After that, a motor or galvanometer will scan the sample in an orthogonal direction, y axis. The advantage of this technique, as opposed to raster scanners, is that only a 1D scanning is performed because the other direction is covered by the 1D spatial separation of the spectral components. The pattern created is shown in figure 1.15 (b).

The image is then reconstructed by recording successive spectra. Hence, the major downside of this technique is that the image acquisition rate is limited to the one of spectral acquisition systems. The detection channel is also complicated as the emission spectrum must be measured which can be tricky with weak signals.

Piezoelectric tube

Finally, a piezoelectric tube with four electrodes placed on two orthogonal directions, resonantly exciting the fiber tip [76–78] as represented in figure 1.16 (a), has been applied as an endoscopy scanning mechanism [15, 19, 54, 79–82].

By appropriately driving both directions with electric signals (a full description will be provided in chapter 3), one can achieve a spiral pattern of the fiber tip, as represented in figure 1.16 (b). After the spiral scan is completed, the driving can be turned off for the fiber to slowly return to its original steady position, or it can be quickly performed by driving both direction of the piezo tube in anti-phase during an active breaking phase, allowing to reach higher image acquisition rates.

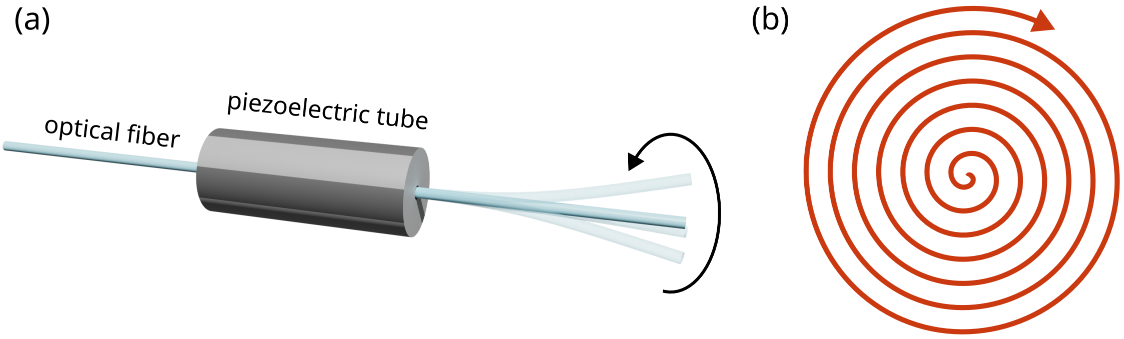

Figure 1.16: *(a) Schematic representation of a doubly resonant piezoelectric tube used to scan the sample at the output of an endoscope. (b) Illustration of a spiral scanning pattern.*

The piezo tube scanner is easily electronically tuned, allows a very small endoscope head, and can reach a few dozens of images per second, which makes it the preferred candidate for a scanning system inside our endoscope head.

1.3.4 Nonlinear signal collection

The nonlinear signal generated at the output of an endoscope can be collected either with the same fiber that delivers the excitation signal, or with a separate collection-only fiber. In the latter, the detection channel is notably simplified, as the collection fiber can be directly plugged to the detector, with an appropriate collection filter, but the endoscopic head design is more complex and needs to be larger.

To keep the distal part of the endoscope as small as possible, the nonlinear signal can be collected and back propagated by a second channel inside the excitation fiber. Because the fiber core will in most cases only weakly collect signals, it is in practice carried out by the cladding around the core, in so-called double clad fibers (DCF).

The TIR guidance inside the inner cladding is made possible by either adding a small layer of low index material (generally a polymer) between it and the mechanical cladding [21], made of high index polymer (represented in figure 1.17 (a)) or with a ring of air holes inside the silica cladding [83], acting as a low index layer as well (represented in figure 1.17 (b)).

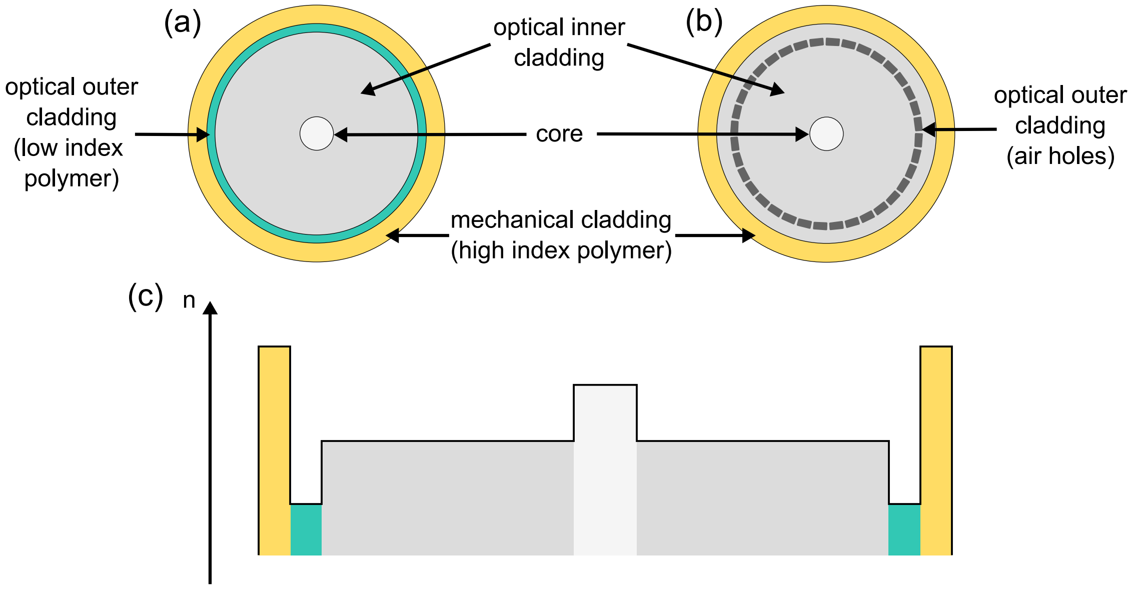

Figure 1.17: *Schematic representation of the different elements in a double clad fiber (DCF), with an inner cladding guiding via (a) a thin layer of low index polymer or (b) a ring of air holes. (c) Schematic index profile of a DCF.*

When guiding with a low index polymer, the NA of the double clad can be simply estimated using equation 1.9. We consider $n_{\mathrm{Si}} \approx 1.46$ in the visible range and $n_{\mathrm{poly}} = 1.37$ for the low index polymer that we use in fabrication (Desolight DF-0016). As a result, a high NA of 0.5 is reachable with this polymer coating.

On the other hand, the NA of the double clad guiding via a ring of air holes, also called air cladding, will be determined by its effective index. To lower it sufficiently, and increase the NA, the silica bridges between air holes must be very thin. With silica bridges thickness lower than half the wavelength, a very high NA (> 0.9) can be reached [83]. However, in a nonlinear endoscope the inner cladding is meant to deliver visible light, typically in the $400 - 700$ nm range. Consequently, the thickness of silica bridges has to be < 200 nm, which is complicated to reach in fabrication.

Conclusion

The different modalities exploited in nonlinear imaging have been described in this chapter, along with their advantages and biological targets. The different elements that must be integrated into a complete setup to form a nonlinear endoscope were introduced as well, particularly the optical fiber requirements, scanning mechanism, and collection scheme.

Chapter 2

Fiber design and properties

In this chapter, we expose the considerations for an optical fiber specifically designed for nonlinear endoscopy. Such a fiber must allow the delivery of high power (typically in the kW range) sub-ps (typically from 50 to 250 fs) pulses over a broad spectral region. The fiber must also contain a second propagation channel, *i.e.* a double clad, with a high collection efficiency to collect and back propagate the nonlinear signal generated within the sample.

Because propagation inside a solid-core fiber remains limited to avoid GVD and SPM, even with pre-compensation, we will hereafter focus our attention to hollow-core fibers. A review of the different types of hollow-core fibers, their guidance mechanisms and characteristics is presented, with the specifications of multimodal nonlinear endoscopy in mind. The fiber fabrication and full characterization are then detailed.

2.1 Hollow core guidance mechanisms and properties

With modes guided in air, hollow-core fibers present unique features over the more conventional solid-core fibers. A major one is the ability to deliver high power laser pulses without generating nonlinear effects nor risking damaging the fiber material [84, 85], thanks to the high damage threshold of air. Because the core refractive index is inherently lower than the surrounding cladding index, total internal reflection (TIR) guidance is prohibited in hollow-core fibers. To overcome this issue, two different effects have been used: photonic bandgap [17, 86, 87], and inhibited coupling [88]. These techniques and the corresponding fiber designs are presented in the following sections.

2.1.1 Photonic bandgap

Photonic crystals present a 2D periodic structure creating a band gap, *i.e.* a spectral window for which light propagation is forbidden for a certain range of n_{eff} [17]. Therefore, light confinement is made possible when surrounded by this periodic structure, forming a so-called photonic band gap fiber (PBGF). This mechanism allows guidance in a medium of refractive index lower than that of the surrounding cladding [87], for example an air core and a silica with air holes cladding, hence the general term of hollow core fiber.

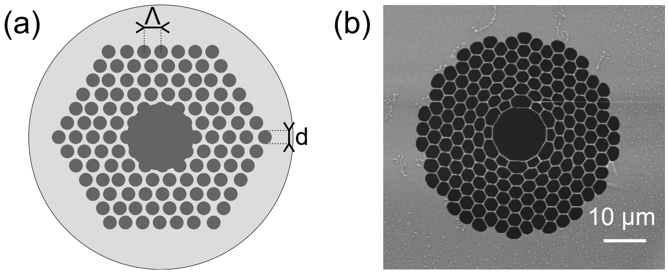

Figure 2.1: *(a) Schematic representation and (b) scanning electron micrograph (SEM) of a photonic bandgap fiber. High and low index materials are represented by light and dark gray respectively.*

The air filling fraction of the cladding, represented by the ratio d/Λ, with d the air hole diameter and Λ the pitch (hole to hole distance), is of great importance. Increasing this ratio widens the transmission band, but also makes it more complicated to fabricate the fiber. A scheme and a scanning electron micrograph of a PBGF fabricated at FiberTech Lille are shown in figure 2.1 (a) and (b) respectively.

A hollow core fiber is able to handle higher power delivery than solid core fibers because of the higher damage threshold of air and low overlap of the core modes with the surrounding silica material. Additionally, it theoretically presents lower losses than conventional silica fibers because of the lower absorption of air compared to silica, even though only leaky modes are present in HCF with confinement loss (CL) prevailing over absorption. However, in practice the loss of PBGF is limited by the surface scattering at the core cladding interface (SSL). Its origin lies in the surface roughness caused by the frozen capillary waves during the fiber draw [89]. SSL scales with the optical overlap of the guided modes with the silica core contour, and it increases when the wavelength shortens.

PBGF are of great interest because of the ability to deliver high power without generating much nonlinear effects, due to the hollow core propagation, as the intrinsic nonlinearity of air is much lower than that of silica. It also presents significantly lower material absorption [90].

Nevertheless, the narrow transmission bands of PBGF, although it can be exploited for spectral filtering for instance, makes it hardly applicable in the context of a multimodal endoscope which needs to transmit a wide range of wavelengths. In addition, the power overlap of the core modes with the glass cladding is rather large compared to the fibers described below, inducing relatively high material absorption inside the silica structure. Finally, propagation inside a PBGF causes a high GVD, especially when close to the band gap edges, which is also an issue for short pulse delivery.

2.1.2 Inhibited coupling

Another way for a hollow core fiber to guide light in absence of a photonic band gap is to inhibit the coupling between the core guided modes and the continuum of modes associated with the cladding. This mechanism was first described to explain the guidance inside a Kagomé fiber [88]. In that case, a core guided mode and a cladding mode can propagate without strong interaction even if they have the same effective index [91].

The guidance mechanism can be described as antiresonance (AR) of the modes at the core cladding interface [92]. IC can lead to higher propagation loss than PBG but with much broader transmission bands (can be more than 1000 nm for IC [93], and about 100 nm for PBG), and very low GVD over the whole transmission window [21].

The first antiresonant optical waveguide was reported in 1986 [95]. The underlying principles can be detailed using a simple slab waveguide description (figure 2.2). The hollow core, of thickness D_{core} and refractive index n_0, is surrounded by two glass walls, of thickness t and of refractive index n_1 so that $n_1 > n_0$.

If the core diameter is large enough as compared to the propagation wavelength λ_0 (*i.e.* if $D_{\text{core}} >> \lambda_0$), then the longitudinal $\overrightarrow{k_L}$ and transversal $\overrightarrow{k_T}$ wave vectors inside the glass can be approximated to $k_0 n_0$ and $k_0\sqrt{n_1^2 - n_0^2}$ respectively [94], where $k_0 = 2\pi/\lambda_0$

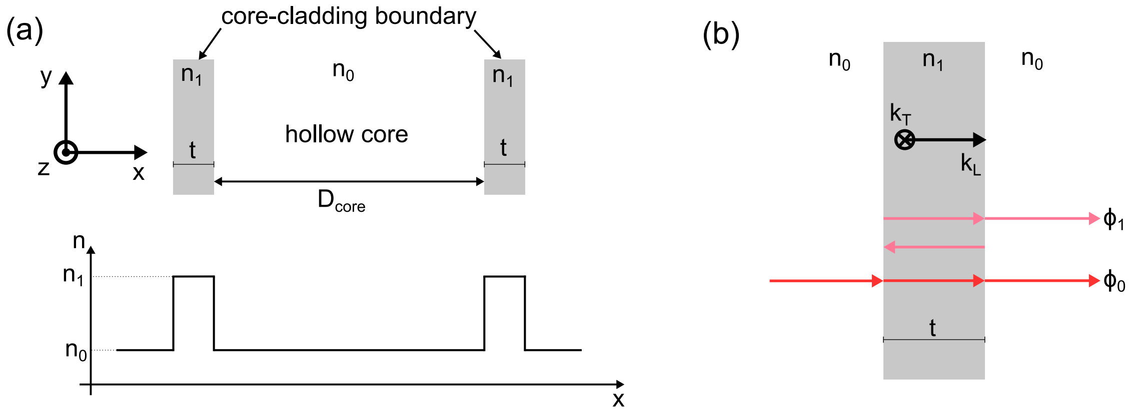

Figure 2.2: *Simplified description of the resonance and anti-resonance at the core contour in an inhibited coupling fiber with (a) the cross-section and refractive index profile of a M-type slab waveguide, and (b) insight on the core/cladding interface. Redrawn from [94].*

is the wave vector in air. Thus, the phase shift between the transmitted waves with and without reflection inside the glass wall is

$$\Delta\Phi = 2tk_0\sqrt{n_1^2 - n_0^2} \tag{2.1}$$

We can then distinguish two states:

- **Resonance** : $\Delta\Phi = 2m\pi$ with m an integer who represents the order of resonance. It corresponds to a wall thickness and wavelength

$$t_\mathrm{R} = \frac{m\lambda_0}{2\sqrt{n_1^2 - n_0^2}} \tag{2.2a}$$

$$\lambda_\mathrm{R} = \frac{2t}{m}\sqrt{n_1^2 - n_0^2} \tag{2.2b}$$

- **Antiresonance** : $\Delta\Phi = (2l - 1)\pi$ with l an integer who represents the order of antiresonance. It corresponds to a wall thickness and wavelength

$$t_\mathrm{AR} = \frac{(l - 1/2)\lambda_0}{2\sqrt{n_1^2 - n_0^2}} \tag{2.3a}$$

$$\lambda_\mathrm{AR} = \frac{4t}{2l - 1}\sqrt{n_1^2 - n_0^2} \tag{2.3b}$$

Therefore, the wave can be put in resonance or antiresonance (*i.e.* can interfere constructively or destructively) by tuning the wall thickness t. This model of light propagation by antiresonance is called antiresonant reflective optical waveguide (ARROW)

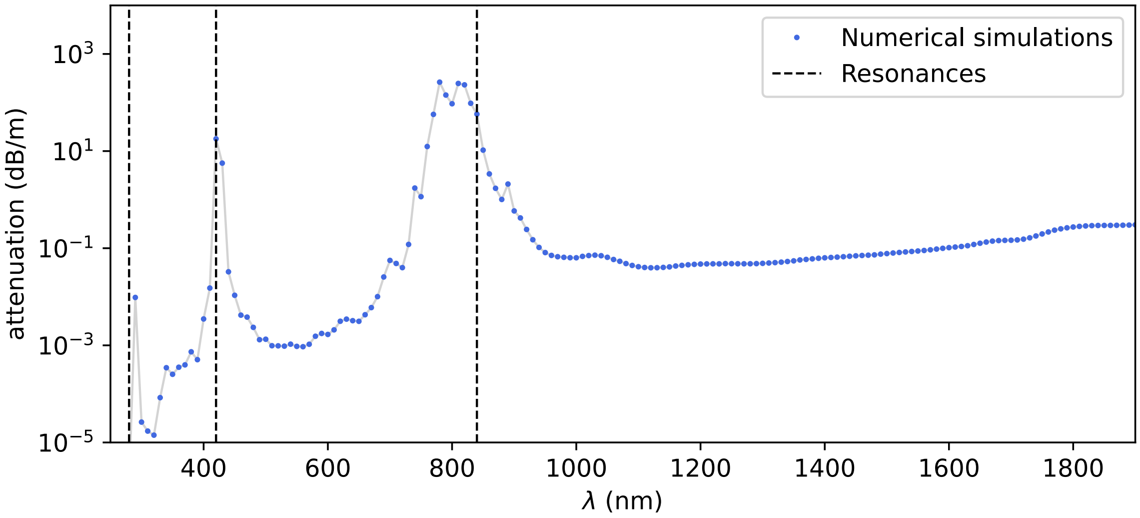

Figure 2.3: *Numerical simulations (Comsol Multiphysics) of the confinement loss (CL) in a tubular hollow core fiber (blue dots). The vertical dashed lines are the resonant wavelengths calculated using equation 2.2b.*

and can be extended to a 2D microstructure. For example, a Bragg fiber has a cladding made of alternating concentric rings of high and low refractive index. In such a fiber, each high refractive index ring can be considered as a Fabry-Perot resonator (if the rings thickness is large compared to the wavelength [96]), and so can enhance or decrease the confinement of light inside the air core under the conditions of antiresonance or resonance respectively.

The transmission spectrum of an antiresonant fiber is multiband, analogous to that of a Fabry-Perot resonator, with the band edges being defined by the resonance wavelengths. As an example, figure 2.3 shows the transmission spectrum (numerical simulations) of a negative curvature tubular hollow core fiber (described hereafter) with the resonance wavelengths predicted by equation 2.2b. The ARROW model is well established in predicting the band edges but fails to provide any more information about the transmission spectrum. In fact, antiresonance is a necessary but not sufficient condition to understand the full guidance mechanism.

Inhibited coupling means highly reducing the leakage from the core to the cladding by suppressing the mode coupling. In order to achieve this, two conditions are to be met: low spatial overlap of the modes involved[1], and a mismatch of their wave numbers [91, 94, 97]. The spatial overlap is highly reduced by the antiresonance conditions described above, hence reducing the wave number mismatch required, although some is always

---

[1] Taking into account the overlap integral of their phase.

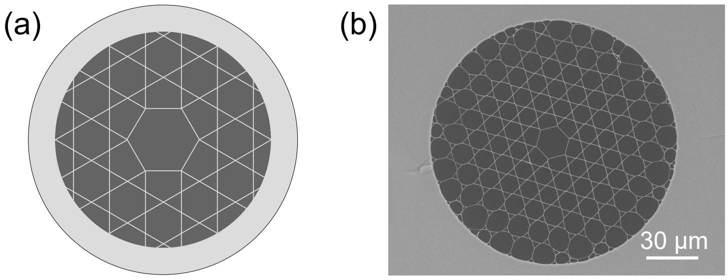

Figure 2.4: *(a) Schematic representation and (b) scanning electron micrograph of a Kagomé fiber. High and low index materials are represented by light and dark gray respectively.*

needed.

Kagomé fibers [18] have a hollow core and a 2D periodic cladding with a pattern similar to a star of David. A scheme and a scanning electron micrograph of a Kagomé fiber fabricated at FiberTech Lille are shown in figure 2.4. This fiber design, guiding via IC, significantly reduces the spacial overlap of the core modes with the silica cladding [92] and therefore minimizes the surface scattering loss, as opposed to PBGF. Moreover, the reduction of the number of cladding layers does not significantly affect the fiber loss nor the spectral bands position [98]. In fact, numerical and experimental studies show that the crucial element in defining the guidance behavior is the core contour [97]. The core wall shape thus plays an important role in lowering the attenuation of the fiber [99]: a negative curvature[2] reduces the spatial overlap of the core modes with the silica, reducing the overall attenuation, this phenomenon getting more important as the radius of curvature gets smaller. This observation led to the creation of so called hypocycloid-core Kagomé fiber [100].

While the Kagomé fiber allows broadband transmission in a hollow core, and with low GVD, its structure is complicated to fabricate. Additionally, the cross-section of the microstructured cladding is very large compared to the hollow core, as attested by figure 2.4 (b). In the context of creating a double clad fiber, such a large microstructure leads to a small cross-section of double clad (*i.e.* the silica material surrounding the microstructure), or a higher overall fiber diameter. As the essential part of the cladding is the core contour, it is then possible to design a simpler fiber without impairing its performances.

Investigations of antiresonance and Kagomé fibers led to the creation of fibers with a hollow core and a cladding made of a single ring of tubes [20] as shown by the figure 2.5 (a), taking advantage of the guidance mechanism of the Kagomé fiber, with the low loss of the core contour negative curvature, and the simplicity of the cladding structure

---

[2] Negative curvature refers to a core wall curvature pointing inwards, which is by convention the negative axis.

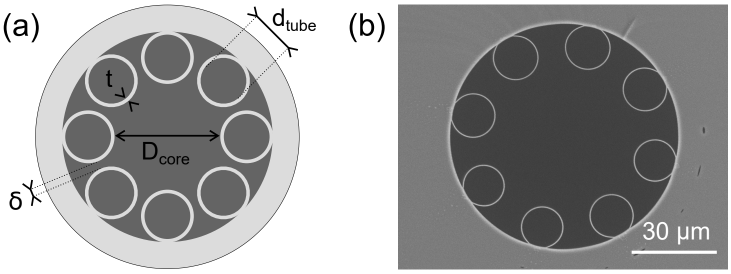

Figure 2.5: *(a) Schematic representation and (b) scanning electron micrograph of a negative curvature tubular fiber. High and low index materials are represented by light and dark gray respectively.*

[94]. The cladding is then much simpler without diminishing the fiber's performances because, since there is no band gap, there is no need of a periodic organization. It is then easier to fabricate, and has a smaller cladding cross-section. Different names are used to refer to these fibers, namely: negative curvature fibers (NCF), antiresonant fibers (ARF), tubular lattice fibers (TLF), or revolver fibers. Figure 2.5 (b) shows a scanning electron micrograph of a NCF fabricated at FiberTech Lille.

The different geometrical parameters of a NCF are the core diameter D_{core}, the tubes inner diameter d_{tube}, the tubes wall thickness t, the gap between the tubes δ, and the number of tubes N (see figure 2.5 (a)). The parameters are related by the following formula[94]:

$$D_{core} = \frac{d_{tube} + 2t}{sin(\frac{\pi}{N})} - (d_{tube} + 2t) \tag{2.4}$$

They can also be tuned to present an almost endlessly single mode propagation, for example when $d_{\text{tube}}/D_{\text{core}} \approx 0.68$ with $N = 6$ [101]. Also, the transmission bands position can be tuned by changing the capillary thickness t, and the bandwidth is inversely proportional to t [102]. Furthermore, the GVD depends mainly on the wall thickness t as well [90]. The leakage loss depends on all the parameters, but the primary sources of loss are the touching nodes, either between the tubes and the outer silica jacket, or between adjacent tubes if they are touching [91, 103]. In the case of non-touching capillaries ($\delta \neq 0$), leakage through the space between the tubes can become a significant source of loss if δ is too high. Therefore, to reduce attenuation, it is better to have non-touching capillaries but with a low δ.

Consequently, negative curvature fiber is, as of today, the best suited for our multimodal endoscope as it presents the advantages of air guidance, low overlap of the core modes with the cladding silica walls, low GVD, broadband transmission with tunable bands position, low SSL, relatively low confinement loss, simplicity and small cross-section of the cladding.

2.2 Double clad negative curvature hollow core fiber

2.2.1 Fiber design

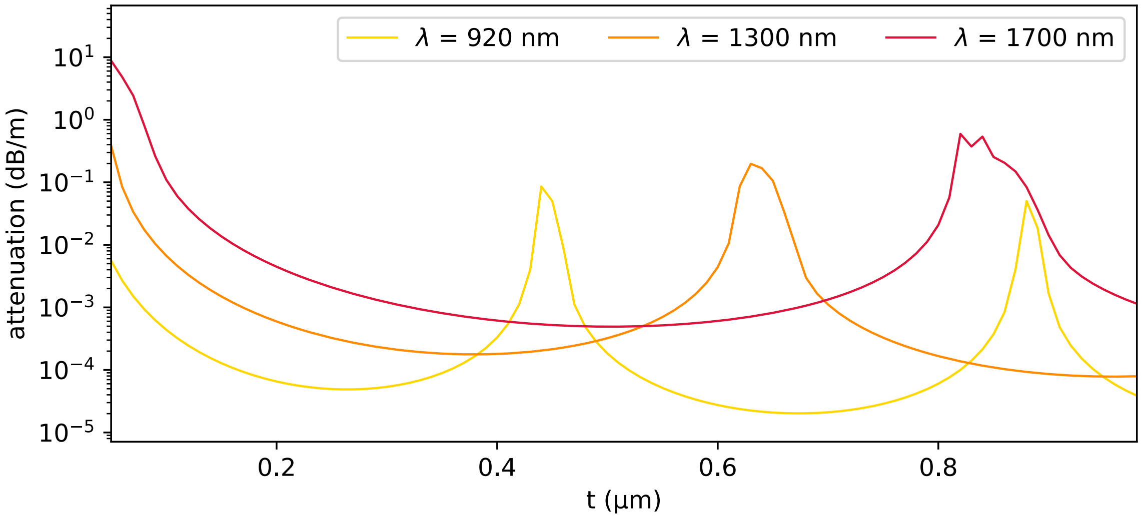

Figure 2.6: *Confinement loss (CL) of the fundamental mode as a function of the capillary wall thickness t inside a negative curvature fiber, with 8 capillary tubes and a 3 µm gap between each tube (calculated using the model from [104]).*

The fiber design that we chose for the endoscope is an 8 capillaries NCF, based on the fiber from [91], that appear to be the best compromise between single mode propagation and low loss guidance over a large spectral band. Because the crucial parameter in determining the transmission bands position is the capillary wall thickness t, we calculated the attenuation using the model described in [104].

Figure 2.6 shows the calculated attenuation spectrum of such a fiber as a function of t for $\lambda = 920$ nm (yellow), $\lambda = 1300$ nm (orange) and $\lambda = 1700$ nm (red), which are three commonly used excitation wavelengths in nonlinear microscopy (see chapter 1).

Besides, it is in our interest to have all excitation wavelengths contained in the first transmission band. The reason for that is the flexibility it brings to the endoscope, with the ability to adjust the excitation wavelength without having a gap in the range of interest. With that in mind, we conclude from figure 2.6 that $t = 400$ nm is the best compromise to limit the attenuation at the targeted excitation wavelengths while retaining them in the first transmission band.

We confirm the accuracy of the model by plotting the attenuation spectrum (a) and group velocity dispersion (GVD) (b) in figure 2.7 (green solid line) and comparing it to

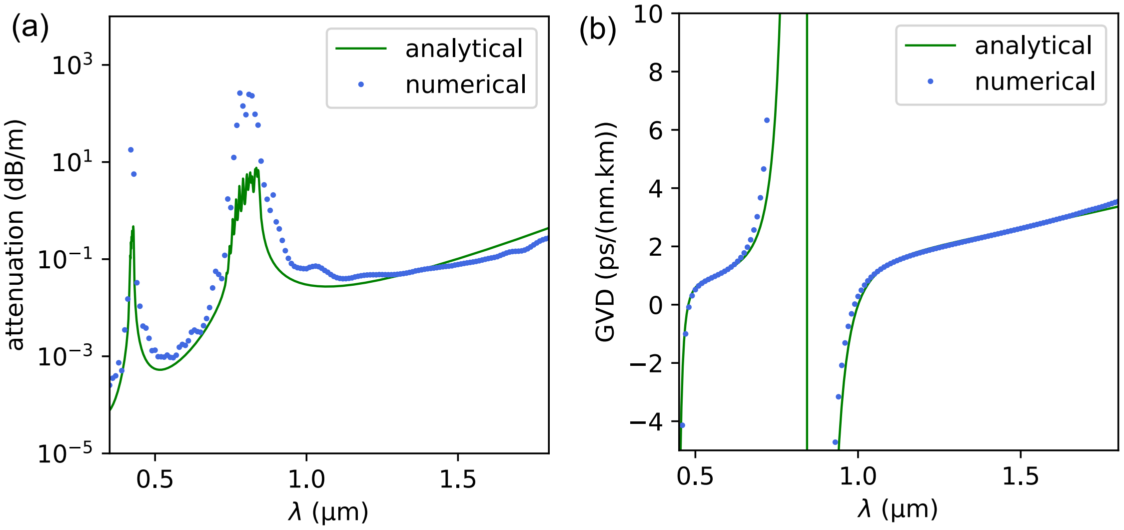

Figure 2.7: *Calculated (a) confinement loss (CL) and (b) group velocity dispersion (GVD) of the fundamental mode inside a negative curvature fiber with a 35 µm core diameter, and 8 capillary tubes of thickness* t = 400 *nm and a* δ = 3 *µm gap between each tube. Calculations using the formula from [104] (green solid line) are compared with numerical simulations realized using Comsol Multiphysics (blue dots).*

Comsol Multiphysics numerical simulations (blue dots) of the same fiber. The capillary wall thickness is fixed at t = 400 nm. Figure 2.7 (a) shows a first transmission band ranging, as expected, from about 850 nm to at least 2000 nm. The fiber dispersion (figure 2.7 (b)) over the whole transmission window is very low, $<$ 3 ps/(nm.km). This allows to deliver sub-ps pulses without temporal broadening, as we shall see below.

Figure 2.8 (a) is a comparison of attenuation sources in this fiber, obtained by Comsol Multiphysics numerical simulations. The surface scattering losses (SSL, light blue) are several orders of magnitude bellow the confinement losses (CL, dark blue). It confirms that SSL do not have a major impact in NCF and therefore will not be taken into consideration hereafter.

Finally, one considerable issue with NCF is that bending losses can become non-negligible. Numerical simulations show that the bending losses remain very low, $<$ 0.1 dB/turn, even for a radius of bending bellow 10 cm (see figure 2.8 (b)). Nevertheless, we note that these losses are more prominent when getting close to the transmission band edges, *i.e.* for $\lambda = 920$ nm in figure 2.8 (b).

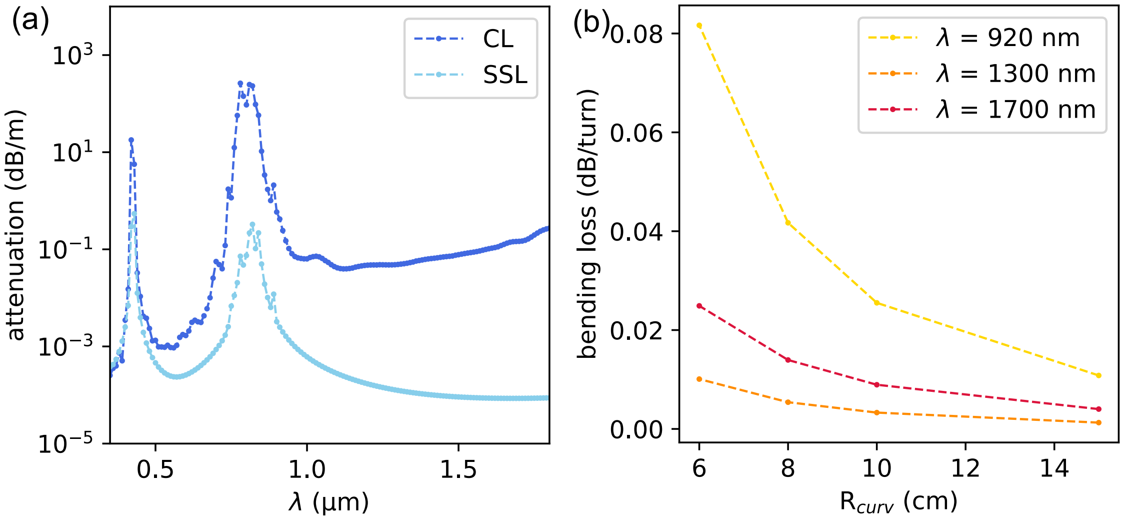

Figure 2.8: *Numerical simulations (Comsol Multiphysics) of (a) the confinement loss (CL, dark blue) and surface scattering loss (SSL, light blue), and (b) the bending loss as a function of the radius of curvature* R_{curv} *for* $\lambda = 920$ *nm (yellow),* $\lambda = 1300$ *nm (orange) and* $\lambda = 1700$ *nm (red).*

2.2.2 Fiber fabrication

The fabrication process for the double clad hollow core fiber (DC-HCF) is based on the stack and draw process, for which the steps are represented in figure 2.9 (a). First the stack is realized by placing hollow capillary tubes around a glass rod to keep them in place. Smaller holds (in dark blue in figure 2.9 (a)) are also placed between the capillaries to maintain a regular spacing. The structure is then inserted inside a larger silica jacket, on which the capillaries will be spliced during the cane drawing. This is performed by heating a region of the stack without holds, while pulling the canes out. A second jacketing is then carried out to increase the size of what will be the inner cladding of the fiber. Finally, the cane is drawn to a fiber following the scheme of figure 2.9 (b). The ratio between the fiber pulling speed and the cane descending speed into the furnace (preform feed) determines the fiber diameter. The capillaries diameter and thickness are adjusted by controlling separately the pressures inside the core and the hollow capillaries.

A monomer layer is added to cover the bare fiber, then polymerized with a UV light. This first polymer layer, with a low index, allows the guidance inside the inner cladding. The same procedure is repeated to add a second layer of polymer coating, of high index, for mechanical protection. The fiber fabricated is shown in figure 2.10. It has 8 capillary tubes of inner diameter $d_{\mathrm{tube}} = 15$ μm and thickness $t = 425$ nm. The gap between capillaries was measured to be $\delta = 7.2$ μm, and the hollow core diameter $D_{\mathrm{core}} = 45$ μm. The inner diameter of the silica double clad is 72 μm, and its outer

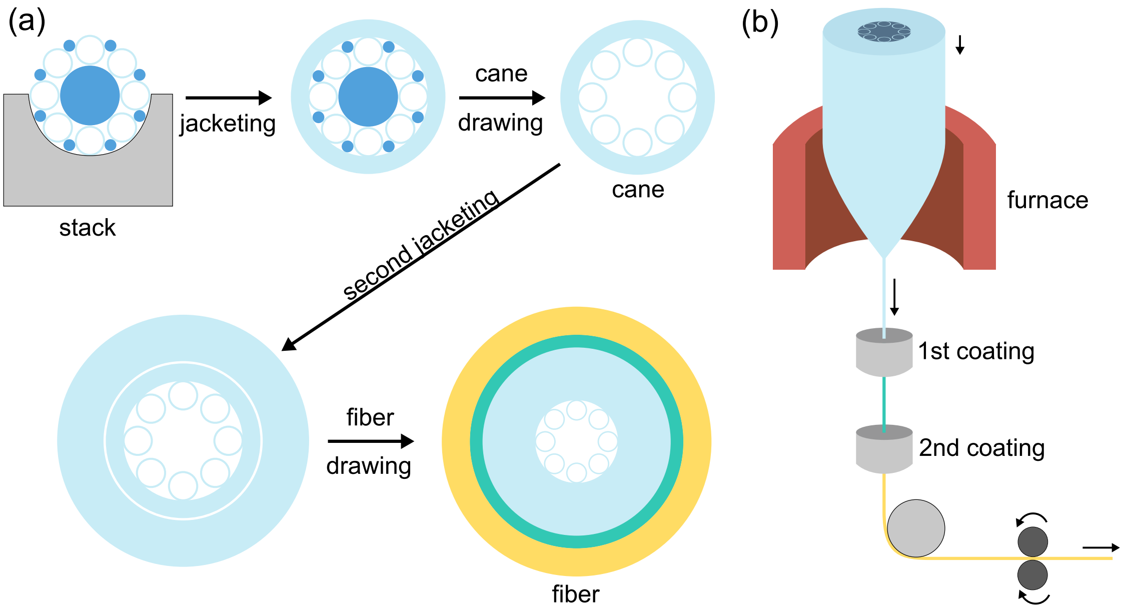

Figure 2.9: *(a) Illustration of the different steps in a stack and draw process, for the fabrication of a double clad negative curvature hollow core fiber. (b) Schematic representation of the fiber drawing tower.*

diameter is 307 µm, leading to a collection surface $S = 70\,000\ \mu\text{m}^2$. This is much higher than for Kagomé fibers [19] thanks to the smaller cladding structure of NCF, as evidenced by the comparison between figure 2.10 (a) and (c).

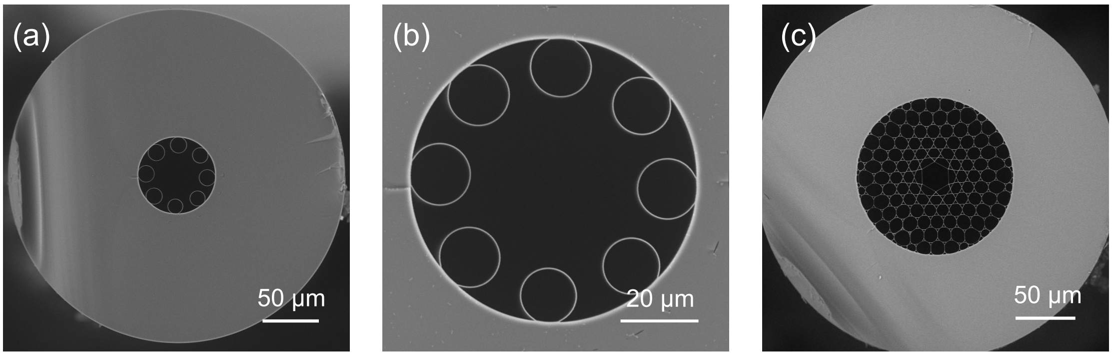

Figure 2.10: *(a) Scanning electron micrograph of the double clad negative curvature hollow core fiber fabricated at FiberTech Lille, with (b) a close-up view in the hollow core region. (c) Scanning electron micrograph of the double clad Kagomé hollow core fiber fabricated at FiberTech Lille.*

2.2.3 Transmission properties

The transmission properties of the fabricated NCF are measured by injecting a supercontinuum source (YSL) into its core. The output of the fiber (near field) is imaged using a Si (DCC1645C, Thorlabs) or InGaAs (SU320KTS-1.7RT, SUI) camera, depending on the wavelength of interest. The injection is thus adjusted to maximize the transmission into the fundamental mode of the NCF.

The output of the fiber is sent to an optical spectrum analyzer (OSA, AQ-6315A, Ando) to record its transmission spectrum. The attenuation of the fiber can be obtained by the cutback method. The transmission of a long fiber, in our case 20 m, is recorded, then most of the length is cut off. The transmission of the short length remaining, here 1 m, is again measured without changing the injection into the fiber. The difference between both measurements divided by the length removed gives us the attenuation spectrum of the fiber, represented in figure 2.11.

The NCF has a very large first transmission band that ranges, has expected, from 850 nm to, at least, 1750 nm (upper limit of the OSA). This transmission band covers the commonly found excitation wavelengths for the different nonlinear effects targeted, as evidenced by the green (2PEF, SHG), yellow (CARS) and red (3PEF, THG) rectangular areas in figure 2.11. Furthermore, the measured attenuation for the whole band is almost flat at 0.5 dB/m, except for $\lambda < 1000$ nm where it slowly increases to 0.7 dB/m at 850 nm. The second transmission band, even if not very significant in our endoscope design because the collection from the core is negligible as compared to the inner cladding, is located in the visible range.

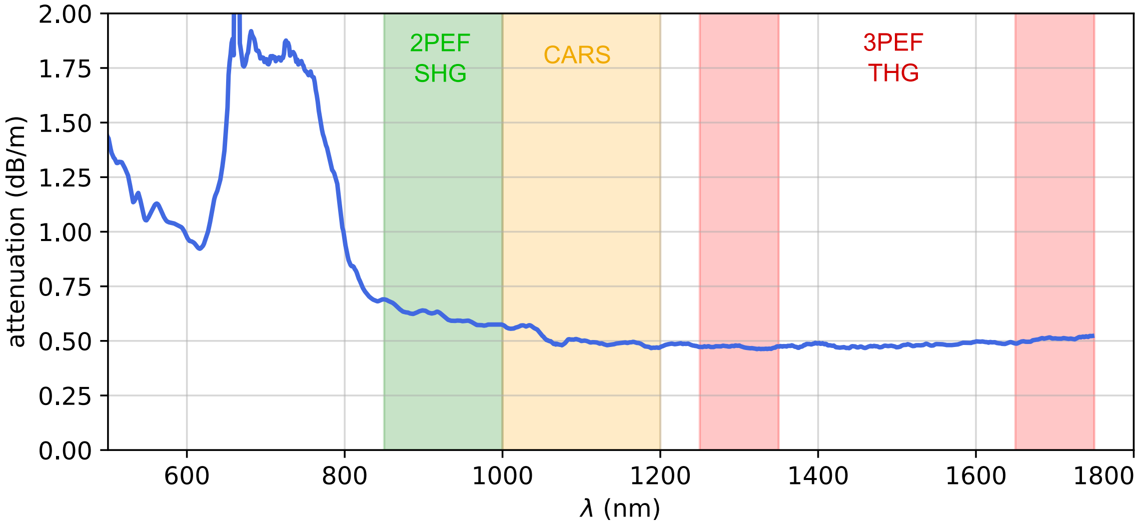

Figure 2.11: *Measured attenuation spectrum of the DC-NCF fabricated.*

2.2.4 Group velocity dispersion

We then measured the group velocity dispersion (GVD) of the fiber using the low coherence interferometry method [105], with the setup presented in figure 2.12 (a). Again, a supercontinuum is used to perform the measurement at different wavelengths, by simply changing the bandpass filter in front of the detector. The source is separated into two arms forming a Mach-Zehnder interferometer: one serves as a reference and

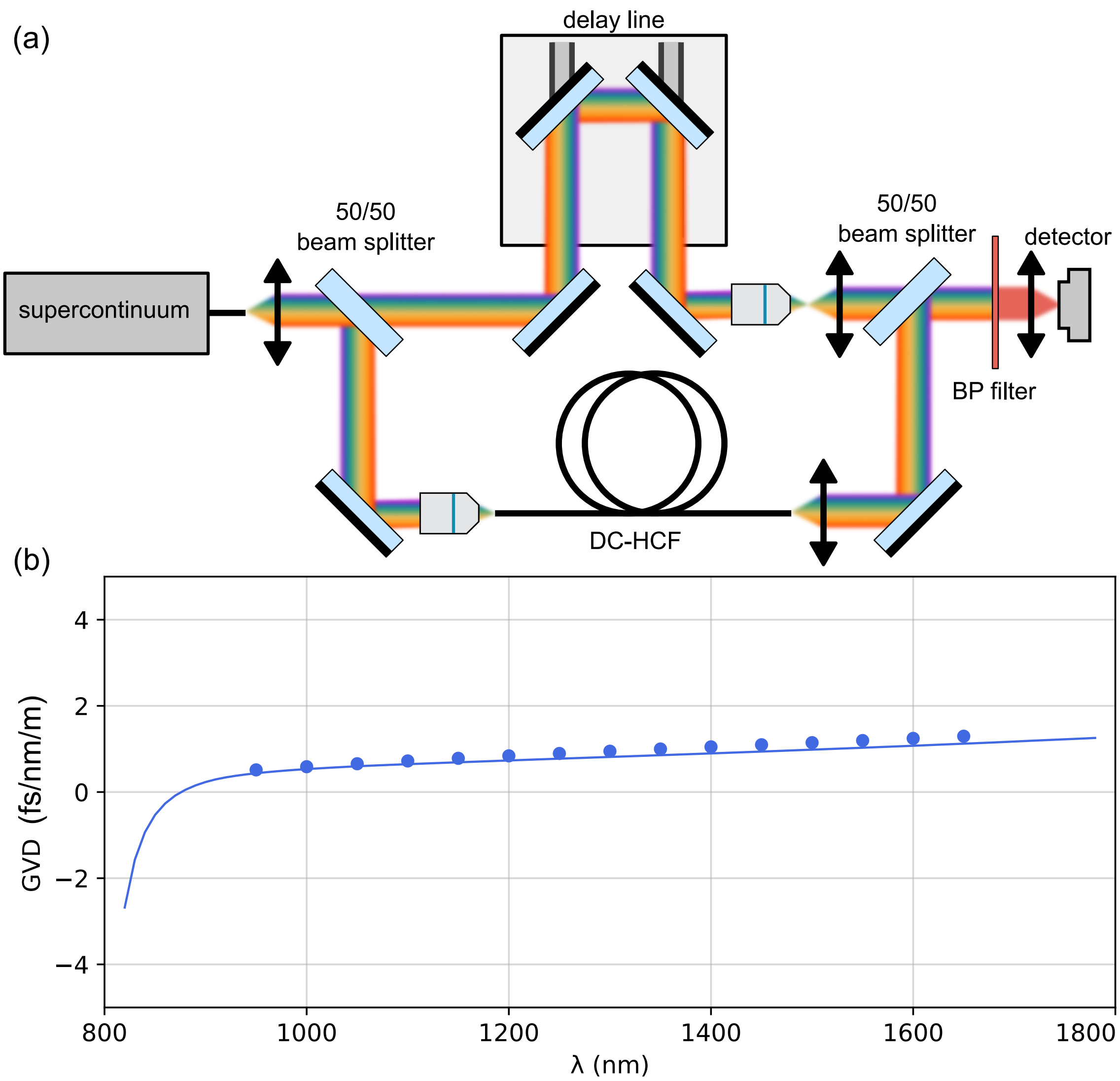

Figure 2.12: *(a) Schematic representation of the setup used to measure the GVD of a fiber using the low coherence interferometry method [105]. (b) Measured GVD of the DC-NCF over the first transmission band (blue dots), compared to Comsol Multiphysics numerical simulations (solid blue line).*

the other is injected into the fiber. To ensure only the GVD of the fiber is measured, a microscope objective and a lens, identical to the ones used to inject into the fiber and collect the output beam, are placed on the reference arm. Both arms are then spatially superimposed before being sent to the detector. A delay line in the path of the reference arm allows to adjust the temporal alignment between both beams in order to generate interferometry fringes. The difference in delay line position Δx corresponding to a wavelength difference $\Delta\lambda$ hence gives a relative measurement of the GVD:

$$D(\lambda) = \frac{2\,\Delta x}{\Delta\lambda}\,\frac{1}{c\,L} \tag{2.5}$$

with $c \approx 2.99.10^8$ m/s the speed of light and $L = 1$ m the fiber length.

With this method, we obtain the GVD over the first transmission band of the NCF, and depict it in figure 2.12 (b) (blue dots). It remains very low, under 2 fs/nm/m, for all wavelengths probed, and fits very well with the numerical simulations (solid blue line) realized before.

2.2.5 Fundamental mode size

The DC-HCF core diameter is, as asserted above, $D_{\text{core}} = 45$ µm. The fundamental mode was imaged at the output of a 2 m long fiber with a Si (DCC1645C, Thorlabs) camera, at $\lambda = 920$ nm. It is represented in figure 2.13 (a). To measure the mode size, we realize a plot along the dashed blue line (blue dots in figure 2.13 (b)). We then fit the measurement with the following Gaussian function (solid gray line) :

$$G(x) = a\,.\,exp\Big(\frac{(x-x_0)^2}{2\,\sigma^2}\Big) \tag{2.6}$$

where a is the peak intensity (set to $a = 1$ in our case), and x_0 its position (set to $x_0 = 0$ here). With the standard deviation σ, we can calculate the mode field diameter (MFD, diameter at a/e^2) and the full width at half maximum (FWHM) :

$$MFD = 4\,\sigma \tag{2.7a}$$

$$FWHM = 2\,\sqrt{2\,ln(2)}\,\sigma \approx 2.3548\,\sigma \tag{2.7b}$$

In our case, we measure $MFD = 37.3$ µm, and $FWHM = 22$ µm. The MFD is a crucial parameter when implementing a fiber for endoscopy. Indeed, the imaging resolution will (partly) depend on its value, so we want it to be as low as possible. In this scope, a MFD of 37.3 µm is too large, and we need to reduce it before adding the fiber to the endoscope scheme, as we shall see in the next chapter.

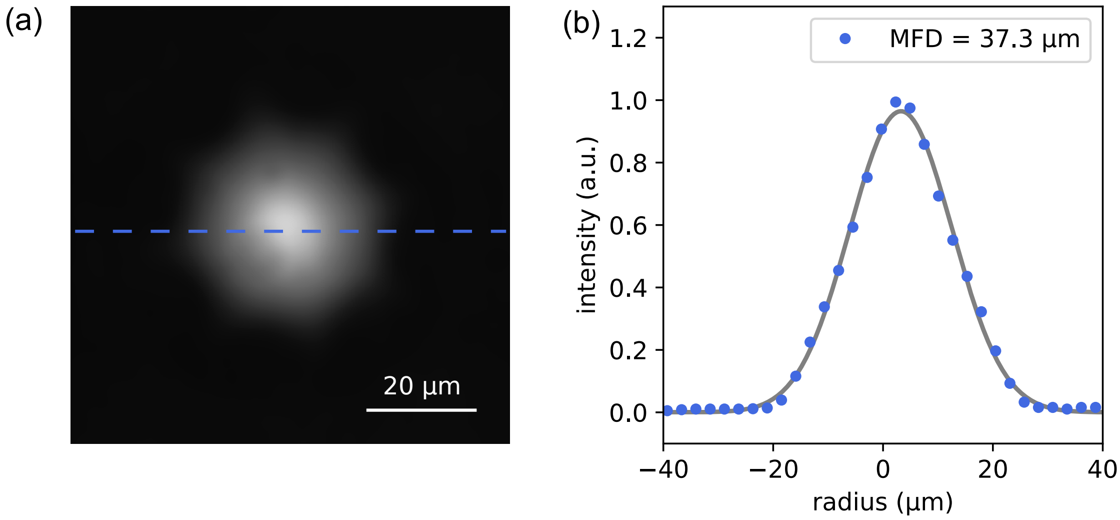

Figure 2.13: *(a) Fundamental mode of the DC-HCF imaged at* $\lambda = 920$ *nm and (b) plot along the blue dashed line (blue dots), with a Gaussian fit (solid gray line).*

2.2.6 Numerical aperture

The numerical aperture (NA) of a given fiber provides an information on the divergence of the beam at the output, and also on the acceptance cone at the input. For the core of the DC-HCF, that information is particularly important for the input of the fiber as it determines the ease of injection inside the fiber, *i.e.* excitation of the fundamental mode.

To measure the NA at different wavelengths, we perform the measurement described by figure 2.14 (a). We use a supercontinuum source and a bandpass filter to inject into the fiber. The far field is imaged with a Si (DCC1645C, Thorlabs) or InGaAs (SU320KTS-1.7RT, SUI) camera (depending on the wavelength). By moving the camera away from the fiber and successively measuring the mode size, we obtained the $1/e^2$ radius as a function of the relative camera position. This is shown in figure 2.14 (b) for $\lambda = 920$ nm (yellow dots), $\lambda = 1300$ nm (orange dots), and $\lambda = 1700$ nm (red dots). The slope of a linear fit on the measurement (solid lines) grants the NA.

Our measurements of the NA (in the legend of figure 2.14 (b)) are all very low, < 0.05 for all wavelengths probed. Although it does not render the fiber unusable, it does make the setup alignment more delicate, especially when switching wavelength, and prone to misalignment over time. This is an issue that should be addressed in the future to establish a more stable endoscopy setup.

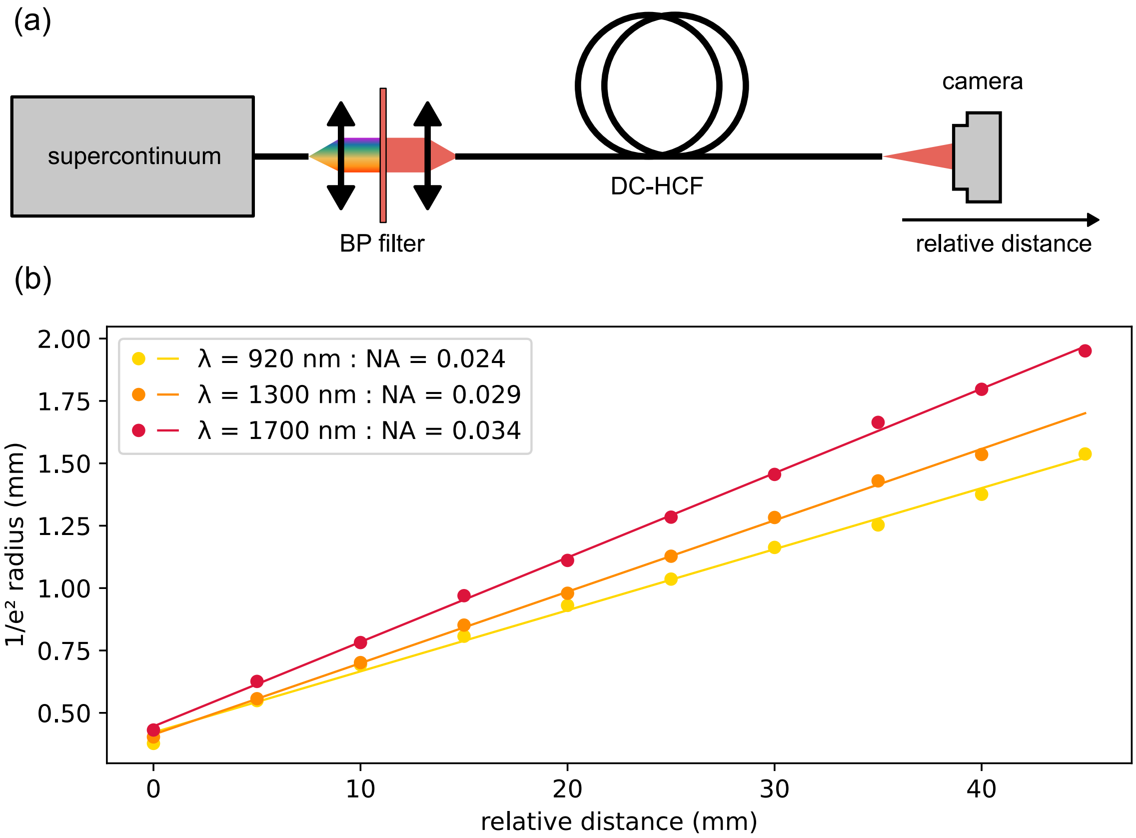

Figure 2.14: *(a) Schematic representation of the setup used to measure the NA of a fiber core. (b) Measured* $1/e^2$ *radius as a function of the relative camera position at* $\lambda = 920$ *nm (yellow),* $\lambda = 1300$ *nm (orange), and* $\lambda = 1700$ *nm (red).*

2.2.7 Ultrashort pulses delivery

As explained in detail above, the main reason for choosing a hollow core NCF design for endoscopy is the ability to deliver pulses without distortion. This is confirmed by the low GVD measurement presented in 2.2.3. Nevertheless, we ensure this by measuring the pulse duration before and after propagation inside the fiber described in 2.2.2, even for sub-100 fs pulses. The source used for this purpose is made of an ytterbium doped master oscillator power amplifier (Monaco, Coherent) pumping a broadband optical parametric amplifier (Opera-F, Coherent), tunable over the 640-940 nm and 1147-2676 nm ranges. It delivers 40-80 fs pulses with an energy of a few μJ, at a 1 MHz repetition rate. Autocorrelation traces, plotted in figure 2.15, were measured using an autocorrelator (pulseCheck, APE) before (solid lines) and after (dots) 2 m of propagation inside the fiber's hollow core.

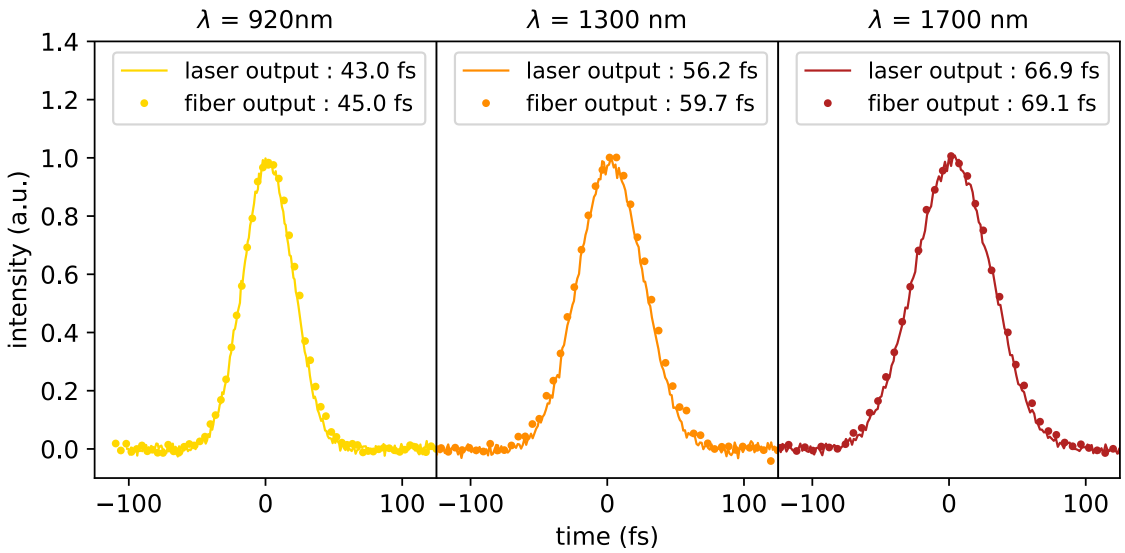

Figure 2.15: *Measured autocorrelation traces at the laser output (solid lines) and after propagating in a 2 m long NCF (dots), for* $\lambda = 920$ *nm (yellow),* $\lambda = 1300$ *nm (orange), and* $\lambda = 1700$ *nm (red).*

The autocorrelation traces measured after the fiber are superimposed on the traces measured before, showing that even for sub-100 fs pulses no temporal distortion is induced by the fiber. This is further emphasized by the pulses duration (shown in the legends of figure 2.15). Only a very slight increase in the pulse duration is measured, confirming the suitability of this fiber to deliver short pulses, in particular for a multimodal endoscope.

2.2.8 Double clad for signal collection

In the endoscopic scheme, the signal collection is performed by the double clad of the fiber. As explained in chapter 1, guidance inside the double clad is enabled by adding a layer of low index polymer (Desolight DF-0016, $n = 1.37$) between the inner cladding (silica) and the high index polymer cladding. To increase the efficiency of the collection, two parameters are to be taken into account. First the collection surface, *i.e.* the section of silica shown in figure 2.10 (a), has been increased with a NCF design as compared to previously used Kagomé fibers (see section 2.2.2). Then the NA has to be as high as possible to maximize the collection efficiency.

Figure 2.16 (a) shows the setup used to measure the numerical aperture of the double clad. It is similar to the one used for the measurement of the hollow core NA (figure 2.14 (a)), except the injection into the inner cladding is performed with a high NA (0.65)

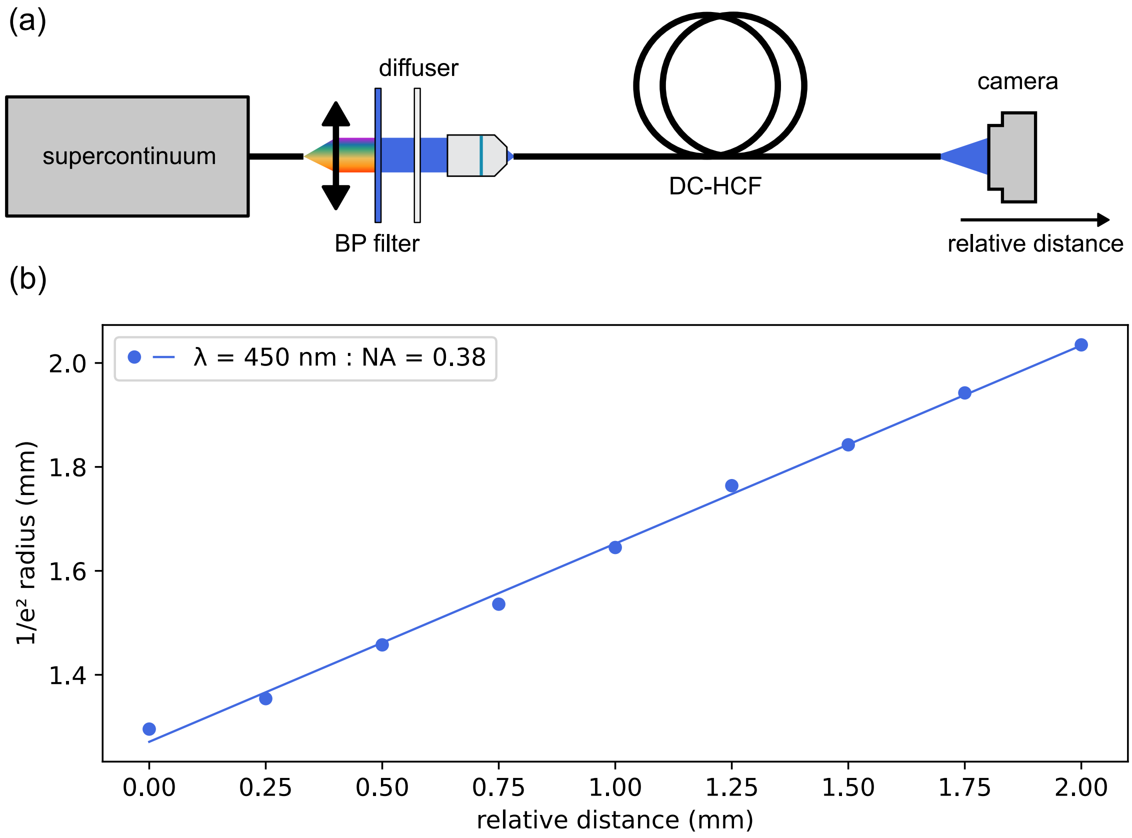

Figure 2.16: *(a) Schematic representation of the setup used to measure the NA of a fiber double clad. (b) Measured* $1/e^2$ *radius as a function of the relative camera position at* $\lambda = 450$ *nm (blue dots), and linear fit (solid blue line).*

x40 microscope objective, coupled with a diffuser to guarantee all modes of the cladding will be excited. This is sufficient because the NA of the microscope objective is above the theoretical value of the NA calculated for the double clad of the fiber (0.5, see chapter 1).

Likewise, the cladding NA, at $\lambda = 450$ nm, is obtained by plotting the $1/e^2$ radius of the far field as a function of the relative position of the camera (blue dots in figure 2.16 (b)). The slope of the linear fit (solid blue line) returns the NA, in our case 0.38. While it is not exactly close to the estimated value because it did not take into consideration the high number of modes guided in the double clad, it is still a high NA and should provide a good signal collection for the endoscope.

Conclusion

A double clad hollow core fiber was designed and fabricated to be specifically applied to multimodal nonlinear endoscopy. Eight capillary tubes surrounding the hollow core allow singlemode guidance over a large spectral band, from 850 nm to more than 1750 nm, covering all typical excitation wavelengths used in nonlinear imaging. A group velocity dispersion under 2 ps/nm/km over the whole transmission band also enables the delivery of ultrashort pulses without temporal broadening. A silica double clad surrounds the hollow microstructure to collect and back-propagate the nonlinear signal, with a large surface (70 000 μm^2), by virtue of the small microstructure size, and a high numerical aperture (0.38, measured at $\lambda = 450$ nm).

Chapter 3

Endoscope assembly and performances

The double clad negative curvature hollow core fiber detailed in chapter 2 allows the delivery of sub-ps pulses with peak power in the kW range, needed to generate the nonlinear imaging effects. It can also collect and propagate the signals generated by the sample. The DC-HCF constitutes the center element of the nonlinear endoscope, but needs additional elements to provide a usable imaging setup. First the output beam of the fiber needs to be tightly focused to trigger the nonlinear effects and reach a high resolution of imaging. The focused spot must also be shifted away from the fiber to achieve a convenient working distance, which in term allows imaging under the sample surface. This is performed with the addition of optical elements to the fiber tip, coupled with a fixed micro-objective inside the endoscope head. Both elements are presented in the first sections of this chapter.

The following sections expose the devices implemented to realize images from the optical fiber. Indeed, to probe an area inside a biological tissue, the focused laser spot needs to be moved around to scan an area. For this purpose, a piezoelectric tube is used to provide a resonant excitation of the fiber tip.

Two different endoscope designs are then presented, and their performances are compared to each other, including an imaging comparison. Finally, the full endoscopic head design for multimodal imaging, with previously mentioned elements embedded, is presented.

3.1 Fiber tip functionalization

Hollow core fibers, in particular NCFs, present many advantages for multimodal nonlinear endoscopy, but the major drawback is the output mode size. Because the core diameter tends to be quite large, so is the fundamental mode (FM, see section 2.2.5). On the other hand, in a fiber based endoscope, the spot size at the output is crucial to determine the imaging spatial resolution. In this scope, the target spot size should be as small as possible, meaning in the same order of magnitude as the wavelength. Thus, a 22 µm FWHM spot is way too large. This needs to be addressed before assembling the endoscope head onto the fiber.

It is important to note that by convention, the focal spot size for the excitation light in an imaging setup, called point spread function (PSF), is taken as the FWHM. It differs from the convention in optical fibers, where the mode size is measured by the mode field diameter (MFD), which is the diameter at $1/e^2$ of the maximal intensity. Because the aim of this fiber is to perform imaging, we will hereafter express both the mode and spot size as the FWHM.

The reduction of the mode size at the output of the DC-HCF can be achieved with the addition of an optical element directly fixed at the fiber distal tip. This step is therefore referenced as the fiber tip functionalization. Two options are proposed in the following sections: a silica bead inserted inside the hollow core of the fiber and a graded index (GRIN) fiber spliced to the DC-HCF then polished to a fixed length. Both options are implemented into an endoscope and an in-depth investigation of their respective characteristics and results is provided later in this chapter.

3.1.1 Silica bead

Silica beads have be used to tightly focus a laser beam by generating a photonic nanojet [106, 107]. Utilizing this effect, a silica bead can be placed directly inside the hollow core of a fiber, acting as a ball lens. The FM is then focused to a small spot size immediately after the fiber. This method has been successfully applied to endoscopy setup both with Kagomé fibers [19] and NCF [21].

Fabrication

To accomplish this assembly, the DC-HCF is placed in the setup represented in figure 3.1 (a). A white light is injected into the fiber, and its distal surface is imaged with a Si camera. Silica beads of 45 µm diameter are diluted inside water then spread on a microscope slide. The slide is then dried with the beads attached to its surface. It results in beads spread out far away from each other, has shown in figure 3.1 (b), making it easier to isolate one to be embedded into the fiber.

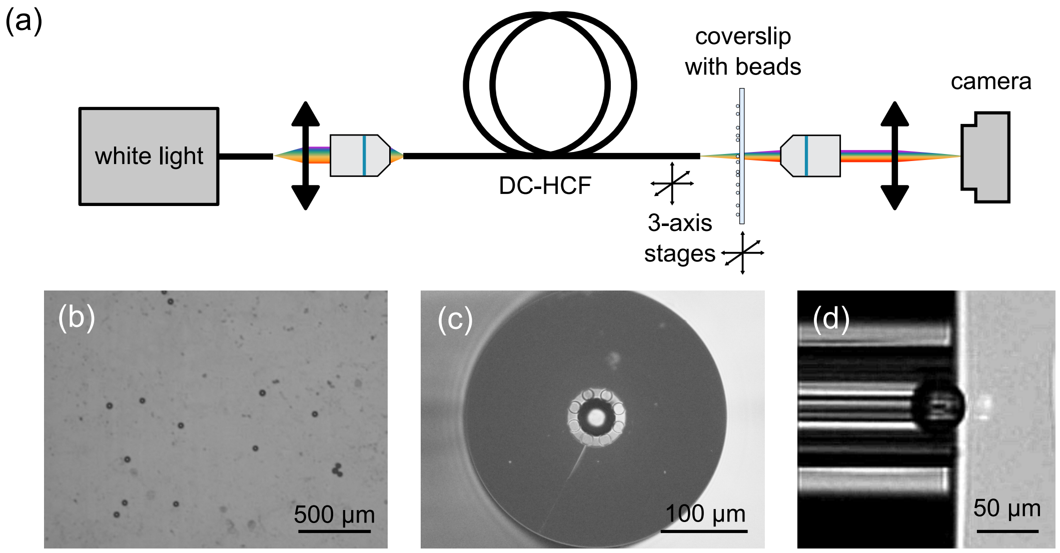

Figure 3.1: *(a) Schematic representation of the setup used to place a silica bead inside the core of a DC-HCF. (b) 45 µm beads in diameter, spread on the surface of a microscope slide and observed with an optical microscope. Optical microscope images of (c) the endface and (d) side view of the DC-HCF after insertion of the silica bead.*

The slide covered with beads is then placed vertically between the fiber endface and the imaging optics, so that the camera can image the fiber and the beads alternatively. The transverse position of the slide is adjusted to place a bead in front of the fiber core, while moving the fiber closer. This is repeated until the bead is inserted inside the hollow core. Moving the fiber back should then detach the bead from the slide and retain it inside the hollow core. An optical microscope observation of the DC-HCF endface with the bead inserted is provided in figure 3.1 (c). It is useful to monitor the microstructure,

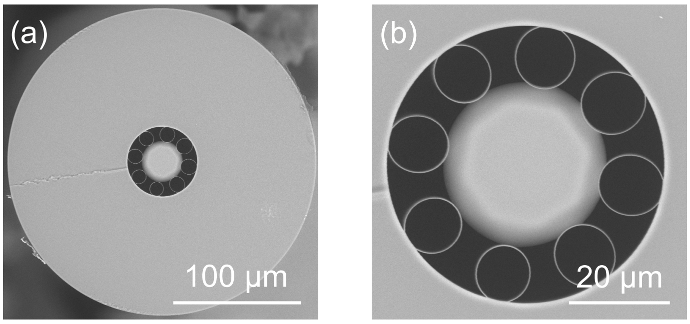

Figure 3.2: *(a) Scanning electron micrograph of a DC-HCF with a silica bead inserted inside its core, with (b) a close-up view on the core region.*

in particular to ensure that no capillary has been damaged in the process. A side image can be performed as well (figure 3.1 (d)) to confirm that the bead is entered sufficiently inside the fiber core.

To prevent the bead from moving, or completely falling off the fiber, it is sealed to the adjacent capillaries with a CO_2 laser (LZM-100, Fujikura). By controlling the duration and power of the applied laser beam, the bead can be spliced without affecting the microstructure of the fiber. This is confirmed by imaging again the tip of the fiber.

Figure 3.2 (a) shows SEM images of the DC-HCF after sealing the silica bead into its core, with a close-up view on the core area (b). It shows that the bead can be inserted and sealed without damaging the microstructure of the fiber. In particular, no capillary was deformed, which means that the transmission should not be affected by the process.

Focal spot size

To evaluate the effect of the bead, we measure again the mode size and compare it to the FM FWHM measured in section 2.2.5. Using the same setup, we image the output mode, at $\lambda = 920$ nm, before and after inserting the bead, shown in figure 3.3 (a) and (b) respectively, denoting a significant spot size reduction induced by the silica bead. Plots along the dashed lines are produced in figure 3.3 (c), showing the mode profile with (red) and without (blue) the bead.

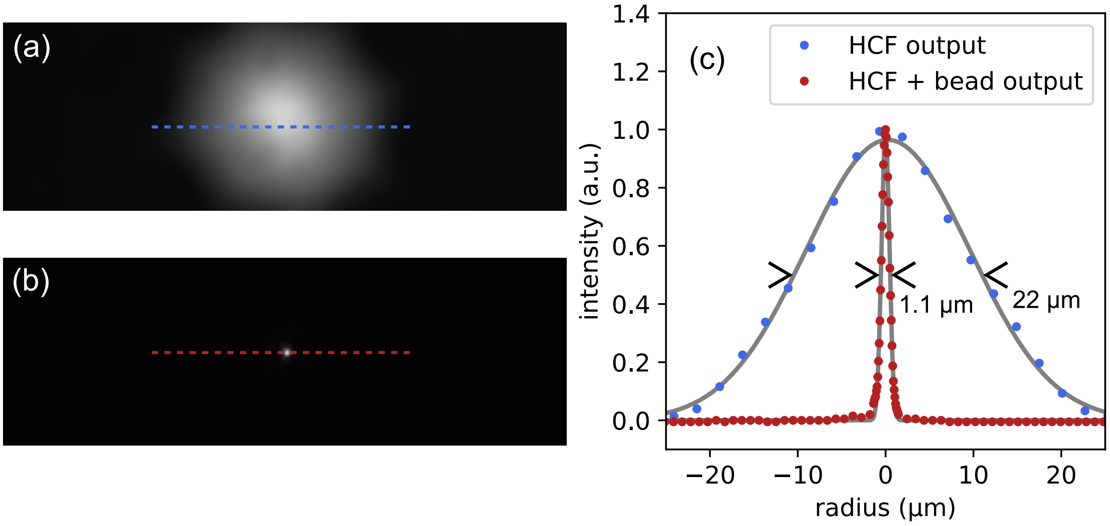

Figure 3.3: *(a) Fundamental mode of the DC-HCF imaged and (b) focalized spot after inserting and sealing a silica bead inside its core, measured at $\lambda = 920$ nm. (b) Plot along the dashed lines for the fiber with (red dots) and without (blue dots) the bead, with a Gaussian fit (solid gray line).*

The spot size (FWHM) is reduced from 22 µm to 1.1 µm, which is acceptable to perform biological imaging in most applications. If realized with bulk optics, such a decrease would have needed large focal length lenses, which is not suitable for micro-endoscopy.

Numerical aperture (NA)

Because the size of the laser spot is reduced by the silica bead, the numerical aperture is correspondingly increased. The NA of the output beam is an important factor to consider in the design of an endoscope to match the distal optics as it will be discussed hereafter. Consequently, we measure the NA, at $\lambda = 920$ nm, with the setup shown in figure 3.4 (a), similar to the one described in section 2.2.6.

To do that, the radius at $1/e^2$ of the maximal intensity is plotted in figure 3.4 (b) (red

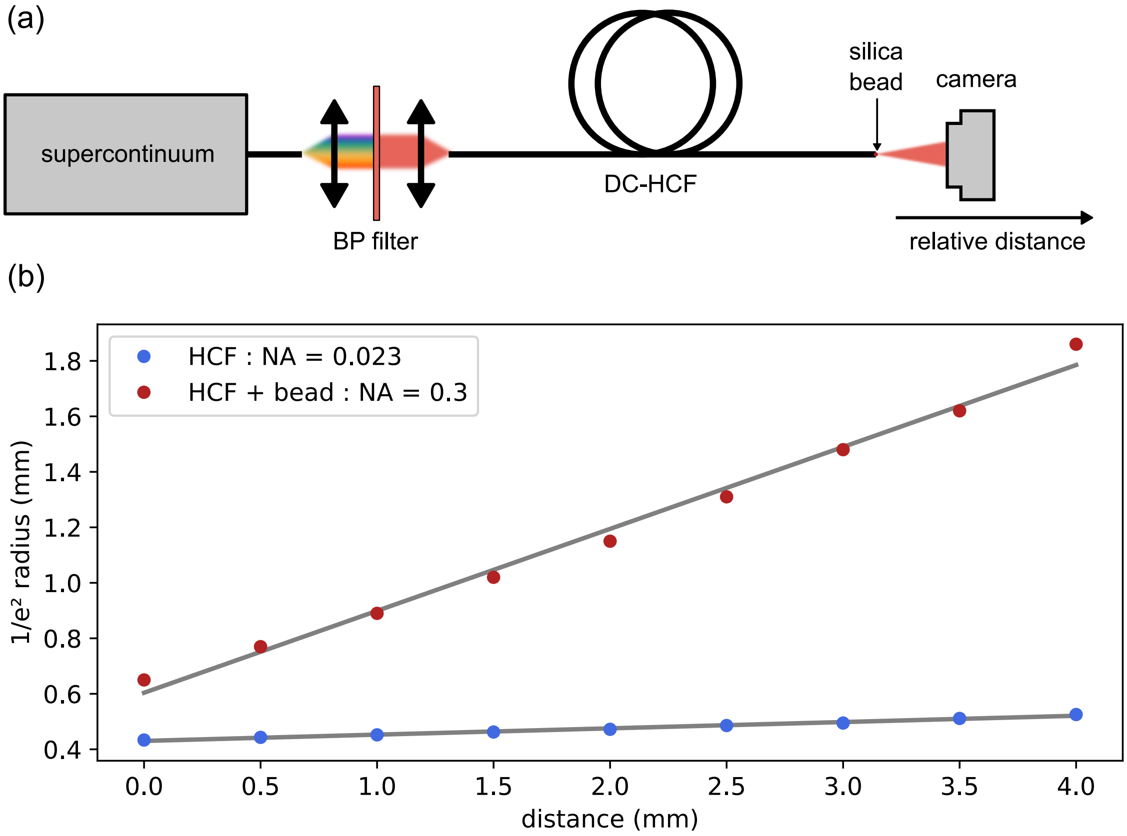

Figure 3.4: *(a) Schematic representation of the setup used to measure the NA of the DC-HCF with a silica bead inserted into its core. (b) Measured* $1/e^2$ *radius as a function of the relative camera position at* $\lambda = 920$ *nm and for the DC-HCF with (red) and without (blue) a silica bead.*

dots) and compared to results obtained previously for the DC-HCF without bead (blue dots). The measured NA, slope of the linear fit (gray line), exhibits an increase of more than an order of magnitude compared to the NA of the fiber without the silica bead. This is a considerable enhancement, and will be addressed in following sections.

3.1.2 GRIN fiber

A substitute for the silica bead is to replace it with a GRIN lens spliced at the end of the fiber. A GRIN lens is a GRIN fiber of a specific length designed to act as a convergent lens by exploiting the spatial self-imaging mechanism.

Design and fabrication

Spatial self-imaging (SSI) is a particular property that can be exploited with GRIN fibers. It leads to a periodic oscillation of the beam spatial distribution along the propagation [108]. An input field is reproduced periodically at equally spaced distance z_{SSI} during propagation [109]. This distance is characteristic to the GRIN fiber, more specifically to the radius and index difference of the fiber, and will be called hereafter period of SSI. Consequently, if the GRIN fiber length is a multiple of z_{SSI}, the output will reproduce the input shape of the field.

Using the model described in [110], we performed numerical simulations of a multimode propagation inside a GRIN fiber. A 2D profile of the modal distribution as a function of the propagation distance z is represented in figure 3.5 for $\lambda = 920$ nm. The

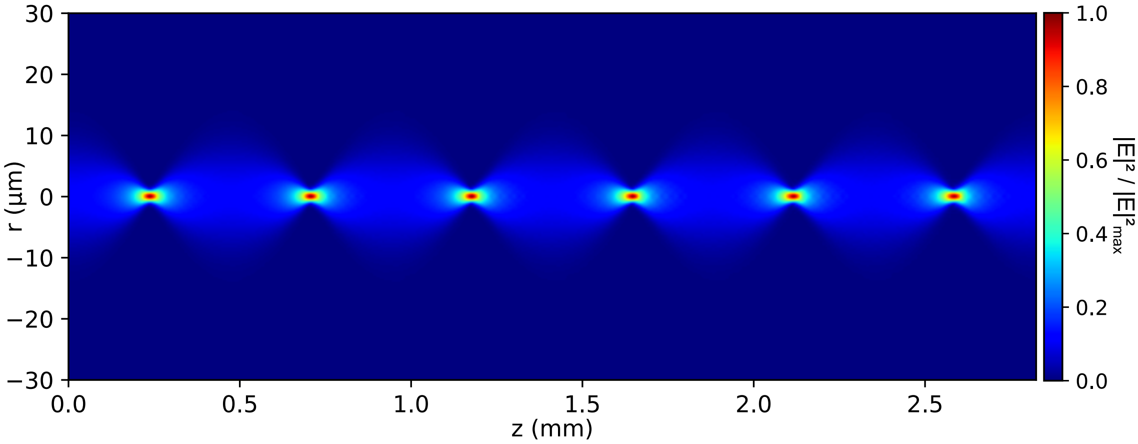

Figure 3.5: *Numerical simulations of the light intensity profile along the propagation distance z inside a GRIN fiber, based on the model from [110]. The input mode has a 22 µm FWHM. The GRIN fiber has a 30 µm core radius and a* 30.10^{-3} *index difference between core and cladding.*

GRIN fiber has a parabolic profile defined as such :

$$n(r)=\begin{cases} n_{\text{core}}-(n_{\text{core}}-n_{\text{clad}}).\left(\frac{r}{r_{\text{core}}}\right)^2, & \text{if } r \leqslant r_{\text{core}} \\ n_{\text{clad}}\,, & \text{if } r > r_{\text{core}} \end{cases} \tag{3.1}$$

where n_{core} and n_{clad} are the refractive indices of the core and cladding of the GRIN fiber, and r_{core} is its core radius. We fixed $n_{\text{core}} = 1.4815$ and $n_{\text{clad}} = n_{\text{core}} - 30.10^{-3}$ at 920 nm, which corresponds to the commercial germanium doped preform that we used for the GRIN fiber fabrication. We also set the GRIN fiber radius to $r_{\text{core}} = 30$ µm. The simulation was performed for an input mode of 22 µm in diameter (FWHM) to match the fundamental mode size measured previously for the DC-HCF (see section 2.2.5).

The SSI period can then be calculated using the following formula [111] :

$$z_{\text{SSI}} = \pi r_{\text{core}} \sqrt{\frac{n_{\text{core}}^2}{n_{\text{core}}^2 - n_{\text{clad}}^2}} \tag{3.2}$$

In our case, it results in a SSI period of $z_{\text{SSI}} = 470$ µm. Indeed, we observe in figure 3.5 that the input profile is periodically repeated at every multiple of this period, and is reproduced at the output after six full periods. In addition, for a propagation distance z of half the SSI period[1], the field intensity is restricted to a much smaller mode profile. Consequently, if the GRIN fiber length is set to $L_{\text{GRIN}} = \frac{z_{\text{SSI}}}{2}$, or every odd multiple of it, the output beam of the fiber will be a lot smaller than its input. In this manner, the GRIN fiber would act similarly to a convergent lens, and thus could be called a GRIN lens. We further emphasize on this phenomenon by showing in figure 3.6 the simulated field intensity profile inside and at the output of a GRIN fiber with a length equal or smaller than half its SSI period. Propagation along the direction z is represented with $z = 0$ being the input of the GRIN fiber. The GRIN fiber core is illustrated by a light translucent rectangle, and the smallest field profile size, and highest intensity, is marked with a white dashed line.

First we focus on the case where $L_{\text{GRIN}} = 235$ µm, which in our case is half the SSI period. In this instance, the focal spot is exactly positioned on the GRIN fiber output facet and has a FWHM of 2.8 µm. As stated above, the input beam has a diameter of 22 µm (FWHM), and it is thus decreased by about an order of magnitude by the GRIN lens. Although the de-magnification factor is still smaller than the one measured when using the silica bead, the reduction in mode size achievable with this method is still significant.

Moreover, the flexibility provided by the GRIN lens functionalization outperforms the silica bead described above. As a matter of fact, the silica bead diameter is contained

---

[1] Or more generally for $z = (m + 0.5)\, z_{\text{SSI}}$, with m being an integer.

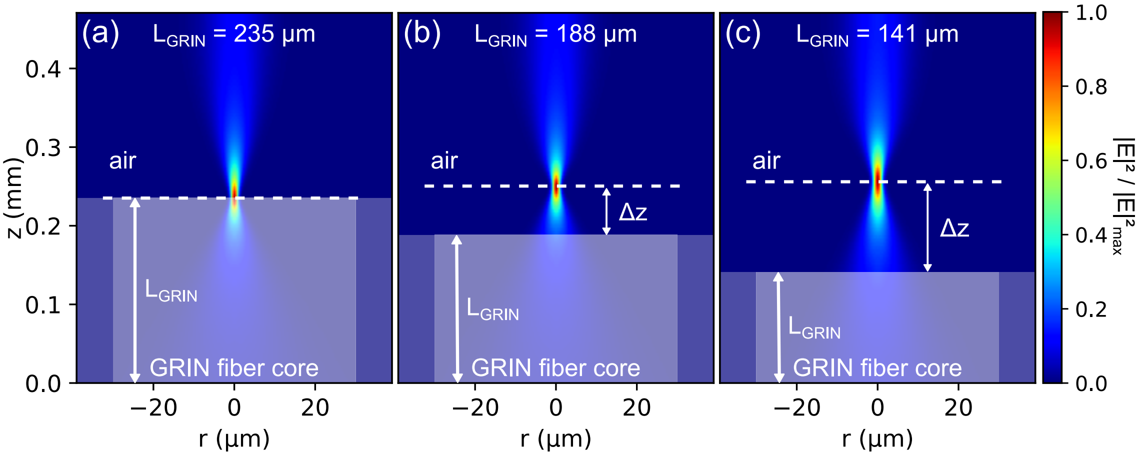

Figure 3.6: *Numerical simulations of the light intensity along the propagation distance z at the output of the HCF ($z = 0$) for different GRIN fiber lengths L_{GRIN}, based on the model from [110]. The light rectangle is the GRIN fiber core, the dashed white line is the position of the focused spot and Δz is its distance from the GRIN fiber endface.*

in a very small range by the dimensions of the hollow core, and no other parameter can be adjusted to tweak the focal spot size and/or position. With the GRIN lens however, both these parameters can be addressed by changing the length of the GRIN fiber used. First, figure 3.6 shows that when reducing L_{GRIN}, the focal spot is moved away from the GRIN fiber endface, *i.e.* Δz increases.

This evolution, shown in figure 3.7 (a), is almost linear for the range of GRIN fiber length observed, and can grant a distance between the focus spot and the GRIN fiber surface of 100 to 200 µm. These simulations also show an increase in focus spot size (FWHM) that can be controlled with the GRIN fiber length (gray line in figure 3.7 (b)). The black vertical dashed line in figure 3.7 represents half the period of SSI, in our case $L_{\mathrm{GRIN}} = 235$ µm. As expected, simulations show that this value provides the smallest spot size (2.8 µm FWHM) and no gap between the focus spot position and the GRIN fiber surface ($\Delta z = 0$).

Because the spot size at the output of the fiber is decisive in determining the endoscope performances, we demonstrate experimentally the righteousness of these results in figure 3.7 (b) (blue dots). For this, we first drew a commercial germanium-doped preform to a GRIN fiber with a 30 µm core radius and a 30.10^{-3} refractive index difference between the core and cladding. It also has a 300 µm outer diameter, fitting that of the DC-HCF, for fabrication ease. The GRIN fiber was spliced to the DC-HCF using a CO_2 laser fiber splicer (Fujikura LZM-100), then cleaved a few hundreds of micrometers away from the splice. A specific L_{GRIN} is then obtained by polishing the GRIN fiber surface and measured with a side-view image acquired by an optical microscope. An example

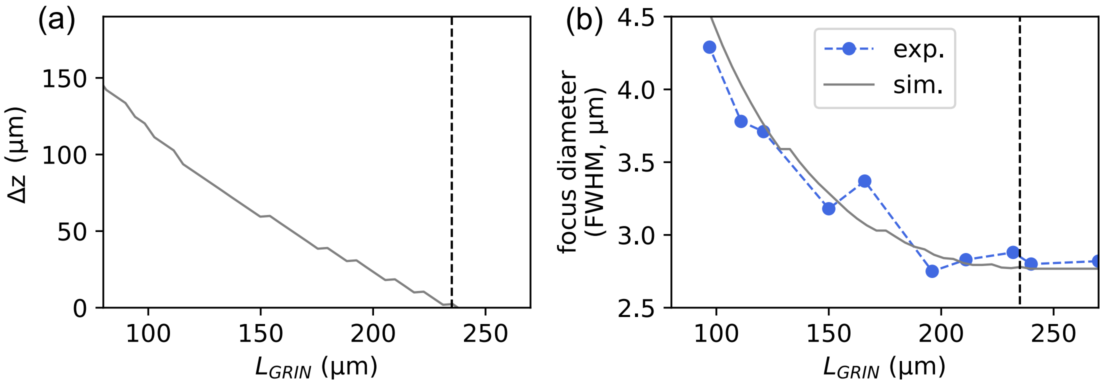

Figure 3.7: *(a) Simulated distance between the focal spot and the GRIN fiber endface as a function of the GRIN fiber length* L_{GRIN}. *(b) Focal spot size (FWHM) as a function of the GRIN fiber length* L_{GRIN}, *measured (blue dots) and simulated with the model from [110] (gray solid line). The vertical black dashed line corresponds to half the SSI period (i.e.* $z_{SSI}/2$*).*

of such an image is shown in figure 3.8 (a). Measurements of the focus spot FWHM with respect to the GRIN fiber length, represented in figure 3.7 (b) (blue dots), are obtained by successive polishing of the GRIN fiber followed by a spot size measurement with the setup described in section 2.2.5. The experimental data confirms the simulations, and both show an increase in spot size of up to a factor 2 for the range of L_{GRIN} probed.

Similarly to the bead integration inside the fiber, we can ensure that the fabrication process to splice the GRIN lens at the tip of the HCF did not affect the fiber microstructure. Indeed, the GRIN fiber end surface can be imaged with an optical microscope,

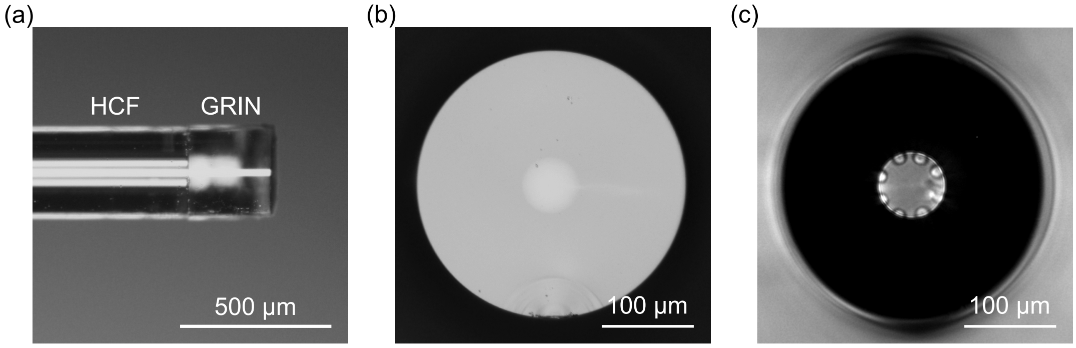

Figure 3.8: *(a) Side view of the GRIN fiber spliced to the DC-HCF then polished, observed with an optical microscope. Image of (b) the GRIN fiber endface and (c) the DC-HCF / GRIN fiber interface, observed with an optical microscope by adjusting the focal plane.*

as shown in figure 3.8 (b). Adjusting the microscope focus plane allows to image the interface between the DC-HCF and the GRIN fiber, as shown in figure 3.8 (c). Although the microstructure is not defined as clearly as when imaging the HCF structure in itself, individual capillaries are distinguishable, which is sufficient to ensure that no major damage was induced.

Finally, we shine a light on some other advantages of using this functionalization method. In particular, the fabrication is less delicate and leads to a more robust design over time. It also has the convenience of sealing the fiber output which prevents outside intrusion (dust, humidity) and allows the surface to be cleaned if needed.

Focal spot size

As it was stated above, the spot size measurements at the output of the HCF functionalized with a GRIN lens is realized with the setup described in section 2.2.5. The imaged fundamental mode of the HCF is displayed again in figure 3.9 (a) and compared to the spot obtained with the addition of a GRIN lens with a length of $L_{\text{GRIN}} = 130\ \mu\text{m}$ (figure 3.9 (b)). This value is not chosen arbitrarily, and the reasons for this decision will be detailed in section 3.7.1. Plots along the dashed lines are represented in figure 3.9 (c) for the HCF alone (blue dots), and with the GRIN lens spliced (red dots). A Gaussian fit on the experimental data, represented by the gray solid lines in figure 3.9 (c), provides

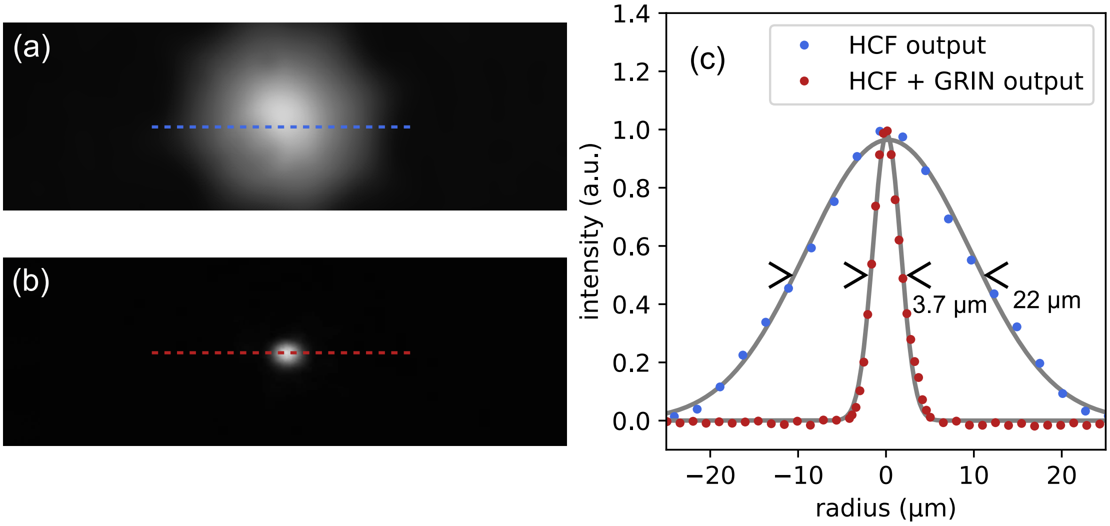

Figure 3.9: *(a) Fundamental mode of the DC-HCF imaged and (b) focalized spot after splicing the GRIN fiber to the HCF and polishing it to a 130 µm length, measured at $\lambda = 920$ nm. (b) Plot along the dashed lines for the fiber with (red dots) and without (blue dots) the green lens, with a Gaussian fit (solid gray line).*

the FWHM measurements.

The mode size reduction provided by this method is significant and almost reaches an order of magnitude, with a FWHM of 3.7 µm after functionalization of the fiber. Still, this spot size is a bit too large for imaging applications, especially compared to the results obtained with the silica bead functionalization. Nevertheless, this can be corrected when re-imaging the spot onto the sample, as will be described below.

Numerical aperture (NA)

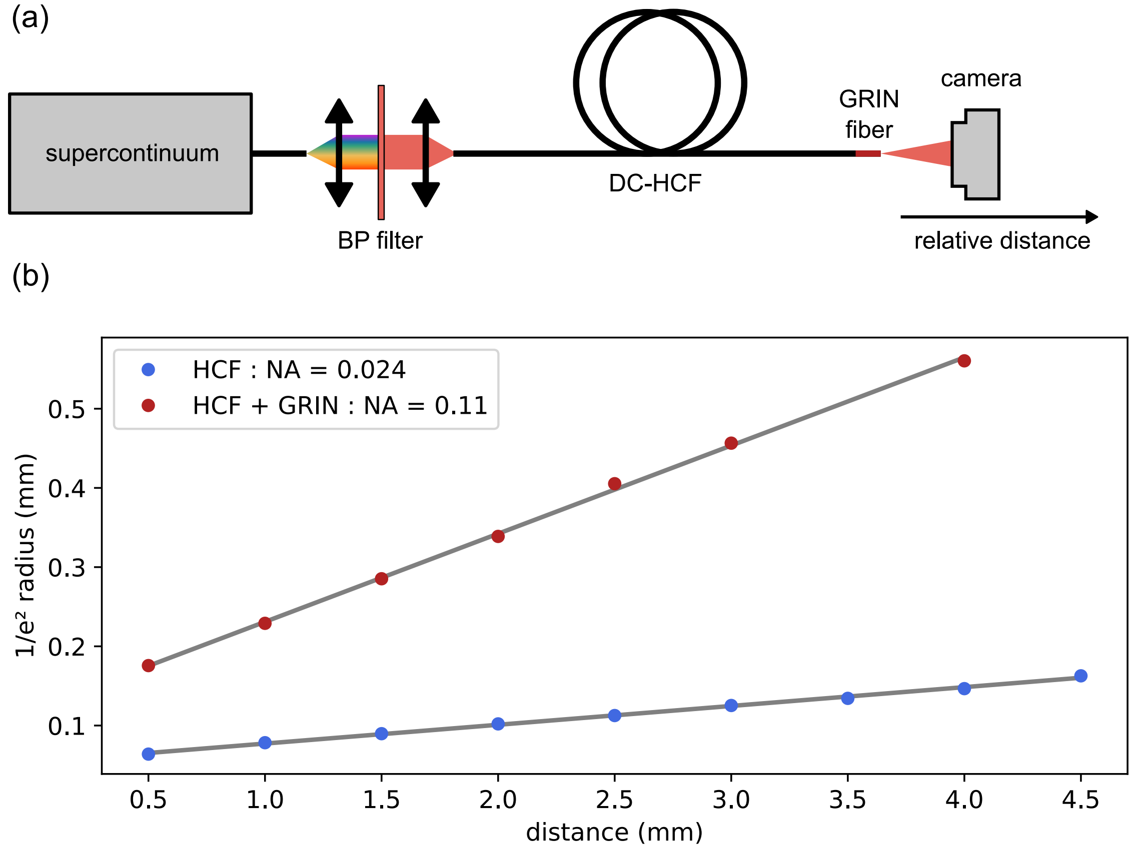

Figure 3.10: *(a) Schematic representation of the setup used to measure the NA of the DC-HCF with a GRIN lens spliced at its distal end. (b) Measured* $1/e^2$ *radius as a function of the relative camera position at* $\lambda = 920$ *nm and for the DC-HCF with (red) and without (blue) the GRIN lens.*

The NA at the output of the GRIN lens is measured with the setup represented in figure 3.10 (a), with a 920±5 nm bandpass filter fixing the wavelength. The radius (at $1/e^2$ of the maximal intensity) of the far field with respect to the camera position is depicted in figure 3.10 (b) for the DC-HCF before (blue dots) and after (red dots) splicing the GRIN lens. The measured NA is retrieved with a linear fit, and values are exhibited in the legend of figure 3.10 (b).

Because the spot size reduction is not as considerable as it is with the silica bead, the NA do not reach such a high value. The two functionalization techniques reached different results, each having its own advantages. It seems that both method could be employed in an endoscopy scheme depending on the requirements to be met.

As a summary, the beam properties at the output of the endoscopic fiber and for both functionalization methods are joined in the following table :

	HCF	**bead**	**GRIN**
spot size (µm)	22	1.1	3.7
NA	0.024	0.3	0.11

3.2 Micro-objective

Regardless of the fiber tip functionalization method, the focal spot is inherently located very close to the fiber endface, up to a few dozens of micrometers away. Yet microscopy standards provide a working distance (WD), meaning the distance between the optics and the imaging plane, up to several millimeters. To increase the working distance of the endoscope, so as to get closer to microscopes performances, additional optics need to be embedded to the distal design. In addition, distal optics can further decrease the laser spot size at the output of the endoscope, called PSF and measured at FWHM, with a magnification factor < 1. This should be of particular importance for a GRIN lens functionalization of the HCF, as the spot size reduction is less significant than for the silica bead functionalization. However, because the scanning mechanism will be applied to the fiber, the magnification factor of these optics will also apply to the scanning pattern, and could restrict the field of view (FoV, width of the scanned area on the sample) of the endoscope. Consequently, a compromise must be made on the magnification factor to provide a small enough spot size, for high resolution imaging, and a large enough field of view.

In this scope, we propose two different designs of distal optics combined to form so-called micro-objectives: an objective formed with four micro-lenses designed to be coupled with the silica bead functionalization, and one based on a GRIN fiber specifically made to be joined with the GRIN lens functionalization.

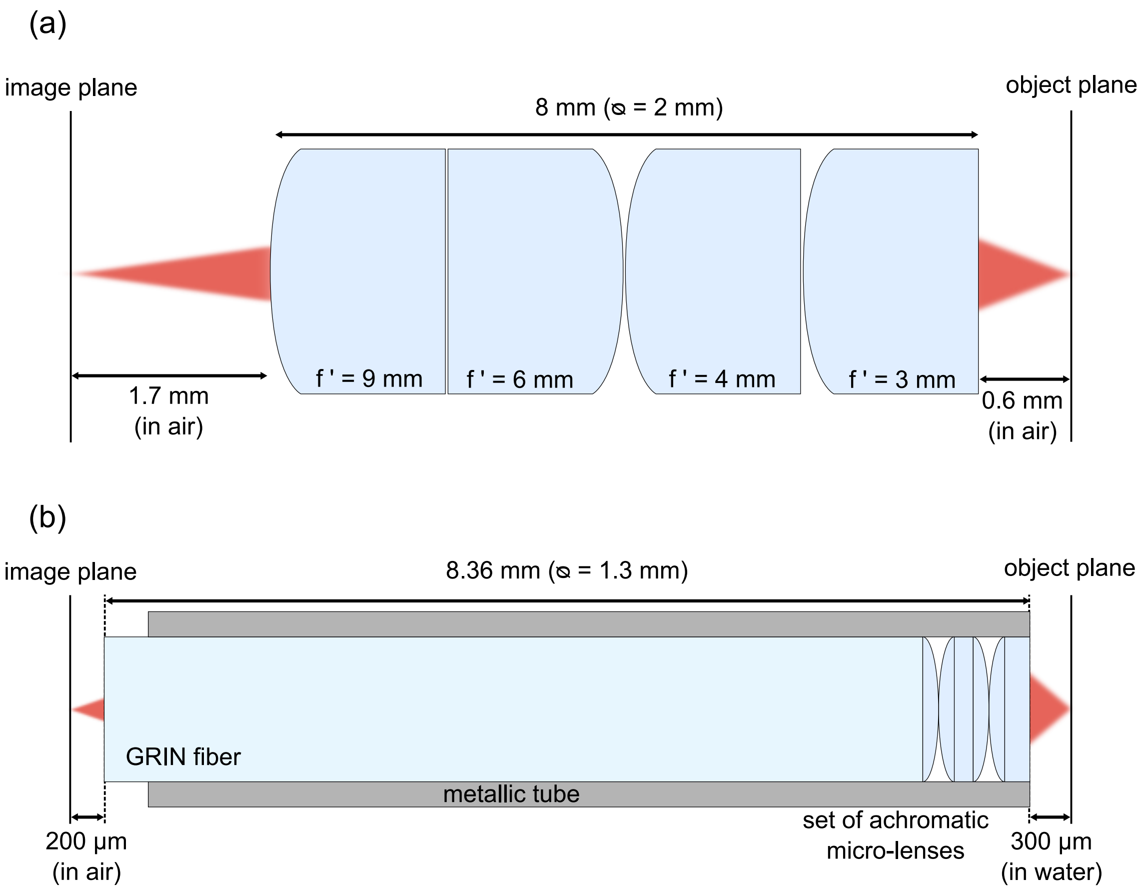

Figure 3.11: *Schematic representation of the micro-objectives inserted and fixed into the endoscope head, based on (a) four micro-lenses or (b) a GRIN fiber. The image plane is the laser spot at the output of the endoscopic fiber, and the object plane is the plane to image inside the sample.*

Micro-lenses objective

The first design we implemented is a combination of four achromatic doublets, based on [35]. The disposition of the lenses is schematically represented in figure 3.11 (a). The four micro-lenses have an image focal distance f' of 9 mm (Edmund Optics 83-338), 6 mm (Edmund Optics 65-569), 4 mm (Edmund Optics 65-568), and 3 mm (Edmund Optics 65-567). It has a total length of 8 mm for a 2 mm diameter, small enough to be integrated into a compact endoscope head.

The objective was designed to provide a 0.63 magnification ratio (from the image plane to the object plane) and a 600 µm working distance (WD) on the object side, which is the output of the endoscope. The WD on the image size, *i.e.* distance from the fiber to the objective, is 1.7 mm. The NA is 0.45 on the object side and 0.3 on the image side. This micro-lenses design is a good compromise for an input spot already small enough to provide high-resolution imaging, in our case supplied with the silica bead functionalization, and a FoV that is not much reduced. However, it does not yield a small enough magnification ratio for it to be combined with a GRIN lens functionalization. For this reason, the micro-lenses objective will henceforth be combined only to a DC-HCF with a silica bead inserted inside its core.

GRIN fiber objective

An alternative to the micro-lenses assembly is a GRIN micro-objective. For this, commercial products are readily available, and designed for endoscopy applications. In our case, we chose a GRIN fiber objective from GRINTECH GmbH (GT-MO-070-016-ACR-VISNIR-30-20), represented in figure 3.11 (b)[2]. Its main advantage is a 0.22 magnification ratio, fitting requirements for the GRIN lens functionalization of the HCF. The objective diameter is also much smaller (1.3 µm), which could allow even smaller endoscopic probes.

The drawbacks of this objective is the decrease of the FoV with the magnification ratio, and a smaller WD (300 µm in water, corresponding to 225 µm in air, on the object side). On the other hand, the NA of the objective is 0.7 on the object side, much larger than the micro-lenses one, increasing the collection efficiency of the endoscope. On the fiber side, the WD is 200 µm and the NA 0.22.

In summary, a comparison of the optical properties for each micro-objective is provided in the following table :

micro-objective	**magni-fication**	**NA (obj.)**	**NA (im.)**	**WD (obj.)**	**WD (im.)**
lenses	0.63	0.45	0.3	600 μm	1.7 mm
GRIN	0.22	0.7	0.16	300 μm (in water)	200 μm

3.3 Resonant fiber scanning device

The scanning device implemented inside the endoscope head is based on a piezo-electric tube and offers a cost-efficient and very small solution. Consequently, it has

---

[2] Redrawn from the manufacturer data sheet.

been widely used for endoscopy applications [15, 19, 54, 79, 80]. The scanning device and its driving were not developed in the context of this thesis. Therefore, the results presented in this section originate from the work of Guillaume Ducourthial during its PhD thesis [81], later revised by Alberto Lombardini [35] and Vasyl Mytskaniuk [36].

We used a 10 mm long, 0.9 mm inner and 1.5 mm outer diameter piezoelectric tube from Physik Instrumente. The tube is made of a ceramic material (PIC255) and four isolated electrodes (Copper Nickel, CuNi) placed on its outer surface, forming two pairs of diametrically opposed electrodes. These pairs set two orthogonally oriented directions, x and y, that can be addressed separately with two driving voltage, V_x and V_y.

The piezoelectric tube is set around the fiber and its movements are passed along to the fiber through the intermediary of two ceramic custom-made parts, glued to both the fiber and the piezo tube. For low voltages (<50 V), the displacement of the tube is in the micrometer range, but the fiber tip can reach an amplitude of oscillation of several hundreds of micrometers when the driving signal is set to the mechanical resonance frequency of the fiber. This frequency f_{res} depends on the fiber material, diameter, air fraction, the length of fiber that protrudes from the tube, and the direction of applied tension. When exciting the two axes resonantly, one can achieve a circular motion, that can be turned into a spiral pattern by adding an amplitude modulation.

If we consider the system to be ideal, which in our case means that the movement of the fiber in response to a specific voltage is the same for both axes, a circular pattern is achieved by driving both axes of the piezoelectric tube with sinusoidal waves at the frequency f_{res} and with a $\pi/2$ phase difference. The driving voltages can then be defined as :

$$V_x(t) = V_{max} \,.\, \sin(2\pi f_{res}\, t) \tag{3.3a}$$

$$V_y(t) = V_{max} \,.\, \cos(2\pi f_{res}\, t) \tag{3.3b}$$

with V_{max} the amplitude of oscillation, and t the time variable.

To transform the fiber tip movement into an expanding spiral pattern, a modulation of the amplitude is added. A simple example is a slowly varying envelope such as $\sin(2\pi f_{mod}\, t)$ oscillating at a frequency $f_{mod} \ll f_{res}$. The driving voltages thus become :

$$V_x(t) = V_{max} \,.\, \sin(2\pi f_{mod}\, t) \,.\, \sin(2\pi f_{res}\, t) \tag{3.4a}$$

$$V_y(t) = V_{max} \,.\, \sin(2\pi f_{mod}\, t) \,.\, \cos(2\pi f_{res}\, t) \tag{3.4b}$$

Because the sampling for each circle remains constant, sampled points draw away from each other on the edge of the spiral. A sinusoidal modulation of the driving signals, rather than a linear one, is then preferred to balance the sampling density throughout

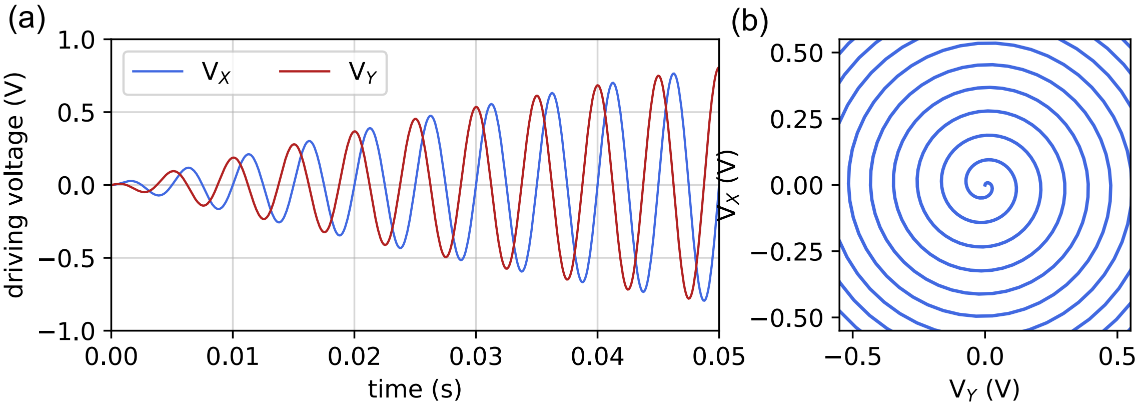

Figure 3.12: *(a) Example of sinusoidal driving signals in x (blue) and y (red) directions to produce a spiral scan (b). Both axes are driven with a resonant frequency* $f_{\text{res}} = 200$ *Hz, and a* $\pi/2$ *phase difference.*

the spiral scan, decreasing the distance between circles when moving away from the spiral center.

An example of such driving voltages and the spiral expanding pattern produced is represented in figure 3.12 (a) and (b) for $f_{\text{res}} = 200$ Hz, $f_{\text{mod}} = 3$ Hz and $V_{\text{max}} = 1$ V. Once the spiral scan is performed, the fiber needs to be brought back to its original steady position before starting another scan. Fiber relaxation can be accomplished through friction, with no driving needed ($V_{\text{x}} = V_{\text{y}} = 0$). However, it is much faster to perform this with a so-called active breaking, during which both axes are driven with a phase inversion. The driving during these steps is represented in figure 3.13 for a resonant frequency of $f_{\text{res}} = 100$ Hz, with $f_{\text{mod}} = 0.5$ Hz and $V_{\text{max}} = 1$ V. The modulation frequency for the breaking phase is chosen to be 5 times higher than for the scan phase (*i.e.* 2.5 Hz), to decrease the breaking phase duration and therefore increase the overall acquisition rate. The breaking phase is usually followed by a rest phase during which no driving is applied to either axis. This step is not mandatory, but ensures the fiber is still before starting the next cycle.

The driving signals described hereafter consider the ideal scenario where the material response is identical for both axis. In reality, a mismatch between the measured resonant frequencies of both axes, $f_{\text{res,x}}$ and $f_{\text{res,y}}$, is inherently present. A mismatch below 1 % (a few Hz in our case), where the resonant frequency is set between $f_{\text{res,x}}$ and $f_{\text{res,y}}$, is acceptable but a greater mismatch generally leads to distortions of the scanning pattern and a hassle to obtain a large FoV.

To apply these waveforms in a real setup, the laser spot at the output of the endoscope is imaged onto a position sensing detector (PSD, PDP90A, Thorlabs). The position

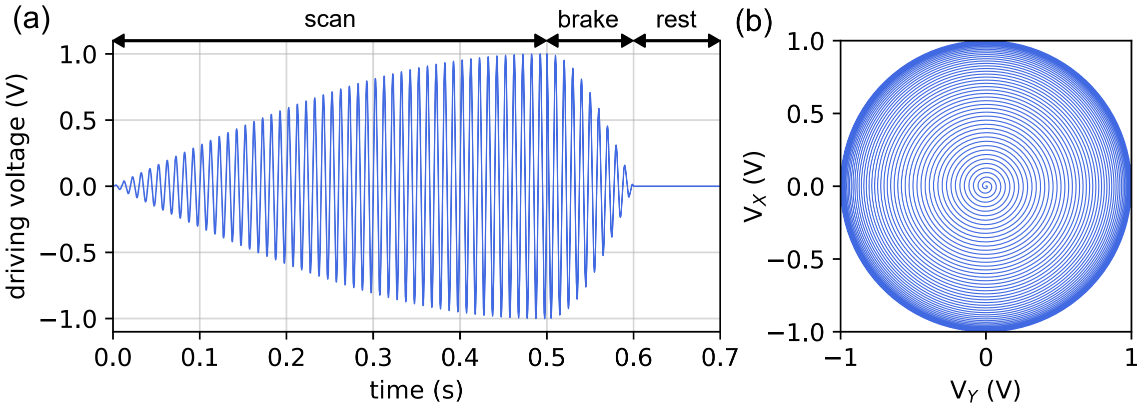

Figure 3.13: *(a) Example of excitation signal for a full image acquisition cycle that produces the spiral pattern of (b). The scan phase, or expansion phase, is followed by an active braking phase during which both axes are excited in anti-phase, then a rest time with no driving applied.*

of the spot over a scanning cycle is displayed using a custom Labview or python software and can be modified by adjusting the parameters mentioned above. First, the driving frequency must be set to fit the resonant frequency of the fiber. This is performed by fixing the driving amplitude V_{max}, and fine-tune the driving frequency until the amplitude of the scan is maximal. In our case, the resonant frequency of a fiber with a freestanding length of 11 mm is about 1800 Hz. Figure 3.14 (a) shows the outline of a scan measured with this driving frequency. The red line is a circle fit of the measured points, and allows us to ensure the circular shape of the scanned area.

In addition, the driving amplitude V_{max} is adjusted to obtain different FoVs, and the modulation frequency f_{mod} determines the acquisition rate. The modulation frequency of the breaking phase is set to be as high as possible to reduce the breaking duration. Figure 3.14 (b) and (c) show the braking phase pattern and position on both axes respectively. It shows that by tuning each parameter with a live visualization, a breaking phase of only a few oscillations is attainable, leaving most of the scanning cycle duration to the scan phase. It also ensures that the fiber remains still after the breaking phase, which avoids distortions at the start of the next scan.

Ultimately, the acquisition speed and FoV allowed by this device are limited by the resonant frequency of the fiber. Because the frequency of the driving signals is fixed by the resonant frequency of the fiber, changing the acquisition rate, via the modulation frequency, only sets the number of circles formed during the spiral scan, *i.e.* the number of oscillations on both axes. The FoV however, is set by adjusting the amplitude V_{max}. Increasing the FoV upscales the spiral pattern while maintaining the number of circles, inherently increasing the distance between consecutive circles. For a proper sampling, this distance should be as small as half the PSF. For instance, if we fix $f_{\mathrm{res}} = 1800$ Hz,

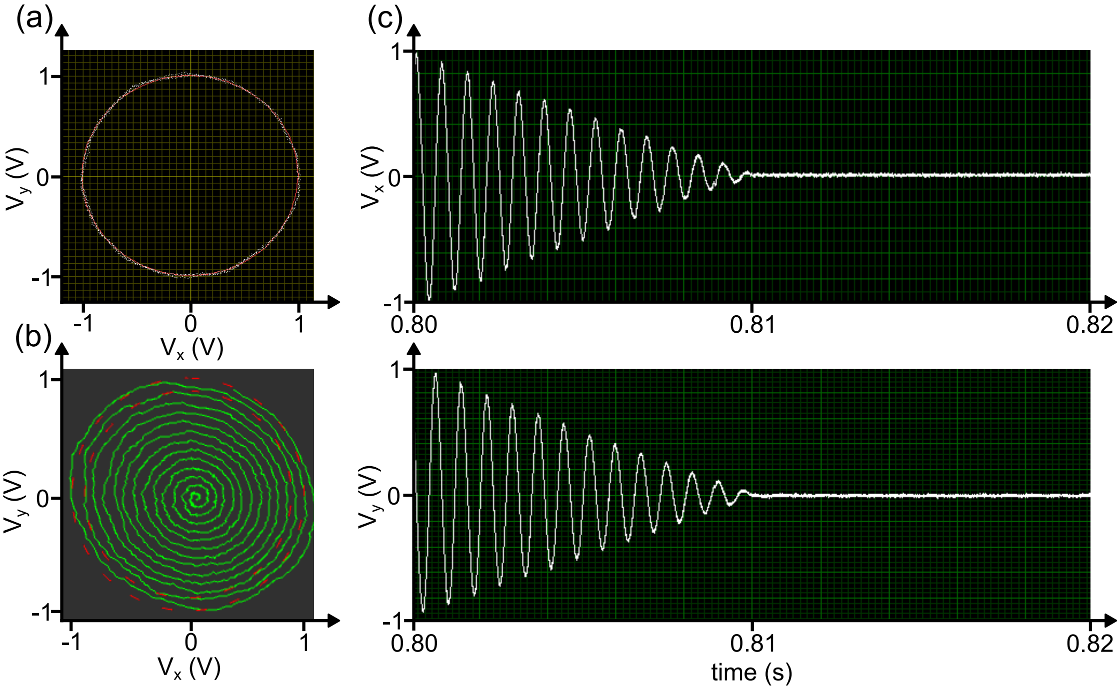

Figure 3.14: *Example of (a) scanning pattern contour, (b) breaking phase pattern and (c) breaking phase position in x (top) and y (bottom) directions, measured with a position sensing detector (PSD). (a) and (c) subfigures were acquired with a custom Labview software, and (b) with a custom python software.*

with a FoV of 200 µm and an acquisition rate of 10 frames per second (FPS), the distance between consecutive circles (in the imaging plane and for the GRIN fiber objective) is 556 nm. In addition, this distance also has to be smaller than the pixel size of the rendered image to ensure that all pixels on the image are sampled. If we consider again the previous example, it leads to a maximal image size of 360x360 pixels. This should be considered when numerically reconstructing images. To summarize, here are the sampling rules capping the performances of the endoscope :

$$\frac{FoV.AR}{2.f_{\text{res}}} \leqslant \frac{PSF}{2}, \qquad\qquad N \leqslant \frac{2.f_{\text{res}}}{AR} \tag{3.5}$$

with AR the acquisition rate, or number of images acquired per second, and N the width of the rendered image in pixels.

3.4 Numerical acquisition

To operate the endoscope, a combination of electronic devices is needed. Figure 3.15 summarizes the different parts of this arrangement and their entanglements. First, to drive the piezoelectric tube, four analog signals are needed, one for each electrode. These are brought by two separate terminal blocks (BNC-2110, National Instruments), both connected to the same acquisition card (PCIe-6363, National Instruments) inside the control computer. The four signals are amplified (E-835.00, National Instruments) before being relayed to the piezoelectric tube, as the acquisition card provides too weak voltages (±5 V). A third terminal block is used as a power supply for the PSD (PDP90A, Thorlabs), and is connected to another acquisition card. The PSD has three numerical outputs, namely x, y and $x+y$, that allow to reconstruct the spot position at any given time. Finally, the signals collected by the optical fiber are detected with a photo-multiplier (PM, H7422-40, Hamamatsu) that also sends a numerical signal. It grants access to the nonlinear signal evolution over time. All numerical signals are relayed to one of the acquisition cards through either of the terminal blocks.

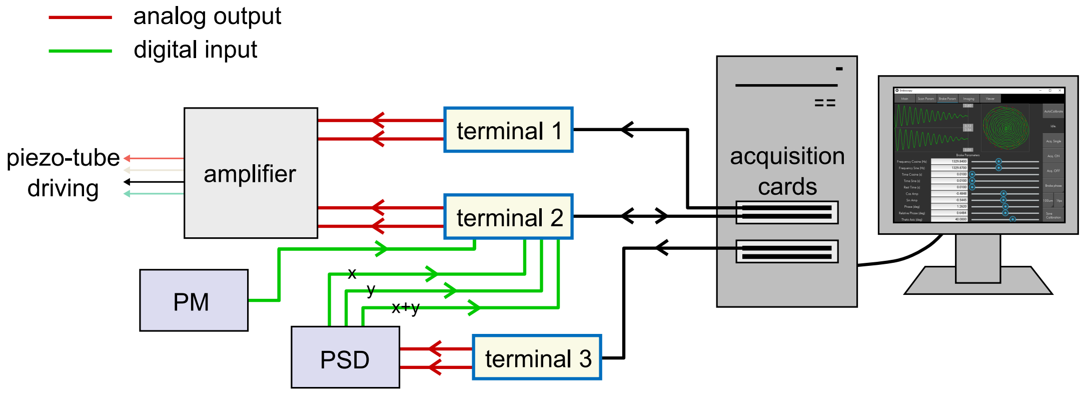

Figure 3.15: *Arrangement of the electronic components for numerical acquisition in the endoscopy setup. It drives the piezoelectric tube scanner, records the nonlinear signals detected by the photo-multiplier, allows calibration of the scanner via a PSD, and reconstructs images with a custom python (or Labview) software.*

The electronic setup is operated by a custom-made software, of which two equivalent versions have been developed, based on python and Labview respectively. A calibration of the scanner is mandatory to obtain a proper spiral pattern and a short active break. It is performed by adjusting parameters detailed in the previous section, for the scan and break phases separately. To correlate the driving voltage amplitude $V_{\max}$ with the actual FoV produced, the latter is measured using a chart (R1DS1, Thorlabs) for an arbitrary value of $V_{\max}$. After that, the FoV can be freely decided with appropriate value of $V_{\max}$, as long as the driving frequency remains unchanged.

As it was mentioned above, the FoV and AR can be easily defined by appropriately setting the driving parameters, although a full calibration is essential for each FoV/AR combination. Once the calibration is complete, the 2D position of the spot is recorded during a spiral scan. These position-over-time values are saved and will be used to reconstruct images in real-time. Thus, several calibrations can be saved beforehand, allowing to quickly switch FoV and/or AR during imaging. Ideally, the scanner calibration has to be routinely readjusted. It avoids any distortion in images reconstruction, as the fiber response to the resonant excitation can slightly drift over time. Lastly, the custom software can display a mean over several frames, thus increasing the imaging contrast, which can be of particular interest for weakly emitting samples or tissues.

3.5 Endoscopic head

All distal elements detailed in this chapter are encased inside a bio-compatible stainless steel tube, forming the endoscopic head. It has a 2 mm inner diameter, a 3 mm outer diameter and a 40 mm length. The piezoelectric tube is glued on both ends to ceramic pieces that transmit the vibrations to the fiber on which they are glued as

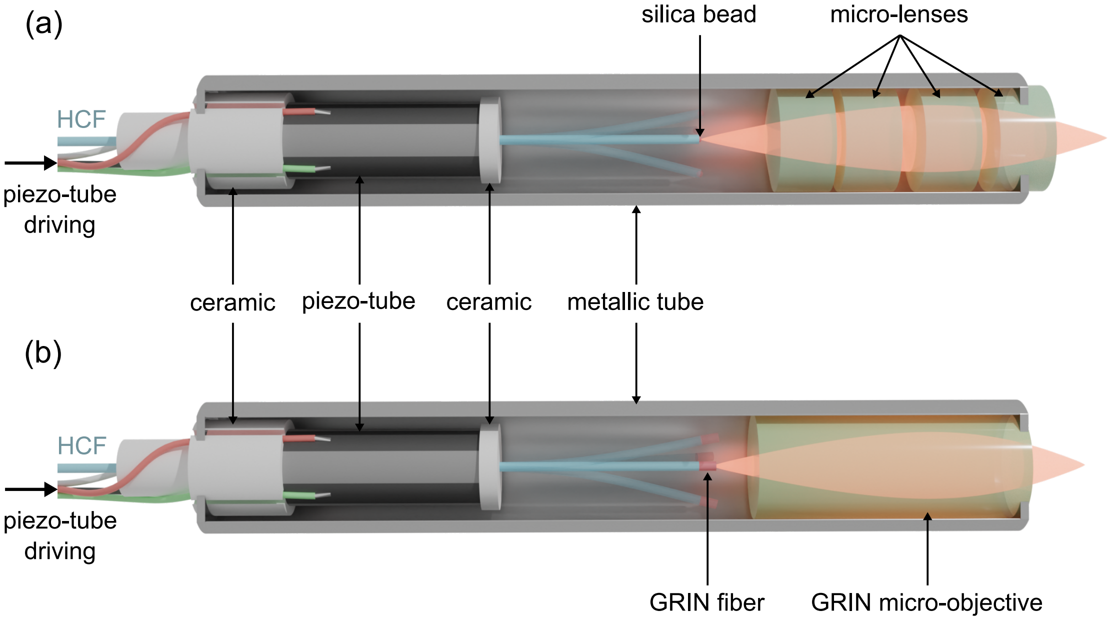

Figure 3.16: *Schematic representation of the two endoscopes fabricated and tested in this work, based on the combination of (a) a silica bead functionalization of the fiber tip and a micro-lenses objective, or (b) a GRIN fiber functionalization of the fiber tip and a GRIN fiber based micro-objective.*

well. Four conduits are carved into the proximal ceramic piece, leading the electrical wires to the four electrodes of the piezoelectric tube. The wires are then soldered to the appropriate electrodes with particular attention to the welding size, which should not exceed the ceramic piece outer diameter to avoid short-circuits[3].

Two endoscope schemes arise from the results presented above. The first one, represented in figure 3.16 (a), has a silica bead inserted and sealed inside the hollow core of the DC-HCF, and four micro-lenses fixed inside a separate bio-compatible stainless steel tube (not shown in figure 3.16 (a)), which is itself settled inside the main tube. As explained above, a 0.3 NA is reached after the bead functionalization, which means that the beam is rather large at the input of the micro-lenses objective. During the scan, especially on the edges of the spiral, it could lead to some clipping of the excitation source, meaning that the beam is too large to be collected entirely by the objective. It is then required to increase the average power of the excitation source to achieve a comparable nonlinear signal generation.

The second one (depicted in figure 3.16 (b)) includes a GRIN fiber spliced to the distal tip of the DC-HCF, and a commercial GRIN fiber based micro-objective. Likewise, the micro-objective is set inside a separate bio-compatible stainless steel tube of 2 mm outer diameter that protrudes from the main tube, on which it is glued. Because the NA at the output of the fiber with a GRIN lens functionalization is much lower than with the bead, and because the GRIN fiber micro-objective is much closer to the fiber endface, the beam at the input of the objective is in this case much smaller. The clipping of excitation light is therefore not in issue in this endoscope configuration.

3.6 Fiber tip bead functionalization and micro-lenses objective

The first endoscope design we implemented integrates a silica bead functionalization of the fiber, with a micro-objective composed of 4 micro-lenses. Although the bead might not be the best suited for durability, this combination provides the best compromise between FoV and PSF.

The distal components of the endoscope are encased inside a 2 mm inner diameter tube, which then represents the theoretical limit of the scan performed by the fiber distal tip. In practice, we found that a maximal scan diameter of 1 mm avoids distortion on the image edges caused by aberrations of the fixed micro-objective and an increased PSF. For this reason, and because of the 0.63 magnification factor of the objective, the

---

[3] Short-circuits may happen if two or more weldings are in contact with the steel tube, and prevent from attaining a proper resonant excitation of the fiber.

maximal FoV achievable by this combination is about 600 µm.

3.6.1 Parasitic noise

Despite the benefits, we encountered two major issues when applying this endoscope design to nonlinear imaging. Both resulted in a parasitic signal that decreased the signal-to-noise ratio (SNR) or even overpass the desired signal.

Two photon fluorescence on the low polymer coating

When performing 2PEF imaging using this endoscope, we encountered a strong noise, present on all images regardless of the sample under study. To determine its origin, we recorded the signal collected in a typical endoscopy setup, represented in figure 3.17, without pointing the endoscope head to a sample. The endoscope head was placed inside a sealed carton box to prevent it from collecting ambient light. The laser source is an ytterbium doped master oscillator (Monaco, Coherent) pumping a broadband optical parametric oscillator (Opera-F, Coherent), tunable over the 640-940 nm and 1147-2676 nm ranges, and delivering 40-80 fs pulses with an energy of a few µJ, at a 1 MHz repetition rate. The excitation wavelength for the following results is fixed at $\lambda_{\text{exc}} = 920$ nm. A collection filter, 565±66 nm bandpass (BP), sets the collected signal to target common fluorophores like GFP (green fluorescent protein). Detection is performed by a photo-multiplier (PM, H7422-40, Hamamatsu) with a spectral response from 300 nm to 740 nm.

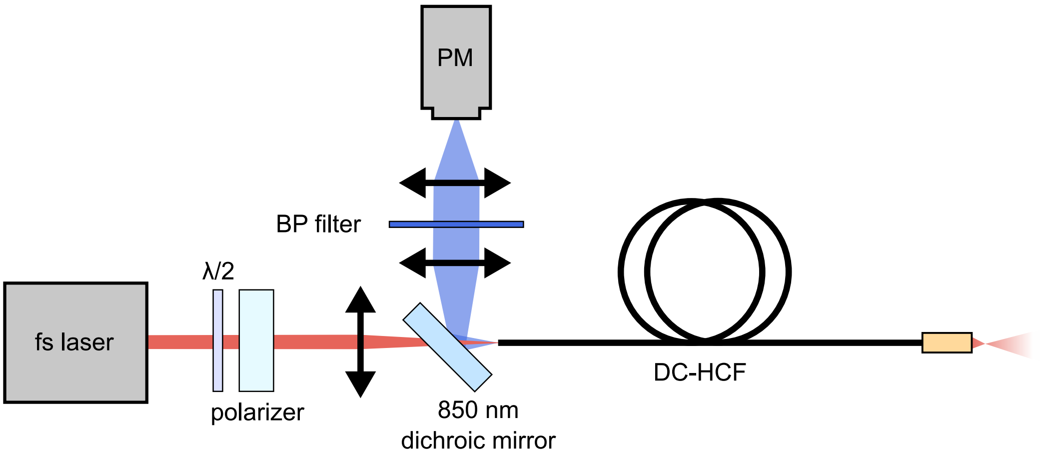

Figure 3.17: *Experimental setup to detect and identify the noise observed in 2PEF imaging. It corresponds to a typical endoscopy scheme deprived of any sample to probe.*

To identify the causing effect of this noise, we detected the signal with increasing excitation average power P_{in} (blue dots in figure 3.18 (a)), measured before injection

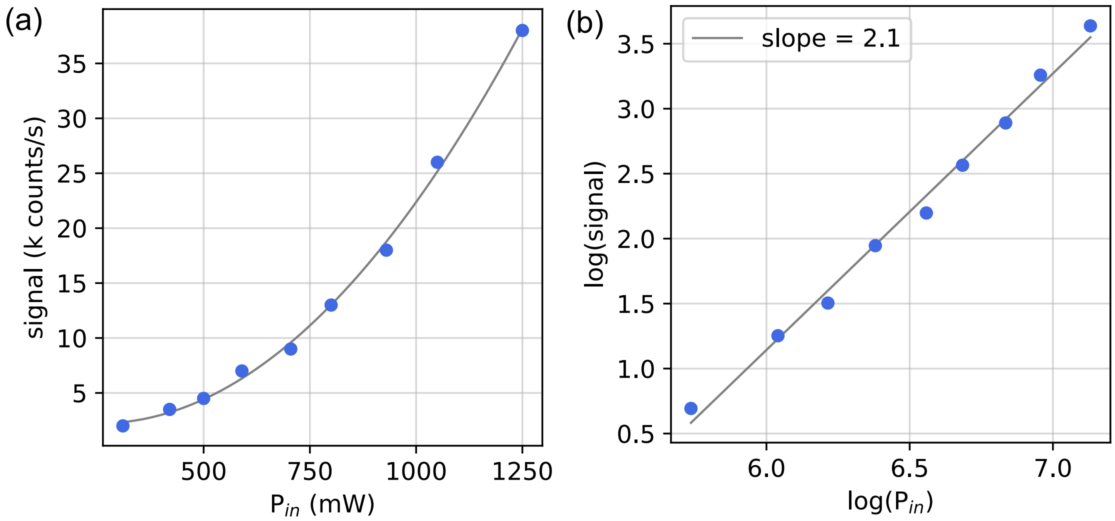

Figure 3.18: *(a) Linear and (b) log-log representation of the noise signal detected with respect to the excitation average power* P_{in}*, measured before injection into the fiber core.*

into the DC-HCF core. The maximal average power delivered by the laser at 920 nm is about 1250 mW. Any value below this maximum is obtained by adjusting a half-wave plate coupled with a polarizer, as depicted in figure 3.17. A quadratic fit is added to the measurements (gray solid line) and corresponds well with the experimental data. It is ensured by plotting the log-log evolution in figure 3.18 (b). The slope of the linear fit (2.1) confirms the quadratic dependence of the noise with respect to the excitation average power.

This quadratic evolution of the noise signal implies that it arises from a 2PEF or SHG effect generated by some element inside the endoscope. It is however unlikely that SHG would happen, considering the materials involved[4]. To confirm it, we measure the detected signal with respect to its wavelength in figure 3.19 (a). With a constant excitation signal at a average power $P_{\text{in}} = 1$ W, the BP filter mentioned above is successively replaced by 10 nm wide BP filters. The signal detected has a spectral emission located in the 500-600 nm range. It is higher than the wavelength of second harmonic (460 nm here) which leads to award this noise to a 2PEF effect.

In figure 3.19 (b), we measure the parasitic signal as a function of the excitation power for the DC-HCF (blue dots), then after the silica bead functionalization (red dots), and finally for the full endoscope (green dots), meaning for the fiber functionalized with a silica bead and with a micro-lenses objective. In all three instances, we obtain

---

[4] Because SHG can only happen in non-centrosymmetric media, as explained in chapter 1, which is not the case of amorphous glass.

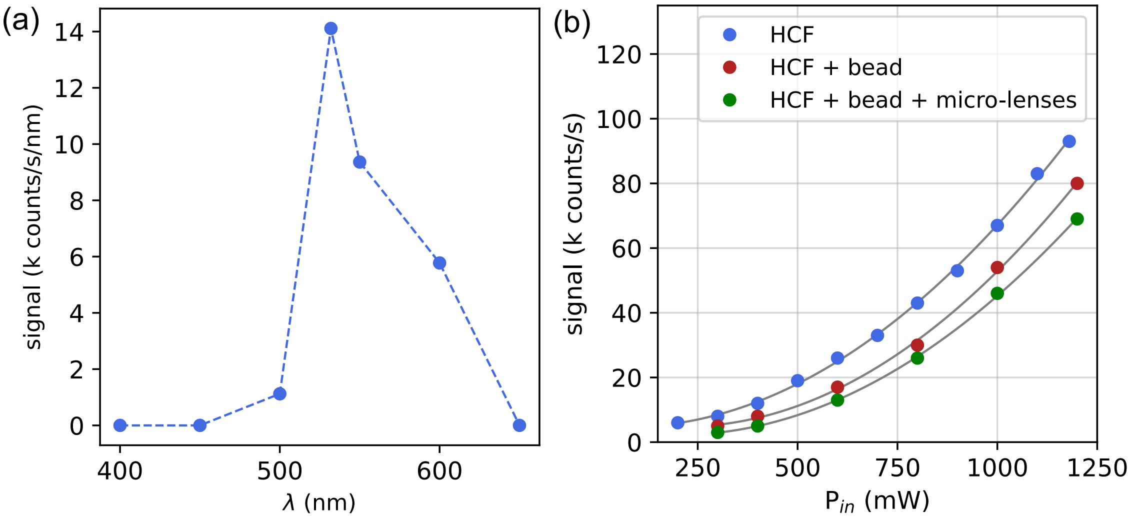

Figure 3.19: *(a) Noise signal detected as a function of the collected wavelength, fixed by 10 nm wide bandpass filters, for an excitation average power of* $P_{\mathrm{in}} = 1$ *W at* $\lambda_{\mathrm{exc}} = 920$ *nm. (b) Noise signal detected with respect to the excitation average power* P_{in} *for a propagation inside the HCF alone (blue dots), after the silica bead functionalization (red dots), and with the silica bead and the micro-lenses objective (green dots). The collection wavelength range is set by a 565±66 nm bandpass filter.*

a quadratic evolution with similar intensity. Consequently, the 2PEF noise must be generated inside the fiber itself and not in the distal optics added to the endoscope scheme.

Because the propagation inside the core is in air, we assume that the 2PEF noise must be triggered by a portion of light not coupled to the fiber core during injection. By imaging the near field at the output of the DC-HCF with a Si camera, we optimize the injection by maximizing the light coupled to the FM. For this we moved the proximal end of the DC-HCF in three directions with respect to the injection lens. We record the noise, then add a misalignment Δz in the z direction, which decreases the light coupled to the fiber core, and therefore increases the light coupled to the double clad. Figure 3.20 (a) shows a significant increase of the measured noise with the misalignment Δz, therefore with the light intensity inside the double clad.

The origin of the 2PEF noise thus lies indeed in the cladding materials, and our attention naturally draws towards the polymer cladding surrounding the inner silica cladding. To investigate its fluorescent response, we spread a thin layer of low index monomer (Desolight DF-0016) onto a microscope cover-slip then polymerize it. We afterwards place it vertically at the laser focal spot to replace the proximal tip of the fiber. Figure 3.20 (b) is the measured noise as a function of the excitation average power. The

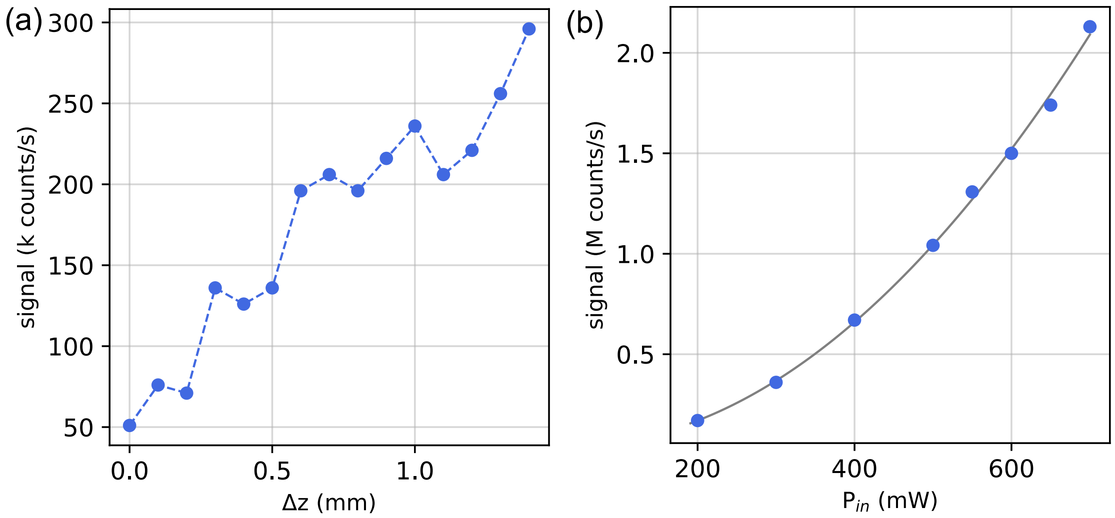

Figure 3.20: *(a) Measured dependence of the noise signal with the quality of injection into the fiber core, for an excitation average power of* $P_{\text{in}} = 1$ *W. The injection is optimized to maximize the transmission into the FM of the HCF, then a misalignment is added in the z direction* ($\Delta z > 0$) *resulting in less power guided in the DC-HCF core and more in the double clad. (b) Signal detected when replacing the fiber input by a thin layer of low index polymer at the focal spot of the laser. A monomer is spread on the surface of a microscope cover-slip then polymerized.*

signal is very high and has a quadratic profile. It confirms that the 2PEF noise observed previously is generated at the silica/polymer interface by light coupled to the inner cladding. Consequently, the injection into the hollow core must be carefully optimized and regularly adjusted in order to minimize this effect, as a small misalignment of the injection will lead to an imaging noise increasing with the average power of the excitation source.

Because a > 80% coupling ratio to the FM of the core is attained across the first transmission band of the fiber, this effect is expected to be very weak for low average power of the excitation source, as it should be the case for biological imaging. However, it forces to be mindful of the injection inside the fiber, as a slight misalignment could cause a sharp increase of the imaging noise.

Third harmonic generation inside the silica bead

The noise signal detailed above can be an issue in performing high contrast 2PEF and SHG images, but should not have any impact on 3PEF nor THG imaging because it would require three photon absorption to happen in the polymer layer, though the probability is far lower than two photon absorption. Nonetheless, we found that another affect restrains 3PEF and THG imaging in this endoscope arrangement. Indeed, only a very weak contrast was reached with these imaging techniques, which goes against the expectations (see chapter 1). Because a very high power density is reached when focusing the beam to a small spot with the silica bead, this low contrast could be caused by a third harmonic signal generated at the bead surface. Indeed, THG is produced for high power density at the interface between two dielectric media of different refractive indices, which matches the conditions at the silica/air interface on the output surface of the bead.

To investigate it, we measure, following the scheme in figure 3.21 (a), the spectrum at the output of the DC-HCF. Figure 3.21 (b) shows the results before (blue) and after (red) the bead insertion, for an input wavelength of 1300 nm.

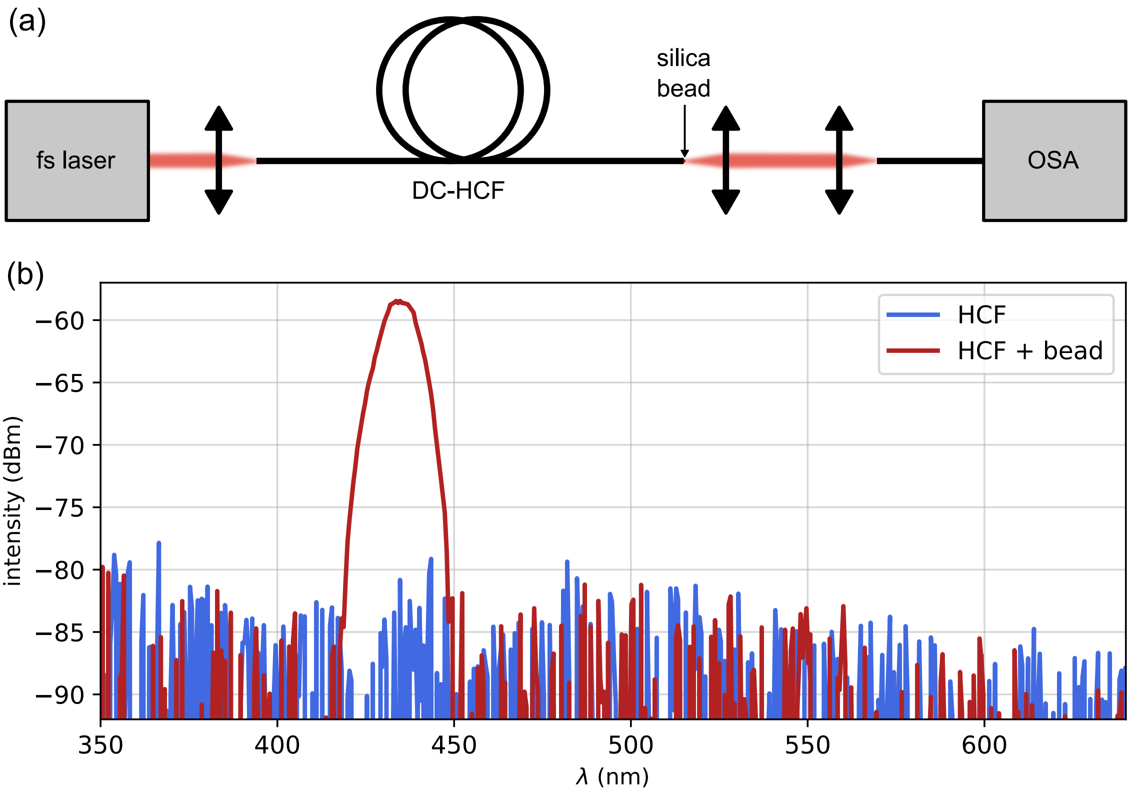

Figure 3.21: *(a) Schematic representation of the setup measuring the spectrum at the output of the DC-HCF functionalized with a silica bead, and (b) spectrum measured before (blue) and after (red) functionalization. Acquisitions were performed at* $\lambda_{\text{exc}} = 1300$ *nm and for a constant average power* $P_{\text{exc}} = 1.2$ *W.*

An intense peak, visible to the eye, around 433 nm is detected only with the bead inserted, confirming this parasitic signal arises from an interaction inside it. Moreover, the emission wavelength of this signal is exactly a third of the excitation wavelength, and corroborates the THG origin. Therefore, this signal is in the range of THG imaging signals, as their origin lies in the same effect, and raises the noise when performing such imaging. Additionally, this signal at 433 nm could cause linear fluorescence inside the sample, with an identical emission spectrum to 3PEF imaging but reduced spatial resolution, and increased ou-of-focus background. Conversely, it causes a decrease in imaging contrast for both THG and 3PEF imaging. 2PEF, SHG and CARS imaging, however, are not affected by this effect, which explains why endoscopes performing them with a bead functionalization of the fiber have been reported [19, 21].

3.7 Fiber tip GRIN functionalization and GRIN micro - objective

The GRIN lens functionalization, presented in section 3.1.2, is a good alternative to the silica bead. It produces a larger spot size which can be corrected by a GRIN fiber micro-objective, at the cost of a smaller FoV. If we consider again the maximal scan width of the fiber tip to be 1 mm, the magnification of the GRIN micro-objective only allows to reach a 200 µm FoV. It is less favorable than what the micro-lenses objective provides, but sufficient to perform biological imaging.

Regarding the 2PEF noise from the low index polymer layer, detected in the previous design, it remains unchanged because the fiber itself is the same. However, it avoids power losses caused by clipping inside the endoscope head and results in a lower average power needed at the input of the fiber, which in term reduces the impact of this noise if any misalignment of the injection is present.

3.7.1 Third harmonic generation noise reduction

Because the major issue of the endoscope scheme presented previously is a significant THG noise that restrains the contrast of 3PEF and THG imaging, we perform the same spectrum measurements, following the setup shown in figure 3.22 (a), with a GRIN lens spliced to the distal tip of the DC-HCF.

The measured spectrum, depicted in figure 3.22 (b) shows again a high THG peak, comparable to results obtained for the silica bead functionalization, for a GRIN fiber length of $L_{\mathrm{GRIN}} = 235$ µm (blue), which provides the highest spot size reduction (see section 3.1.2). It was actually predictable because in this case the focalization happens exactly on the output surface of the GRIN fiber, as in figure 3.6 (a). It results again in a high power density at the interface between silica (GRIN fiber core) and air, favoring THG.

Although, with this technology, we have seen that reducing the GRIN fiber length

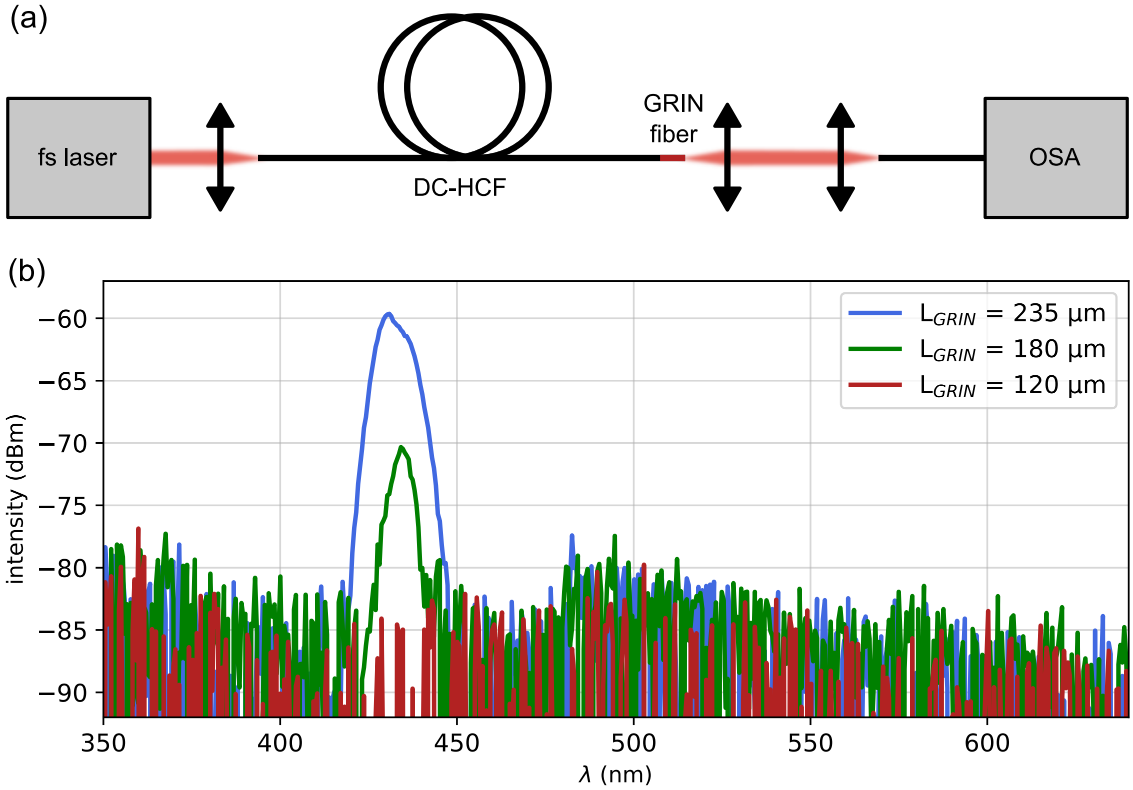

Figure 3.22: *(a) Schematic representation of the setup measuring the spectrum at the output of the DC-HCF functionalized with a GRIN lens, and (b) spectrum measured for* $L_{\mathrm{GRIN}} = 235\ \mu m$ *(blue),* $L_{\mathrm{GRIN}} = 180\ \mu m$ *(green), and* $L_{\mathrm{GRIN}} = 120\ \mu m$ *(red). Acquisitions were performed at* $\lambda_{\mathrm{exc}} = 1300\ nm$ *and for a constant average power* $P_{\mathrm{exc}} = 1.06\ W$*.*

L_{GRIN} moves the focal spot position away from this interface, and therefore reduces the power density on the fiber endface. The green curve in figure 3.22 (b) shows a great reduction of the THG peak intensity for $L_{\mathrm{GRIN}} = 180\ \mu\mathrm{m}$, and it decreases further to below the OSA noise threshold for $L_{\mathrm{GRIN}} = 120\ \mu\mathrm{m}$ (red curve). We conclude from these measurements that a GRIN lens functionalization with $L_{\mathrm{GRIN}} = 120\ \mu\mathrm{m}$ should be enough to highly reduce, if not suppress completely, the third harmonic signal hampering 3PEF and THG imaging.

3.8 Imaging comparison

The improvements provided by a GRIN functionalization are further accentuated by comparisons of 2PEF and 3PEF imaging. The endoscopic setup is similar to the one presented in figure 3.17 and will be presented in detail in the next chapter. The laser source is an ytterbium doped master oscillator (Monaco, Coherent) pumping a broadband optical parametric oscillator (Opera-F, Coherent), delivering 40-80 fs pulses with an energy of a few µJ, at a 1 MHz repetition rate. The excitation wavelength for the following results is fixed at $\lambda_{\text{exc}} = 920$ nm for 2PEF and $\lambda_{\text{exc}} = 1300$ nm for 3PEF. For both, a 565±66 nm BP filter precedes the PM to ensure only the fluorescence signal is detected.

First, figure 3.23 depicts 2PEF images of 2 µm in diameter fluorescent beads (a, c) and neurons inside a mouse brain (b, d) marked with GFP[5]. Both endoscope schemes are able to produce 2PEF images, including on biological tissue. However, it is clear from figure 3.23 that images obtained with the GRIN functionalization (c, d) grant a better contrast. In fact, the noise background previously awarded to 2PEF from the low index polymer layer around the silica inner cladding is distinctly observed on images recorded with the bead functionalization (a, b) and impairs the overall image quality. Because this issue is due to the quality of injection into the hollow core, it should be limiting for both functionalization methods. Yet, because a higher excitation average power is needed with the bead functionalization to compensate for the clipping inside the endoscope head, it remains primarily an issue in that case.

Furthermore, a 3PEF imaging comparison of the same 2 µm fluorescent beads is illustrated in figure 3.24 (a, b). The image obtained with the GRIN functionalization (b), free of THG noise background, shows a drastic improvement in signal-to-noise ratio (SNR) over the one obtained with the bead functionalization (a). It is highlighted by a plot along the dashed blue lines (c). Figure 3.24 (b) exhibits a better definition of the fluorescent beads contour and almost no noise background, where it is almost half of the maximal detected signal in figure 3.24 (a).

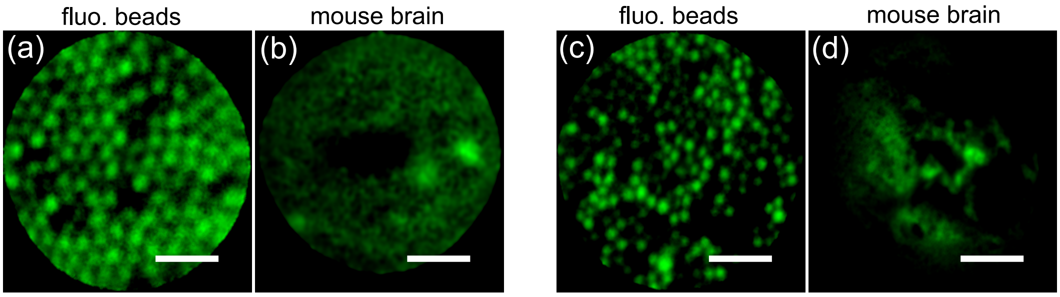

Figure 3.23: *2PEF imaging comparison of the endoscope based on a (a, b) bead or (c, d) GRIN functionalization. Scale bars are respectively: (a) 10 µm, (b) 25 µm, (c) 20 µm and (d) 40 µm. Excitation average power on the samples are respectively: (a) 18 mW, (b) 34 mW, (c) 10 mW and (d) 28 mW. Images are recorded with a 2 FPS acquisition rate and averaged over 5 images.*

---

[5] A full description of the sample preparation is provided in chapter 4.

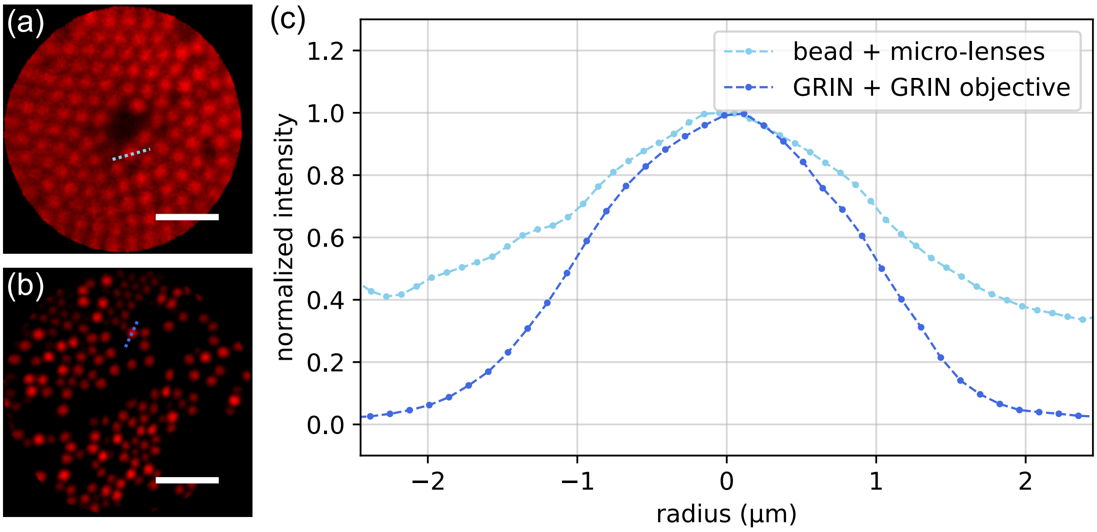

Figure 3.24: *3PEF imaging comparison of fluorescent beads with the endoscope based on a (a) bead or (b) GRIN functionalization. Scale bars are respectively: (a) 10 µm and (b) 20 µm. Excitation average power on the samples are respectively: (a) 26 mW and (b) 11 mW. Images are recorded with a 2 FPS acquisition rate and averaged over (a) 20 and (b) 5 images. (c) Plot along the dashed lines in (a, light blue) and (b, dark blue).*

Additionally, figure 3.24 (a) is the only 3PEF image captured with this endoscope scheme as it needed a high average power on the sample (25 mW) and an averaging along 20 images, causing some photo-bleaching over time at the center of the image. This is a common issue with this type of scanning mechanism, as will be discussed in the following chapter, and denotes the limitation for achievable images. 3PEF imaging on biological tissues is thus hardly conceivable with this endoscope scheme, which is a major issue in the context of this work. Consequently, subsequent results will focus only on the endoscope scheme combining a GRIN functionalization and a GRIN micro-endoscope.

It is noteworthy that the bead functionalization is still a viable method for certain use cases, notwithstanding these issues, particularly for large FoV imaging. Likewise, the GRIN functionalization can be combined with a micro-lenses objective if a compromise on the resolution can be made, even though it will not be investigated further here.

Conclusion

A multimodal nonlinear endoscope is assembled, based on a double clad hollow core fiber functionalized at its distal tip to produce an output spot small enough to perform high resolution imaging. A fixed micro-objective enables to further reduce this spot size as well as shifting its position, increasing the working distance to either 600 µm with a micro-lens based objective, or 300 µm for a GRIN fiber based objective. Scanning is performed by a doubly resonant piezoelectric tube that produces an expanding spiral pattern. The GRIN lens fiber functionalization, although it grants a larger spot size, which ultimately leads to smaller FoV when coupled to the GRIN objective, avoids parasitic THG noise generation inside the silica bead when trying to perform 3PEF or THG imaging. It also corrects the clipping issue caused by the high NA at the output of this bead functionalization, which forces to raise the excitation power, leading to a 2PEF noise generation at the cladding / low index polymer interface. In term, it raises the imaging noise when applying 2PEF or SHG modalities. Imaging comparison, using 2PEF and 3PEF, of both designs shows a massive increase of contrast and overall image quality when using the GRIN fiber functionalization.

Chapter 4

Nonlinear endoscopic imaging

The main attribute of the present endoscope is the multimodality. We give a particular attention to the integration of 3PEF and THG imaging modalities to 2PEF, SHG and CARS techniques, already demonstrated in similar devices [15, 19, 21, 55, 64, 112]. 3PEF and THG modalities benefit from an improved spatial resolution and SNR, thanks to a higher excitation localization [26], and allow imaging for depth into tissues in the millimeter range [10, 12], unreachable by 2PEF and SHG [27–32] because of the adequacy of its excitation wavelength for propagation in biological tissues [6].

However, the generation of 3PEF and THG effects requires higher peak power than 2PEF and SHG which causes issues when transferring these techniques from NLOM to micro-endoscopy (see chapter 1). First reports consisted of fiber-based sources with bulk distal optics [6, 28, 32, 113], though it did not provide a truly flexible and miniature endoscope. With the generation of solitons directly inside the endoscopic solid core fiber, Akhoundi *et al.* [52] obtained a flexible and miniature probe capable of 3PEF and THG, but restrained to a single excitation wavelength, thus not suitable for multimodal imaging. Recently, a 3PEF endo-microscope was realized for *in-vivo* imaging deep inside a mouse brain using a hollow core fiber [31], but again with a relatively bulky head (> 1 cm in diameter).

In this chapter, we present the experimental setup implemented to perform multimodal nonlinear endoscopic imaging. Characterization of the endoscope design fabricated is provided through spatial and axial resolution measurement and comparison between 2PEF and 3PEF imaging on various samples. A study of the different acquisition parameters, in particular the acquisition rate and averaging, and their impact on the image quality is then outlined. Afterward, a thorough description of all samples studied in this work and a demonstration of imaging capability of the endoscope is detailed, covering 2PEF, SHG, 3PEF and THG imaging on unlabeled biological tissues at different depths bellow the sample surface. A separate section is dedicated to CARS imaging. It presents the experimental setup with spatial and temporal alignment considerations for the two excitation beams, as well as an imaging demonstration on unlabeled biological tissues. Finally, the photo-bleaching limitation, inherent of the piezo tube scanning mechanism, is discussed and future perspectives are outlined to improve the endoscope design and setup.

4.1 Multiphoton imaging

We first turn our attention to multiphoton imaging, *i.e.* based on either 2PEF, SHG, 3PEF or THG. A single excitation source is needed and the target effect is chosen by adjusting the spectral range of the detection channel. CARS imaging, for which two excitation beams are required, will be described separately with different considerations.

4.1.1 Setup and excitation laser properties

The experimental endoscopy setup for multiphoton imaging is represented in figure 4.1. The excitation source is composed of an ytterbium doped master oscillator (Monaco, Coherent) pumping a broadband optical parametric oscillator (Opera-F, Coherent), tunable over the 640-940 nm and 1147-2676 nm ranges. It delivers 40-80 fs pulses (depending on the wavelength) with an energy of a few µJ, at a 1 MHz repetition rate. Excitation pulses are injected inside the hollow core of a 2 m long DC-HCF with a lens of 40 mm focal length to excite the sample and generate nonlinear imaging effects at the distal end of the endoscope. The quality of injection, in the FM, is ensured by imaging the near field at the output of the endoscope with either a Si (DCC1645C, Thorlabs) or InGaAs (SU320KTS-1.7RT, SUI) camera. It avoids spurious light propagation inside the fiber double clad and maximizes the coupling to the core FM. A minimum coupling efficiency of 80 % at 920 nm, 1300 nm and 1700 nm is measured through this 2 m long endoscope.

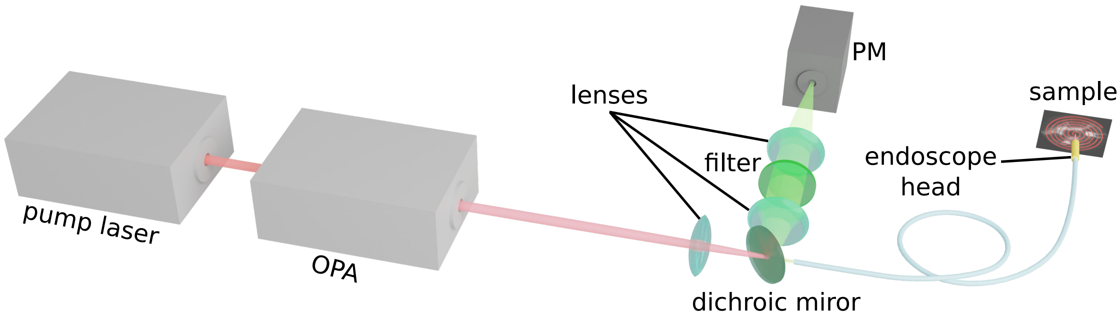

Figure 4.1: *Schematic representation of the experimental setup implemented to perform endoscopic multiphoton imaging.*

The collected signal is back-propagated by the fiber double clad, then separated from the excitation by an 850 nm dichroic mirror. A bandpass filter is placed before the photo-multiplier (PM, H7422-40, Hamamatsu) to select the detection wavelength and thus the nonlinear effect to visualize. Because of the difference in NA of the core and double clad of the fiber (respectively 0.024-0.034 and 0.38, as seen in chapter 2), different lenses have to be employed for injection into the core and collection from the double clad. Therefore, the dichroic mirror is placed between the fiber proximal tip and the injection/collection lenses, which complicates the alignment and forces the use of lenses with sufficiently long focal lengths. A half-wave plate coupled with a polarizer (not shown in figure 4.1) are placed before the injection into the fiber to control the excitation average power. The endoscope is either moved freely in the hand of the operator, or fixed on a 3D-moving stage in front of the sample under study. When the sample is removed, the output of the endoscope can be imaged to control the injection into the fiber core, sent to a PSD to calibrate the scanning mechanism, or to a powermeter to measure the excitation average power immediately after an image acquisition. All images are acquired with the highest possible excitation average power, producing the highest contrast, without inducing photobleaching or damage to the sample.

4.1.2 Two and three photon fluorescence imaging comparison

The aim of this work is primarily to integrate 3PEF and THG imaging techniques into a highly multimodal endoscope that already performs 2PEF and SHG imaging. While THG allows imaging different structures, 3PEF imaging targets are identical to

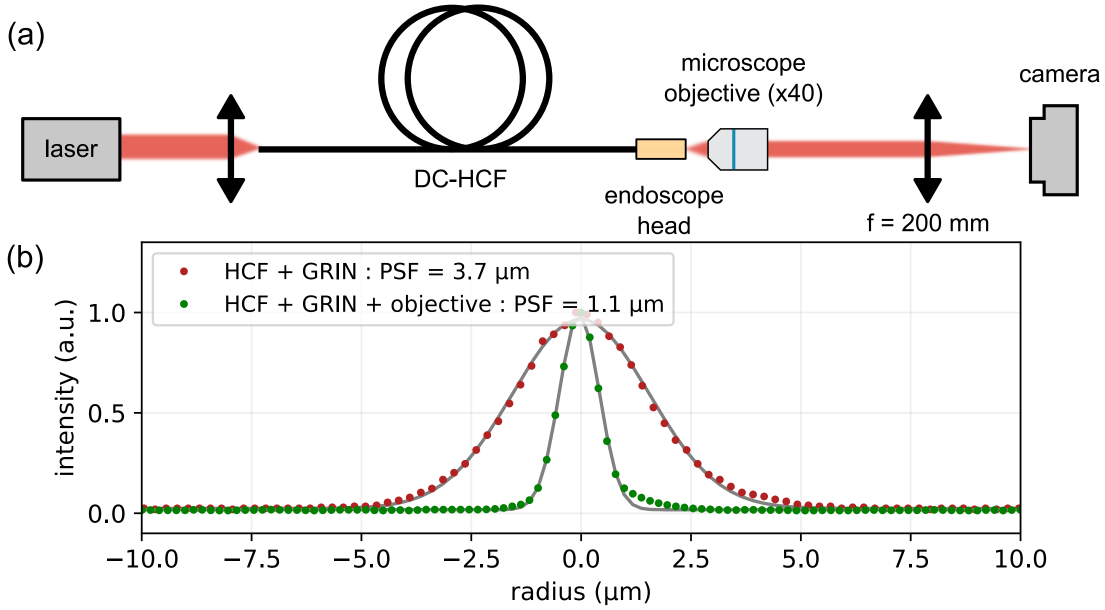

Figure 4.2: *(a) Experimental setup to measure the PSF of the endoscope. (b) Data points and Gaussian fit (gray line) of the PSF at the output of the functionalized fiber (red) and full endoscope (green), for a wavelength of* $\lambda = 920$ *nm.*

2PEF. However, this section highlights the advantages provided by 3PEF imaging, in particular a higher spatial resolution, SNR and optical sectioning. It is also possible to image deeper inside tissues than with 2PEF [32], although it is not demonstrated here, due to the limited working distance of the present micro-objective.

Spatial resolution

The spatial resolution of images acquired with the endoscope is tied to the PSF at its output. In fact, for a proper sampling, the PSF represents the smallest distinguishable spot, and therefore clamps the spatial resolution. Accordingly, we measure the PSF with a calibrated setup presented in figure 4.2 (a). The spot is imaged onto a Si camera (DCC1645C, Thorlabs) with a x40 microscope objective (Olympus) coupled with a tube lens of 200 mm focal length. The spot profile is depicted in figure 4.2 (b) for the fiber with GRIN functionalization (red dots) and with the addition of a GRIN micro-objective (green dots). A Gaussian fit (gray solid line) supplies the PSF measurement (FWHM).

As it was mentioned in chapter 3, the PSF measured after functionalization of the DC-HCF with a GRIN fiber of L_{GRIN} = 120 µm length is 3.7 µm. With the addition of the GRIN micro-objective, the PSF value drops down to 1.1 µm. The decrease is notable, and this PSF at the output of the endoscope is small enough to provide high resolution

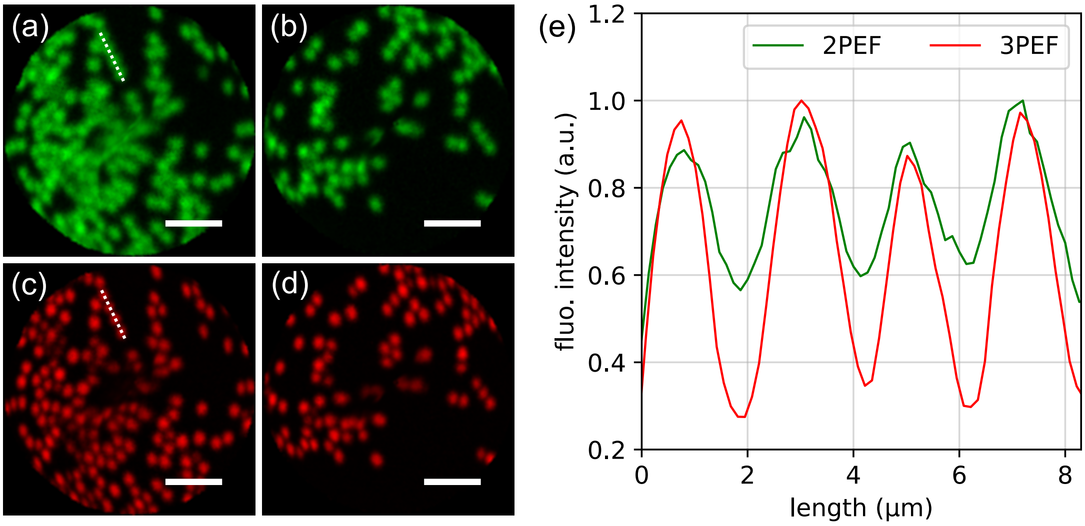

Figure 4.3: *(a, c) and (b, d): 2PEF ($\lambda_{\mathrm{exc}} = 920$ nm, in green on all subfigures) and 3PEF ($\lambda_{\mathrm{exc}} = 1300$ nm, in red on all subfigures) imaging comparison of 2 µm fluorescent beads at two different positions on the sample. Scale bars are 10 µm, and excitation average power on the sample is 10 mW for 2PEF and 12 mW for 3PEF. Images are recorded with a 2 FPS acquisition rate and averaged over 5 images.*

images on biological samples. Still, when taking the 0.22 magnification factor of the objective into account, a 0.8 µm PSF is expected but not reached in practice. It can be explained by considering the focal spot after the GRIN lens. The measured NA is about 0.11, which is significantly less than the 0.16 NA on this side of the micro-objective. Consequently, the GRIN micro-objective pupil on the proximal side is not filled, hence the 0.7 NA on the distal side is not reached either, which leads to a spot size larger than expected.

Figure 4.3 shows that this spot size is enough to resolve fluorescent beads with a 2 µm diameter. As an example, two different positions on the sample, (a, c) and (b, d), are imaged with 2PEF (green) and 3PEF (red). Excitation wavelengths are 920 nm and 1300 nm respectively, and the detection filter is a 565±66 nm bandpass (BP). Even though both techniques allow seeing individual beads, 3PEF provides a better definition of the contours and renders the beads more distinguishable, especially when clustered together.

To emphasize on this, a plot along the white dashed lines in figure 4.3 (a) and (c) is presented in figure 4.3 (e). It confirms that 3PEF allows to outline the shape of the beads more precisely. It also discloses a considerable increase in signal-to-noise ratio (SNR) that can be explained by an improvement in optical sectioning, as we shall see below.

Additionally, this enhancement in overall image quality is underlined by a compar-

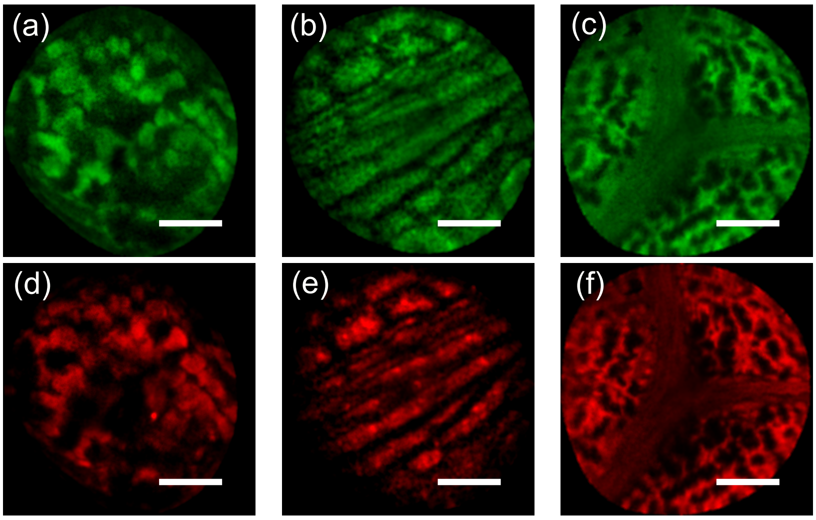

Figure 4.4: *2PEF ($\lambda_{\text{exc}} = 920$ nm, in green on all subfigures) and 3PEF ($\lambda_{\text{exc}} = 1300$ nm, in red on all subfigures) imaging comparison of oak leaves. Scale bars are (a, d) 40 µm and (b, c, e, f) 50 µm, and excitation average power on the sample is 16 mW for 2PEF and 20 mW for 3PEF. Images are recorded with a 2 FPS acquisition rate and averaged over 5 images.*

ison of 2PEF and 3PEF images of oak leaves in figure 4.4. Again the cells contour is sharper with 3PEF and the contrast is much better because of the increased SNR.

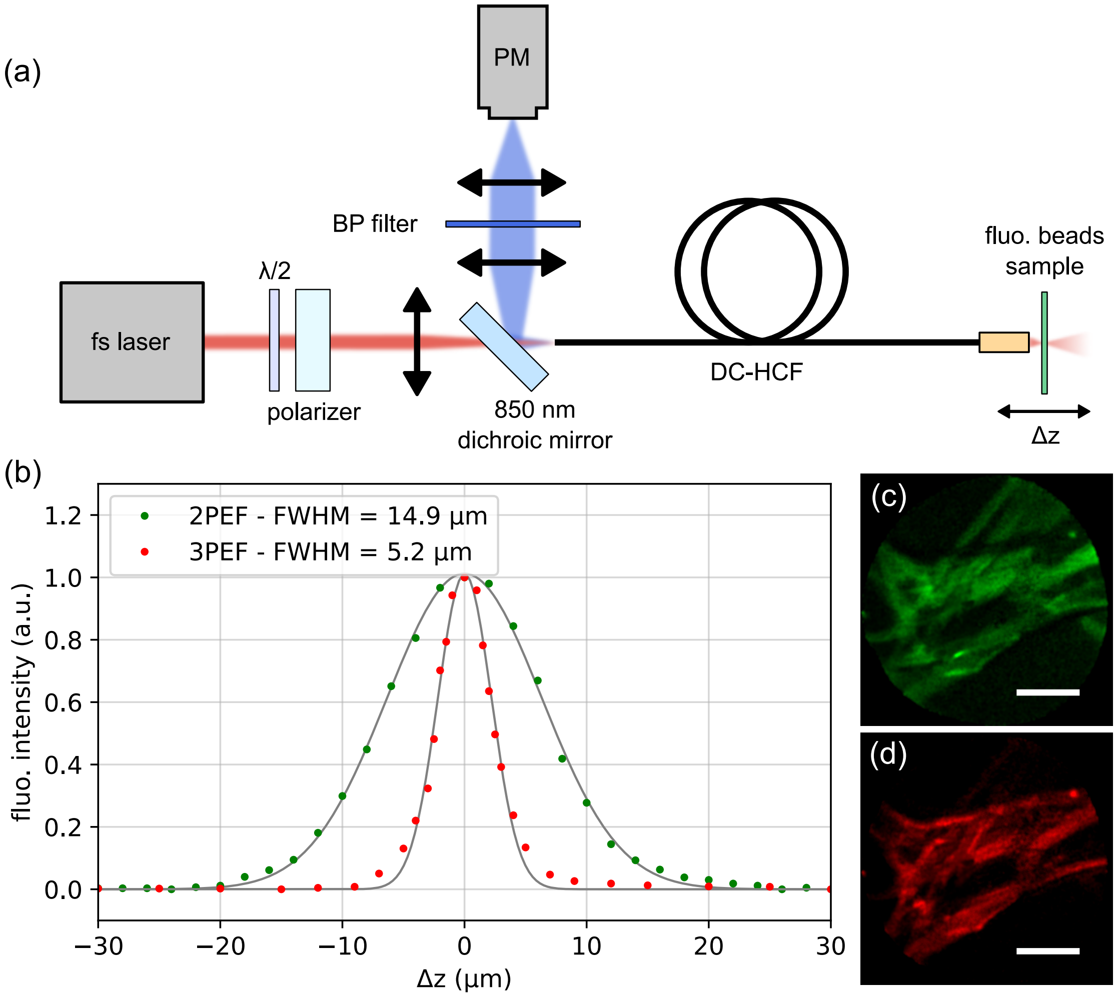

Figure 4.5: *(a) Axial resolution measurement setup by recording the 2PEF ($\lambda_{\text{exc}} = 920$ nm, in green on all subfigures) and 3PEF ($\lambda_{\text{exc}} = 1300$ nm, in red on all subfigures) signals on a single fluorescent bead and moving the endoscope in the z direction. (b) Data points and Gaussian fit (gray line) of the endoscope axial resolution. (c) 2PEF and (d) 3PEF imaging comparison on optical cleaning paper. Scale bars are 50 µm, and excitation average power on the sample is 15 mW for 2PEF and 14 mW for 3PEF. Images are recorded with a 2 FPS acquisition rate and averaged over 5 images.*

Axial resolution

To characterize the optical sectioning of the endoscope, we measure the axial resolution of 2PEF and 3PEF imaging. For that, we used the experimental setup exhibited in figure 4.5 (a), similar to the imaging setup described above, with a sample moving along the z direction. The endoscope is placed to excite fluorescence on a single 2 µm bead, and the signal is measured when adding a displacement Δz. Results are plotted in figure 4.5 (b), and a Gaussian fit (gray solid line) allows to extract the axial resolution, here defined as the FWHM.

The measured axial resolution is 14.9 µm for 2PEF, and drops down to 5.2 µm for 3PEF. It is a substantial improvement in optical sectioning that explains the SNR increase denoted above. It is also particularly visible on certain images where out-of-focus structures are apparent. For instance, figures 4.5 (c) and (d) show 2PEF and 3PEF images of optical cleaning paper. Some tissue fibers out of the focus plane, especially at the top of the images, emit a 2PEF signal and are therefore imaged in figure 4.5 (c) whereas they are completely absent of the 3PEF image (figure 4.5 (d)).

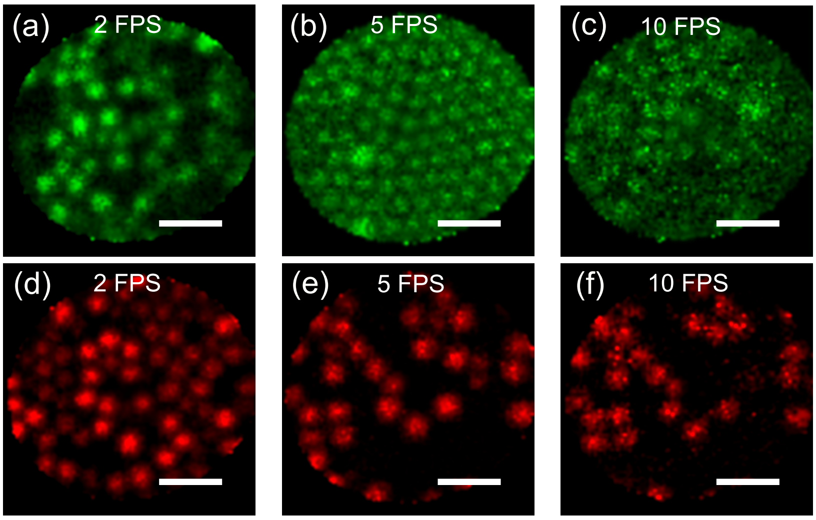

Figure 4.6: *2PEF ($\lambda_{\text{exc}} = 920$ nm, in green on all subfigures) and 3PEF ($\lambda_{\text{exc}} = 1300$ nm, in red on all subfigures) imaging comparison of 2 µm fluorescent beads, for acquisition rate of: (a, d) 2 FPS, (b, e) 5 FPS and (c, f) 10 FPS. Scale bars are 10 µm, and excitation average power on the sample is 16 mW for 2PEF and 18 mW for 3PEF. Images are single shot acquisition (i.e. no averaging is performed).*

4.1.3 Acquisition rate and image averaging

To accommodate the image acquisition to specific requirements, three parameters are tunable. The FoV is adjusted by the driving voltage applied to the piezoelectric tube, and limited by the size of the endoscope head and the magnification ratio of the objective. The acquisition rate is fixed by the duration set for each step of a scanning cycle, *i.e.* scan, break and rest phases. In practice, essentially the scan duration will affect it, as it represents most of the cycle duration, and both brake and rest phases are chosen to be as short as possible. The acquisition rate is capped by the sampling and PSF, because the distance between two consecutive circles of the spiral scan must be as small as the PSF and the pixel size, as detailed in chapter 3.

Another limiting effect is the signal collection. The signal generated is constant over time, though the amount of it that is collected to render an image depends on the acquisition duration. Thus, a higher acquisition rate leads to a decrease in SNR. In this scope, we compare in figure 4.6 2PEF and 3PEF single shot images of 2 µm fluorescent beads acquired at (a, d) 2 FPS, (b, e) 5 FPS and (c, f) 10 fps. At 2 FPS, both techniques allow a good image quality, with a slight SNR advantage for 3PEF. The SNR clearly drops down for the 2PEF image at 5 FPS (figure 4.6 (b)) whereas 3PEF still provides a good contrast with low background noise (figure 4.6 (e)). At 10 FPS, the 3PEF image (figure 4.6 (f)) quality is distinctly impacted, but individual beads are still identifiable, and the background noise is fairly low. On the other hand, individual beads are hardly distinguishable with 2PEF (figure 4.6 (c)) as the noise gets closer to the fluorescent signal detected.

It points out yet another advantage of using 3PEF imaging, deriving from the SNR improvement, especially for investigation of dynamical activities inside biological tissues.

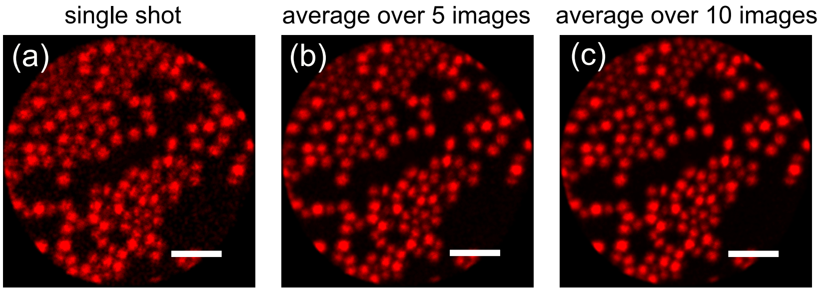

Figure 4.7: *Comparison of image averaging for 3PEF ($\lambda_{\text{exc}} = 1300$ nm) images of 2 µm fluorescent beads. Images are either (a) single shot acquisition, or averaged over (b) 5 or (c) 10 images. Scale bar is 10 µm, excitation average power on the sample is 12 mW, and acquisition rate is 2 FPS.*

The last acquisition parameter is the image averaging. Ideally, single shot acquisitions should be preferred because it allows real-time observation of active processes. Yet, image averaging increases the contrast and can bring out weakly emitting structures, otherwise hidden under the noise level. To grasp this effect, figure 4.7 shows a 3PEF imaging comparison on 2 µm fluorescent beads. Averaging over 5 frames (b) notably decreases the noise and leads to a better defined beads contour than the single shot acquisition (a). The 10 images average (c), however, only faintly improves the image quality.

For these reasons, an averaging over 5 frames is applied to most images rendered here, for presentation purposes, but real-time imaging without any averaging is still feasible with acceptable image quality and SNR.

4.1.4 Biological samples preparation

Various samples were used in this work, and each was prepared separately. Concerning the samples exploited above, oak leaves and optical cleaning paper were simply pressed between a microscope slide and a 120 µm thick cover-slip, and both have a thickness of about 300 µm. The fluorescent 2 µm beads were diluted inside water, spread and dried onto a microscope slide with a cover-slide as well. A single layer of beads is produced on most of the sample surface, although some clusters are also formed.

Regarding the biological samples, the only one labeled for fluorescence imaging is the mouse brain[1]. It is extracted from a transgenic mouse, for the purpose of amplifying the fluorescence emission with green fluorescent protein (GFP). To demonstrate the label-free capacities of the endoscope, no other sample is labeled.

All mouse samples were fixed with paraformaldehyde (PFA) following common histology procedures, before being sliced at various thickness and placed on a microscope slide. A cover-slip is then added to mouse brain and retina samples, whereas skin and liver samples were left uncovered to increase the achievable imaging depth. The mouse tissue slices have a thickness of about 300 µm for the skin, 200 µm for the brain and liver, and 50 µm for the retina.

Fresh human colon biopsies[2] are set in water between a microscope slide and a cover-slip, set apart by a 1 mm spacer. The fresh ox liver sample is about 5 cm thick, and placed on a microscope slide without any cover, to allow the endoscope to be sunk into the tissue.

---

[1] Mouse brain slices are coming from the Institut des Neurosciences de la Méditerranée following INMED agreement number B13-055-19 and OGM agreement number 5817.

[2] Colon tissue samples are coming from the Biobank of the Assistance Publique des hôpitaux de Marseille (AP-HM), Marseille, FRANCE. The AP-HM biobank is open to research projects and administrated by an executive and ethic committee.

To summarize, all samples specifications are concentrated in the following table:

sample	thickness	fixed	labeled	cover-slip
2 µm beads	2 µm	no	yes (GFP)	yes
oak leaves	≈ 300 µm	no	no	yes
optics paper	≈ 300 µm	no	no	yes
mouse skin	≈ 300 µm	yes	no	no
mouse brain	200 µm	yes	yes (GFP)	yes
mouse retina	50 µm	yes	no	yes
mouse liver	200 µm	yes	no	no
human colon	≈ 1 mm	no	no	no
ox liver	≈ 5 cm	no	no	no

The reported studies have been conducted following the EU ethical rules on animals and humans.

4.1.5 Multimodal imaging

A set of multiphoton images captured on biological tissues is presented in figure 4.8. It demonstrates the ability of the endoscope to image various structures in different types of tissues, covering all four imaging techniques described before, namely 2PEF, SHG, 3PEF and THG. An optical filter wheel is placed in front of the PM to select the nonlinear effect to target, allowing to quickly switch the imaging effect during an acquisition session. Filters used in this work are: a 565±66 nm BP for 2PEF at λ_{exc} = 920 nm and 3PEF at λ_{exc} = 1300 nm, a 447±60 nm BP for SHG and THG at the same wavelengths, a 630±46 nm BP for 3PEF and a 562±20 nm BP for THG at λ_{exc} = 1700 nm.

First of all, the upper dermis layer of unstained mouse skin is successively imaged using SHG at λ_{exc} = 920 nm (figure 4.8 (a)), 3PEF and THG at λ_{exc} = 1300 nm (figures 4.8 (b) and (c) respectively), at the same position on the sample. The strong SHG signal shows the collagen fibrils organization, surrounding cells are outlined by THG, and 3PEF shows autofluorescence from proteins inside the tissue. Figure 4.8 (d) is a composite image, *i.e.* a stack of the three images presented above. The use of false colors (yellow for SHG, red for 3PEF and blue for THG) allows to underline the convenience of multimodal imaging to identify the different structures inside a tissue and their organization with

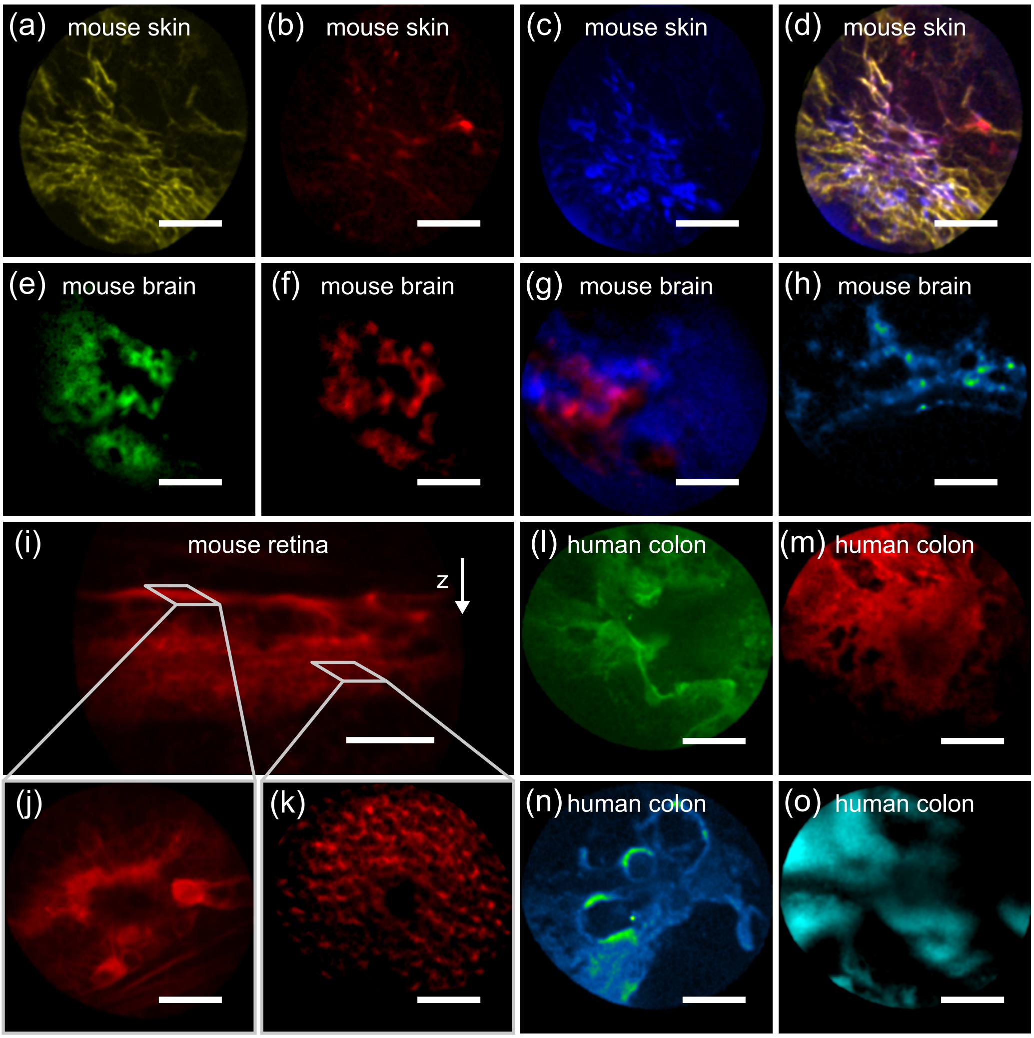

Figure 4.8: *(a) SHG ($\lambda_{\text{exc}} = 920$ nm), (b) 3PEF ($\lambda_{\text{exc}} = 1300$ nm) and (c) THG ($\lambda_{\text{exc}} = 1300$ nm) images of a mouse skin. (d) is a composite image of (a), (b) and (c). Mouse brain images using (e) 2PEF ($\lambda_{\text{exc}} = 920$ nm), (f) 3PEF ($\lambda_{\text{exc}} = 1300$ nm), (g) 3PEF (red) and THG (blue) combination ($\lambda_{\text{exc}} = 1300$ nm), and (h) 3PEF ($\lambda_{\text{exc}} = 1700$ nm). 3PEF images of a mouse retina: radial (i) and transverse section in the (j) ganglion cell layer (GCL) and (k) inner plexiform layer (IPL). Human colon images using (l) 2PEF ($\lambda_{\text{exc}} = 920$ nm), 3PEF at (m) $\lambda_{\text{exc}} = 1300$ nm and (n) $\lambda_{\text{exc}} = 1700$ nm, and (o) THG ($\lambda_{\text{exc}} = 1700$ nm). Scale bars are 40 µm for (e, f, g) and 50 µm for all other subfigures. Images are recorded with a 2 FPS acquisition rate and averaged over 5 images.*

one another. Because only one PM is used to collect the nonlinear signals in our setup, images must be acquired one after the other, with a change of collection filter and/or excitation wavelength between each. However, they could be recorded simultaneously with multiple PM by cascading dichroic mirrors of appropriate cut-off wavelength in the detection channel.

Because 3PEF has recently gained attention in neurology [28–32], an endoscope integrating this modality would be an ideal tool to investigate neurons *in-vivo*. In this scope, we produce 2PEF at λ_{exc} = 920 nm and 3PEF at λ_{exc} = 1300 nm images at a 100 µm depth inside a transgenic mouse brain slice in figures 4.8 (e) and (f) respectively. Intense fluorescence signals identify individual neurons, separated from the lower background signal of surrounding environment. Figure 4.8 (g) demonstrate again the ability to separate the 3PEF signal from neurons (red) from the THG generated by other histological structures, with the same excitation wavelength λ_{exc} = 1300 nm. Finally, neurons and some interconnections can also be imaged with a different excitation wavelength, for instance λ_{exc} = 1700 nm as shown in figure 4.8 (h).

In addition, we perform label-free 3PEF imaging of a radial section showing the different layers in a mouse retina [114, 115] at λ_{exc} = 1300 nm in figure 4.8 (i). The strongest autofluorescence emission hails from the ganglion cell layer (GCL) and enables a great contrast, with a broad range of signals from weak to bright fluorescent cells, as evidenced by the transverse section shown in figure 4.8 (j), displaying cells of various sizes. Although it emits a lower fluorescence signal, the inner plexiform layer (IPL) allows singling out individual cones, exhibited in the transverse section in figure 4.8 (k). Between these two, the inner nuclear layer (INL) emits the weakest signal, and is then not depicted here.

Lastly, two and three photon autofluorescence images, at λ_{exc} = 920 nm and λ_{exc} = 1300 nm respectively, of a fresh human colon biopsy are produced in figures 4.8 (l) and (m). Images of 3PEF and THG at λ_{exc} = 1700 nm are displayed as well in figures 4.8 (n) and (o). These images, acquired at depths of (l) 90 µm, (m) 115 µm, (n) 60 µm and (o) 85 µm below the sample surface, confer information on the tissue organization, even though individual cells are not distinguishable.

Because of the optical sectioning provided by multiphoton imaging, structures inside a tissue can be mapped with respect to the depth to recreate the 3D organization of the sample. This is illustrated in figure 4.9 by the stacked images presented as a function of the imaging depth. Figure 4.9 (a) depicts 2PEF images of unlabeled mouse liver at λ_{exc} = 920 nm. THG images at λ_{exc} = 1700 nm inside a fresh human colon biopsy are showed in figure 4.9 (b). Finally, 3PEF images of neurons inside a mouse brain acquired over a 45 µm thickness at λ_{exc} = 1300 nm are featured in figure 4.9 (c). Ideally, in order to produce a real 3D representation from these images, the gap between

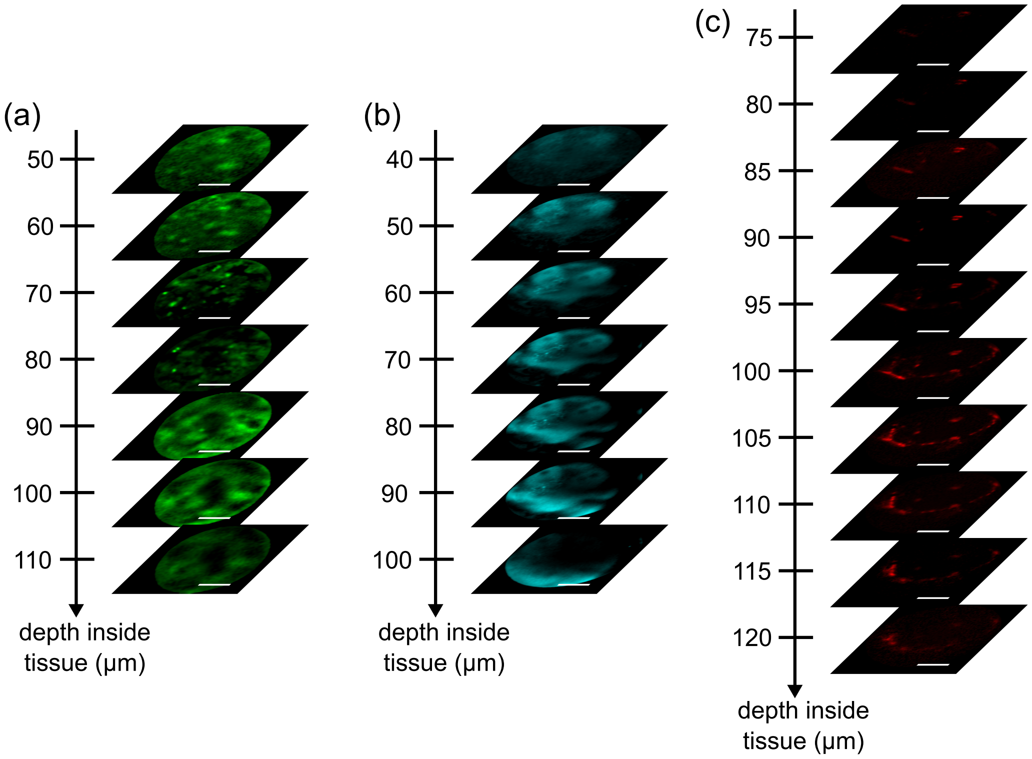

Figure 4.9: *Multiphoton images as a function of the depth under the sample surface. (a) 2PEF ($\lambda_{\text{exc}} = 920$ nm) images of a mouse liver. (b) THG ($\lambda_{\text{exc}} = 1700$ nm) images of a human colon.(c) 3PEF ($\lambda_{\text{exc}} = 1300$ nm) images of a mouse brain. Scale bars are respectively: (a, b) 50 μm and (c) 40 μm. Excitation average power on the sample are respectively: (a) 23 mW, (b) 27 mW and (c) 31 mW. Images are recorded with a 2 FPS acquisition rate and averaged over 5 images.*

consecutive images should be smaller than the axial resolution to provide a proper sampling.

4.2 CARS imaging

This section describes the experimental setup implemented to perform CARS imaging with the same endoscope used for multiphoton imaging. In this case, two excitation sources are needed to probe the vibrational transitions inside tissues. Spatial and temporal alignment considerations, as well as imaging trials are presented afterward.

4.2.1 Setup and excitation laser properties

The excitation source employed in the CARS setup, represented in figure 4.10, is made of a Ti:Sa laser (Chameleon, Coherent) pumping an optical parametric oscillator (Chameleon compact OPO, A.P.E). It delivers two beams with more flexibility than the source used for multiphoton imaging, described above, with the ability to tune both outputs separately. The energy difference between the excitation beams corresponds to the vibration of the targeted molecular bond. In our case, CH_2 and CH_3 chemical bonds, with energy around 2850 cm^{-1}, are excited and an emission wavelength of 700 nm is selected. It results in two excitation sources at λ_{pump} = 874 nm and λ_{Stokes} = 1164 nm for the pump and Stokes beams respectively. The laser provides both at 80 MHz repetition rate, and with pulse durations of 125 fs pulses (FWHM) for the pump and 250 fs pulses (FWHM) for the Stokes.

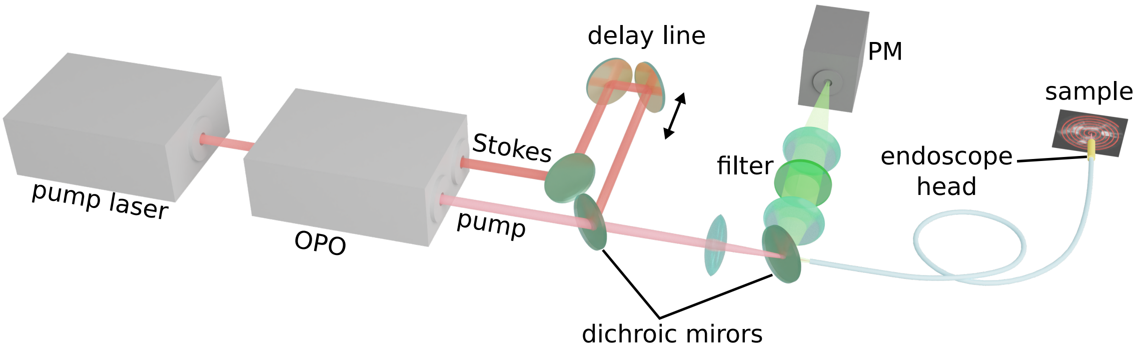

Figure 4.10: *Schematic representation of the experimental setup implemented to perform endoscopic CARS imaging. A second excitation beam (Stokes) is spatially overlapped with the pump beam with a dichroic mirror and temporally by means of a delay line.*

Spatial superimposition of the excitation beams is realized by adding a 950 nm dichroic mirror, depicted in figure 4.10. Alignment of both beams is first performed with two iris diaphragms far apart one another, then by maximizing injection into the FM of the DC-HCF for each beam separately. Temporal superimposition is performed by adding a delay line on the Stokes beam path. It is first coarsely placed based on the beam path of each outputs inside the OPO, then finely tuned to maximize the overlap between pump and Stokes pulses. The endoscope and detection channel remain unchanged from the experimental setup previously described for multiphoton imaging.

4.2.2 Pulse synchronization

Synchronization of the two excitation pulses is a central element to enable CARS imaging. Two mirrors set on a mechanical stage operated from a software with a 0.01

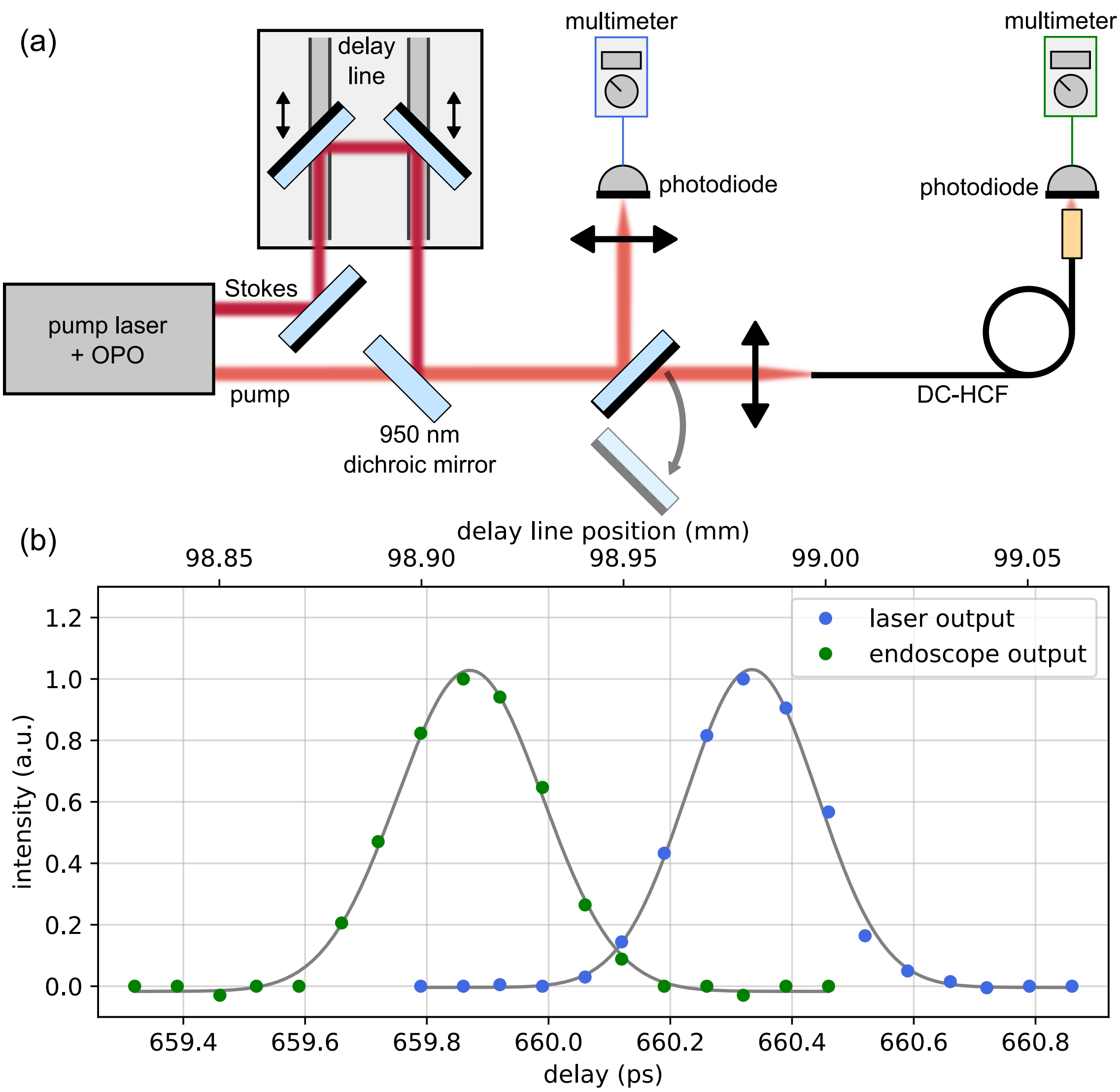

Figure 4.11: *(a) Experimental setup to temporally superimpose the pump and Stokes pulses. (b) Cross-correlation measurement and Gaussian fit (gray line) before (blue) and after (green) propagation inside the endoscope. Intensities are normalized to clearly depict both peaks, and the signal when pulses are not overlapping is set to zero. Temporal superimposition of the pulses is reached at the peak of the Gaussian function, and corresponds to a specific delay line position.*

mm precision allow to adjust the delay between pulses without affecting the spatial beams alignment. The overlap between pulses is estimated with a cross correlation measurement. Figure 4.11 (a) describes the experimental setup including a silicon photodiode placed immediately before or after propagation inside the endoscope to perform cross-correlation measurements using two photon absorption (TPA) in the photodiode. To provide sufficient power density on the detector, a lens with focal length $f' = 11$ mm focalizes the beams onto the photodiode placed before injection into the endoscope. No lens is needed at the distal end as the focalization is already provided by the optics of the endoscopic head.

Both excitation pulses generate a TPA signal inside the photodiode which is set to 1 V measured with a multimeter by adjusting the average power of each beam. Additionally, another signal is generated by absorption of one photon from each beam, only when pulses are overlapping. Therefore, cross-correlation is obtained by measuring the voltage generated from the photodiode when scanning the delay line position. Results are laid out in figure 4.11 (b), measured before (blue) and after (green) propagation inside the endoscope.

The cross-correlation traces, with a Gaussian shape, reveal the optimal position of the delay line to maximize the overlap between pump and Stokes pulses. We also note the shift in temporal alignment after propagation inside the endoscope, which correspond to about 500 fs. A pulse duration increase from 60 fs to 81 fs, measured at $\lambda = 1300$ nm, when adding the commercial GRIN fiber micro-objective to the scheme suggests that this is mainly caused by dispersion inside it. In fact, this dispersion effect can be beneficial in our case because the pulses will mostly not overlap inside the objective and gradually move closer to one another to be synchronized on the output sample. Yet it was presented in chapter 1 that the major effect causing noise to CARS imaging is FWM [116], which mostly happens inside the objective. Consequently, having weakly overlapping pulses should reduce FWM to an acceptable value.

4.2.3 CARS imaging

Hydrocarbon chains, lipids in particular, should emit a strong CARS signal because of their high concentration of CH_2 and CH_3 bonds. To estimate the impact of parasitic FWM as compared to CARS, we exploit this by recording the signal collected when placing a small olive oil tank at the output of the endoscope. For an excitation average power of 75 mW in total on the sample, a signal of about 3.5 M counts/s was recorded at different positions inside the oil sample. When completely removing the sample, and for the same excitation power, a signal of 80 k counts/s is measured. It grants a 43.75 SNR and the residual signal is believed to be mainly caused by parasitic FWM in the GRIN micro-objective. To ensure its origin, a slight misalignment of the delay line is provoked and results in a considerable raise of the noise level, corresponding to an increase in temporal overlap of the pulses inside the objective.

Synchronization of the pulses at the output of the endoscope should then allow high contrast CARS imaging with low FWM background. It is evidenced by images of fat cells inside a fresh human colon biopsy in figure 4.12 (a) and (b). Additionally, figure 4.12

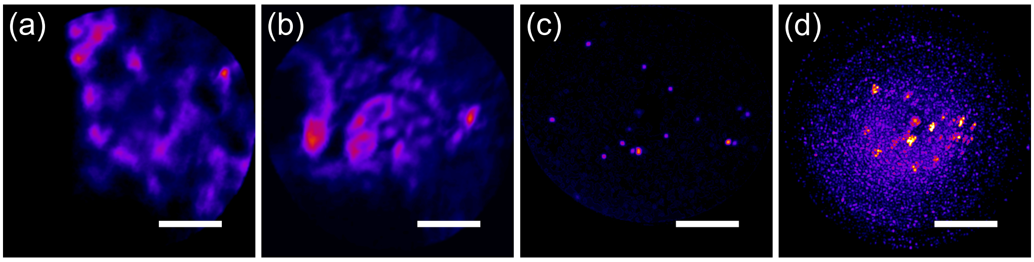

Figure 4.12: *CARS imaging ($\lambda_{\text{pump}} = 874$ nm, $\lambda_{\text{Stokes}} = 1164$ nm) on (a, b) a human colon and (c, d) an ox liver. Scale bars are respectively: (a) 50 µm, (b) 50 µm, (c) 25 µm and (d) 50 µm. Excitation average power on the sample is 19 mW for colon images and 12 mW for liver images. Images are recorded with a 2 FPS acquisition rate and averaged over 5 images.*

shows low (c) and high (d) lipid droplets density regions of fresh ox liver sample, of 5 cm thickness. This is performed by inserting the endoscope head 3 mm deep inside the tissue. It demonstrates the ability of the endoscope to be used freely for histological imaging, even deep bellow the surface.

4.3 Photo-bleaching limitation and perspectives

Regardless of the nonlinear imaging effect, the signal generated, and by extension the signal collected, remains quite weak. Increasing the excitation average power enhances the signal generation, up to a certain limitation over which photo-bleaching will be induced in the sample. It is caused by an irreversible alteration of the emitting molecules by the excitation source and leads to a suppression of nonlinear emission.

It is the primary cause of restrain on the imaging contrast, and is well known for devices performing with a piezoelectric scanner. Indeed, the resonant frequency of the spiral is constant, thus the duration to cover a full circle is also constant throughout the spiral scan. However, because the circles are smaller at the center of the pattern, the surface covered by unit of time is much smaller than on the outskirt. Consequently, the area around the image center will have a higher illumination. It means that the signal generated tends to be non-uniform, which could be numerically corrected, but also that photo-bleaching is more likely to happen at the center of the imaged area. Additionally, the center point is continually illuminated during the rest phase of the scanner cycle, as the fiber remains in an almost stationary position, which exacerbates the induced photo-bleaching.

To illustrate it, figure 4.13 (a) is a 3PEF image of mouse retina, similar to the one presented in figure 4.8 (k). When lightly increasing the excitation average power (in this case from 22 mW to 29 mW) and after a few image acquisitions, a large dark area appears at the center, due to photo-bleaching, and if we continue the acquisition, it grows until the image is completely blank.

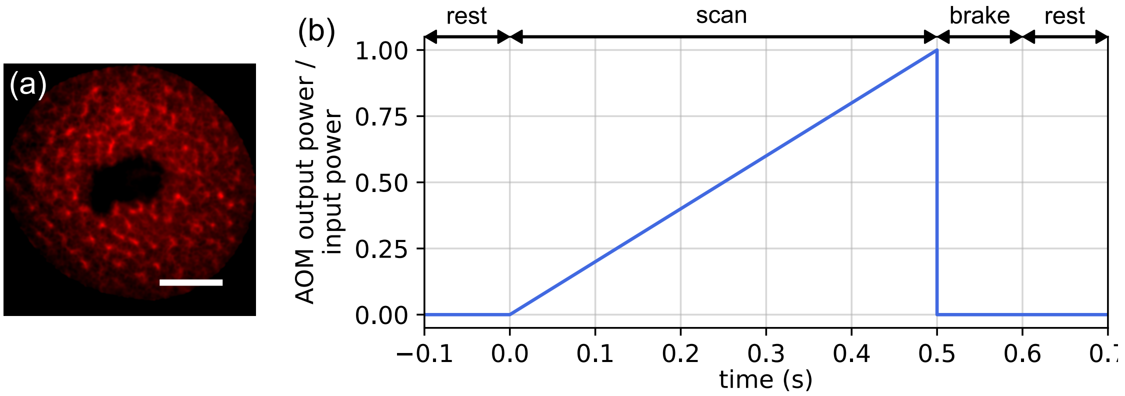

Figure 4.13: *(a) Example of photo-bleaching visible at the center of a 3PEF ($\lambda_{\text{exc}} = 1300$ nm) image of mouse retina. Scale bar is 50 µm, excitation average power on the sample is 29 mW, and acquisition rate is 2 FPS. (b) Acousto-optic modulation (AOM) applied to the excitation source to restrain photo-bleaching effects.*

Because of this issue, imaging contrast was limited throughout this work and some samples could not be imaged properly even though nonlinear signals were generated and detected. To overcome this limitation, the addition of an acousto-optic modulator (AOM) to the experimental setup is currently under investigation. The idea is first to allow the fiber to deliver an excitation signal only during the scan phase, but also to add a modulation that lets the power increase during the spiral scan. Figure 4.13 (b) shows an example of acousto-optic modulation that could be applied to the excitation light by an AOM placed just before injection into the fiber, with a linear ramp during the scan, and no transmission during the rest of the scanning cycle. Alternatively, a sinusoidal modulation can be employed to better fit the shape of the scanner driving signals.

Conclusion

The reported results show that, although 2PEF and 3PEF modalities grant the same chemical information about biological tissues, 3PEF provides an improved axial resolution, as well as an increase in SNR. Additionally, because of the higher excitation wavelength, 3PEF should also allow to image much deeper below the tissue surface, although this could not be demonstrated here because of the limited working distance of the GRIN micro-objective. Besides, the present endoscope is the first reported demonstration of 3PEF endoscopic imaging of unstained biological tissues. Moreover, images presented in this chapter demonstrate the high multimodality of the endoscope assembled, integrating 2PEF, SHG, 3PEF, THG and CARS modalities in a single device. It is capable of imaging biological tissues, fixed or fresh, without the need to stain them.

Chapter 5

Hollow core double clad fiber coupler (HC-DCFC)

Signal collection is a crucial element in the endoscope scheme, and three parameters are to be taken into account when implementing it: collection efficiency, bulkiness and overtime stability. Collecting with a double clad fiber (DCF) grants the smallest probe size, yet a separation of collection and excitation scheme must be added to the proximal end of the fiber. In the previous chapters, this separation was performed by a dichroic mirror, but the NA mismatch between the hollow core and the double clad of the fiber made it mandatory to use different lenses for injection and collection. The resulting spatial clutter renders the alignment more complicated. This scheme is also prone to misalignment over time, requiring a regular adjustment to maintain optimal performances.

Alternatively, separating collection from excitation with a double clad fiber coupler (DCFC) [117–122] seems to be the ideal solution to match the setup requirements as the collection fiber can be plugged directly to the detector. Yet, such device has never been reported with hollow core fibers because of the incompatibility of the fabrication process.

This chapter presents the first fabrication of a hollow core double clad fiber coupler (HC-DCFC) and its implementation in nonlinear endoscopy. First, the context and state of the art of DCFC is outlined. We then present numerical simulations, with beam propagation method, leading to a target design, and the fabrication considerations to realize such a device. Finally, a full characterization of the coupler and its implementation into a nonlinear endoscope is demonstrated.

5.1 State of the art and motivations

In a nonlinear endoscopy scheme, signal collection can either be performed by the same fiber as the excitation delivery, or by a separate collection only fiber [123]. In the latter, there is no need for an additional device to separate collection from excitation as two distinct fibers are used, and the collection fiber can be directly plugged to the detector with appropriate filters. However, it results in a bulkier endoscopic head with a more complicated design. Alternatively, nonlinear collection can be performed by the same fiber as the excitation delivery by addition of a double clad, as it was presented above. The excitation / collection separation is then moved to the proximal part of the endoscope where bulkiness is not much an issue.

5.1.1 Core / cladding separation in endoscopic fiber

When excitation and collection signals propagate inside the same optical fiber, respectively inside the core and inner cladding, a separation scheme must be added to the proximal end of the endoscope. In the results presented heretofore, it was accomplished by adding a dichroic mirror and a collection lens. An example of experimental setup as such is represented in figure 5.1 (a). Despite its ability to be successfully implemented in an endoscopy setup, as demonstrated in the previous chapter, this solution is not ideal. The collection lens must match the NA of the DC-HCF cladding, and the injection lens that of the fiber core. Because of the large mismatch between both, injection and collection must be performed with different optics. Consequently, the dichroic mirror has to be placed between the fiber tip and the optics. The alignment is thus more complicated, time-consuming and prone to misalignment.

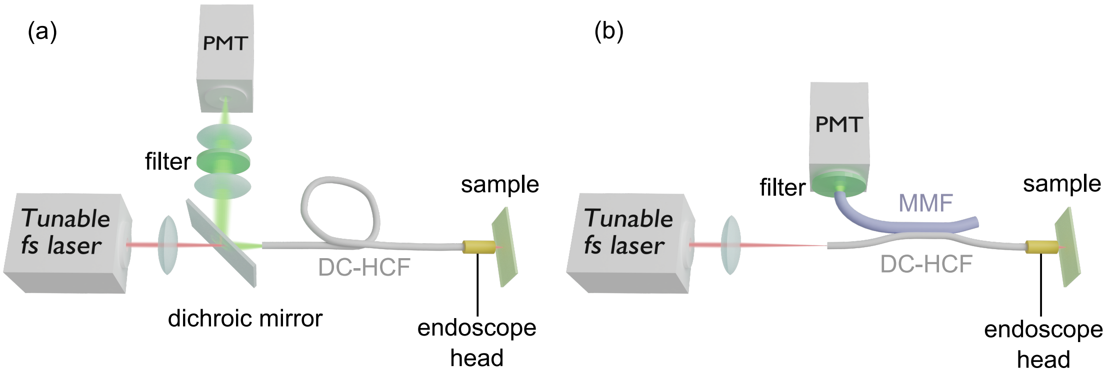

Figure 5.1: *Schematic representation of an experimental setup to perform nonlinear endoscopic imaging, where excitation and collection signals are separated either (a) with a dichroic mirror and optics, or (b) with a DCFC.*

Moreover, such a setup needs to be realigned on a regular basis in order to maintain optimal performances. Still, it is essential for endoscopes to be readily usable at any time and maintain performances, even for long imaging sessions. To overcome these difficulties, DCFCs have been integrated into endoscope schemes [52, 119].

Figure 5.1 (b) shows an endoscopy setup where excitation / collection separation is accomplished by a DCFC. The injection into the fiber core remains unchanged, but as much as possible of the multimode signal collected is coupled to a second fiber. The latter is then directly plugged to the detector, with appropriate collection filter.

5.1.2 Double clad fiber coupler with solid core fibers

All DCFC reported so far have revolved around step index solid core DCF. First demonstrations involved two identical DCFs, arranged such as presented in figure 5.2 (a). In early reports, DCFC were fabricated without fusion, either by side etching the fibers and pressing them one against the other [117], or by twisting them [118]. Yet the multimode (MM) transfer, from the double clad of one fiber to the other, only reached about 30 %.

Adding a fusion step, and eventually tapering, to the fabrication process allowed to draw near a 50 % MM transfer [119]. As a matter of fact, it is the theoretical limit in such a symmetric coupler design [120].

On the other hand, this limitation was outperformed by switching to an asymmetrical design [121], represented in figure 5.2 (b). The fusion and tapering process remains the same, as does the collection DCF. The receiving MMF, however, has a larger diameter, and because only a multimode transmission is needed, the core is removed. The

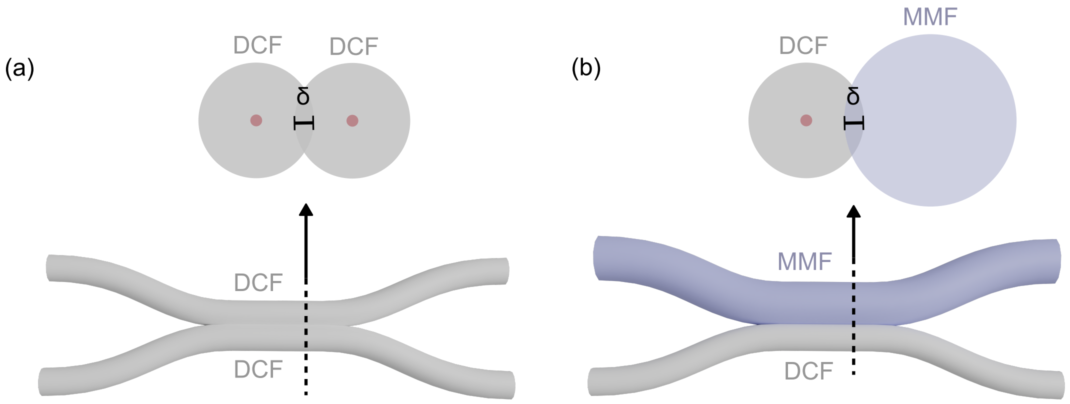

Figure 5.2: *Lateral view of (a) symmetric and (b) asymmetric DCFC schematically represented, with a transverse view at the vertical dashed line. The black horizontal segment represents the so-called overlap δ between fibers.*

simplest model for this coreless MMF is a silica rod, but any MMF can be considered. MM transfer as high as 70 % is reached with this design, and even 80 % when twisting the fibers during fusion to an almost circular coupler cross-section [122].

5.1.3 Double clad fiber coupler with hollow core fibers

The coupler designs with solid core double clad fibers presented above grant substantial results that enabled DCFCs to be integrated in nonlinear endoscopy setups [52, 121]. However, in this work we focused our attention to hollow core DCFs because solid core DCFs based endoscopes are limited in peak power delivery, even with dispersion and nonlinearity pre-compensation, and their use is generally restrained to a single excitation wavelength (see chapter 1).

A hollow core double clad fiber coupler (HC-DCFC) would be ideal to provide robustness and ease of use to the experimental setup. Yet it has never been reported, chiefly because of the inadequacy of a fusion process to be applied to hollow core fibers without impacting the microstructure. In the following sections, we propose a DCFC design with a fabrication process especially conceived for microstructured hollow core fibers, to match as best as possible the state-of-the-art solid core DCFCs performances.

5.2 Design and fabrication

5.2.1 Numerical simulations

Relying on previously reported work, we decided to opt for an asymmetric DCFC design, with a simple rod as the MMF to maximize the MM transfer from the double clad of the endoscopic fiber. To determine the target outer diameter of the MMF, we first take a look at the transmission analytical formula from [121] that calculates the MM transfer in such a design. It is based on the optical etendue calculation $G = \pi S(NA)^2$, where NA is the numerical aperture of the fiber and S the surface of its cross-section[1]. The multimode transfer from the DCF to the MMF is calculated as such [121] :

$$T = \frac{G_{MMF}}{G_{MMF} + G_{DCF}} = \frac{1}{1 + \frac{G_{DCF}}{G_{MMF}}} \tag{5.1}$$

Based on this formula and the parameters of the DCF, namely a 300 µm outer diameter and a 0.38 NA, we calculate the MM transfer to a MMF as a function of its outer diameter in figure 5.3. For a first estimation, the NA of the MMF is assumed to be

---

[1] In the case of the endoscopic fiber, only the cross-section of the double clad is taken into consideration.

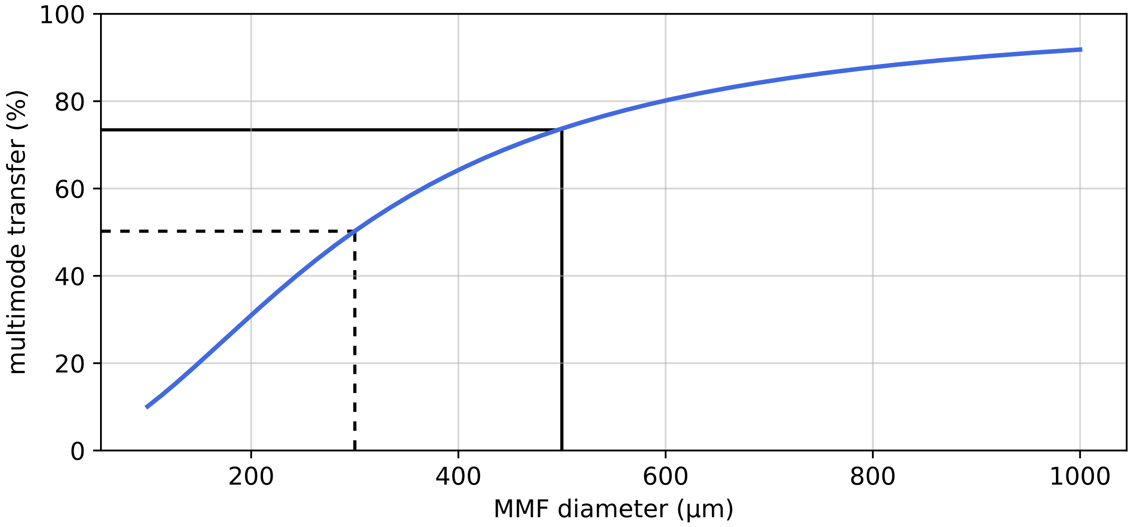

Figure 5.3: *Multimode transfer inside an asymmetric DCFC as a function of the MMF diameter, calculated from equation 5.1. The DCF diameter is fixed at 300 µm, and the coupling length is considered to be infinite. The black dashed line represents a symmetric coupler design, and the black solid line the target design with a MMF of 500 µm outer diameter.*

equal to the DCF's. As we can expect, a symmetric design provides a 50 % MM transfer (black dashed lines), while for a larger MMF, it sharply increases to about 80 %, for a MMF diameter D_{MMF} = 600 µm, then continues increasing but on a much softer slope.

To allow a sufficient MM transfer, we chose a 500 µm outer diameter MMF, which should provide more than 70 % MM transfer (black solid lines in figure 5.3). We could further increase it for better performances, but it would also make the MMF more fragile and delicate to manipulate, which would in term reflect on the coupler. Besides, the enhancement would not be substantial, and a larger MMF could have increased propagation losses.

To further elaborate the coupler design, we perform numerical simulations based on a beam propagation method (BPM) using a finite element method [124] to study the impact of the coupling length. Firstly, we ensure the MM transfer calculation is correctly performed by plotting in figure 5.4 the MM power inside the DCF (dashed lines) and the MMF (solid lines) with respect to the number of input modes inside the DCF.

After a certain propagation distance inside the coupler, the power in each fiber reaches a constant value, regardless of the number of modes at the input. We also note that the MM transfer to the MMF is about 70 %, confirming results previously obtained from the analytical formula of [121].

On the other hand, the propagation distance needed to reach the maximal transfer

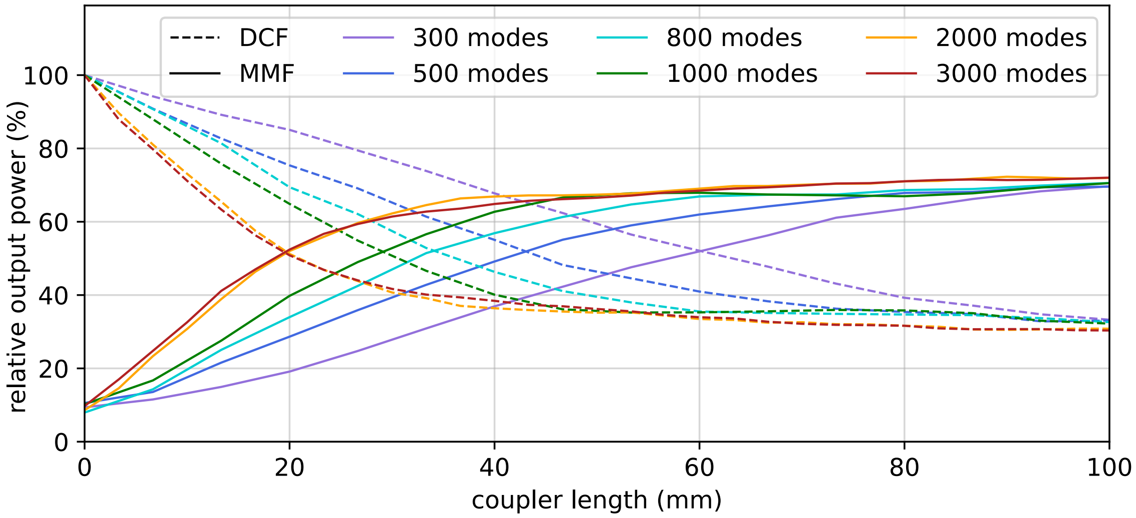

Figure 5.4: *BPM simulation of the multimode power inside the DCF (dashed lines) and MMF (solid lines) of a HC-DCFC depending on the coupling length, for several input modes.*

from one fiber to the other largely depends on the number of input modes. It is about 100 mm when 300 modes are set at the input of the DCF, and drops down to about 30 mm for 2000 modes. However, when increasing the number of modes over 2000, no notable shift is observed, suggesting that 2000 modes is sufficient to properly simulate the MM propagation inside the DCF. Hence, the following simulations will be performed with this value.

Besides the coupling length, the contact surface between the fibers is a major parameter in defining the coupler performances. We define it here by the distance between the fibers outer edge, and call overlap δ, as depicted by a horizontal black line in figure 5.2.

Figure 5.5 shows the simulated MM transfer for a 30 µm (blue lines) and 50 µm (red lines) overlap between fibers. Similarly to the results obtained above, the MM power in each fiber tends to a constant value irrespective of the overlap, but it is reached quicker when the contact surface is increased.

The only issue of a higher overlap value is the constraints it creates for the fabrication process, thus the value will be set by the maximal attainable in practice as we shall see hereafter. We also keep in mind that, for a fixed value of the overlap δ, adjusting the coupler length, *i.e.* the length over which the fibers will be spliced, is also possible to reach the maximal MM transfer.

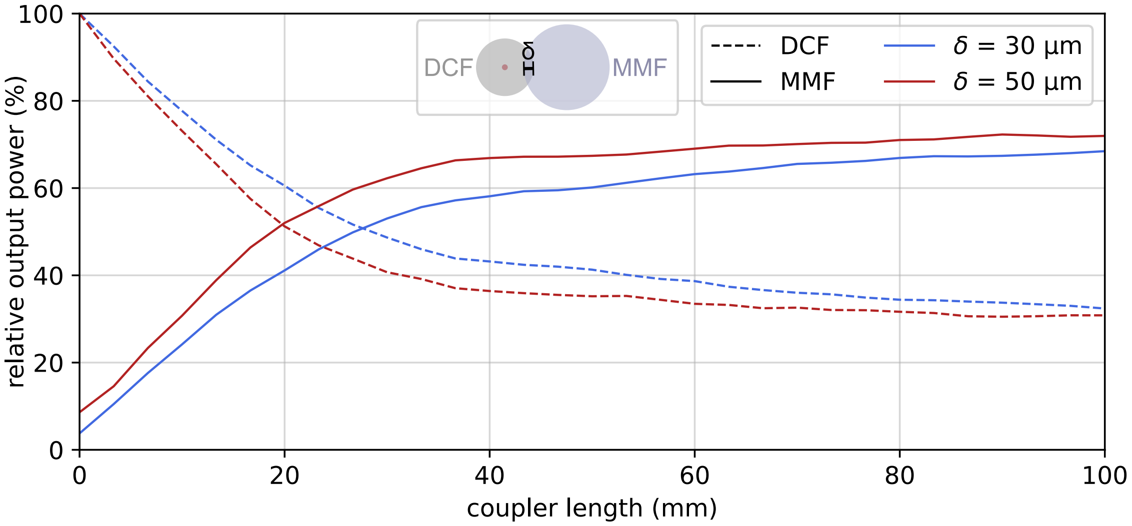

Figure 5.5: *BPM simulation of the multimode power inside the DCF (dashed lines) and MMF (solid lines) of a HC-DCFC depending on the coupling length, for an overlap between fibers of* δ *=30 µm (blue) and* δ *=50 µm (red).*

5.2.2 Fabrication process

To develop the fabrication process, identify the optimal parameters and evaluate the performances of the coupler, we first use a simple silica capillary fiber, of 300 µm outer diameter and 70 µm inner diameter, to mimic the DC-HCF without having to fabricate a complicated microstructured fiber. Indeed, only the double clad is needed to measure the MM transfer, and just a large hollow core is sufficient to estimate the impact of the fabrication process. A low index polymer (Desolight DF-0016) surrounds the fiber to ensure guidance, to which a high index polymer layer is added for mechanical protection.

A splicing of the capillary fiber to a silica rod fiber, with the same double polymer coating and a 500 µm outer diameter (MMF), is performed to obtain the highest possible MM transfer. As opposed to previously reported studies [119–122], no elongation is performed during heating here as it is bound to generate distortions of the hollow microstructure. The coupler fabrication process is represented in figure 5.6 (a). For the fibers to be in contact on the whole splicing length, they have to be held against each other without their coating. For this, both fibers are stripped of their polymer coating on a 20 cm length so that they can be pressed against each other in V-shaped groove holders (clamps) on either side of the splicing area. Fusion between fibers is realized by a CO_2 laser (LZM-100, Fujikura) with control over the heating power and movement of the fibers with regard to the laser beam. To avoid any distortion of the fibers caused by

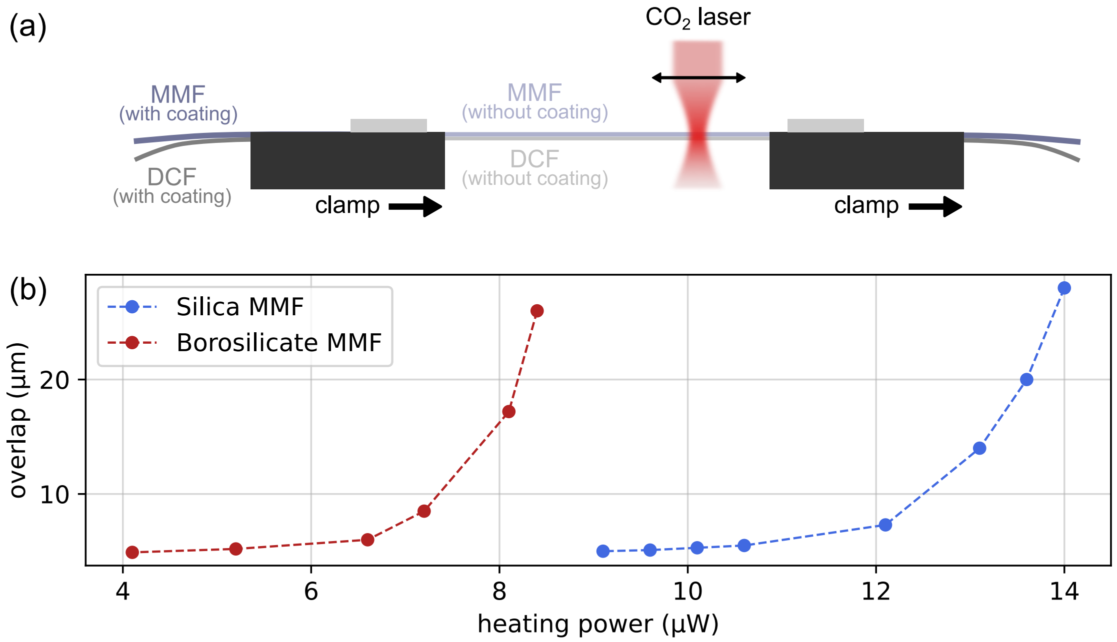

Figure 5.6: *(a) Schematic representation of the DCFC fabrication process. (b) Measured overlap parameter δ between the fibers of a HC-DCFC as a function of the CO$_2$ laser heating power. Measurements were realized using a silica (blue dots) or and borosilicate glass (red dots) MMF.*

a relaxation of the constraints at the process start, linear heating ramps are added at the beginning and end of the process. After the fabrication process, the overlap between fibers can be measured with an optical microscope after cleaving the coupler. Figure 5.6 (b) shows a direct correlation measured between overlap and heating power for a 500 µm outer diameter silica (blue dots) or borosilicate glass (Simax glass, red dots) MMF. Once the fibers are fused, the portion stripped of coating is re-coated using a homemade device with a low index polymer to provide guidance and protection to the coupler.

After splicing at different heating power, and while measuring the overlap, we also measure the inner diameter of the capillary fiber and plot it as a function of the measured overlap in figure 5.7. The inner diameter, initially 70 µm and marked with a horizontal dashed black line, is significantly reduced when increasing the overlap between the capillary fiber and the silica rod MMF (blue dots). For an overlap > 20 µm, the hollow core even completely collapses as attested by the inset picture of figure 5.7. In fact, even for an overlap close to 0, where fibers are barely spliced, the inner diameter is still reduced to < 60 µm. This is a major issue as the hollow microstructure can not be kept unchanged, hence the guidance properties would be affected as well. We note that this issue could be addressed by pressurizing the hollow core and hollow capillaries of the

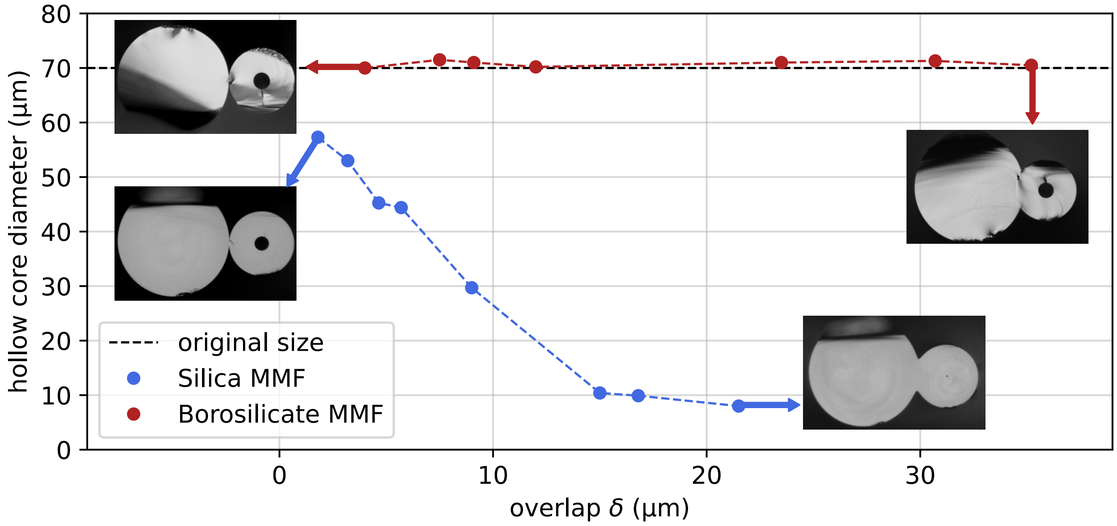

Figure 5.7: *Measured capillary fiber hollow core diameter as a function of the overlap parameter δ between the fibers of a HC-DCFC for a silica (blue dots) or borosilicate (red dots) MMF. The horizontal black dashed line is the hollow core diameter measured on the capillary fiber before the fabrication process. Insets show a transverse view of the couplers fabricated at low and high overlap in both cases, and are acquired using an optical microscope.*

fiber during the process, similarly to the pressure applied during the fiber draw (see chapter 2). Still, it would be very complicated to achieve as both need to be pressurized separately inside the fiber, which is much smaller than the cane pressurized during the fiber draw.

However, this drawback can be addressed by switching the MMF to a different material with a fusion temperature far lower than silica. In this case, the MMF can be heated to a softening point, and spliced to the DCF, while remaining far under the fusion temperature of silica, and therefore without affecting the silica fiber. Apart from the fusion temperature, the MMF material must have a higher refractive index than silica and be transparent in the visible range, to allow MM transfer of the nonlinear signals collected. An adequate and low-cost option is to use a borosilicate glass. For instance, in this work we use Simax glass. Its melting point is about 820°C, far lower than silica (1710°C), and its refractive index is 1.478 at 500 nm, which is higher than silica (1.462). As for the fabrication process, the only restriction is to keep the MMF, which will be the only melted fiber, above the DCF.

As attested by the red dots and insets of figure 5.7, when fusing the capillary silica fiber to a borosilicate 500 µm diameter rod, the inner diameter remains unchanged at 70 µm even for overlap > 30 µm. Consequently, the borosilicate MMF allows to fabricate the coupler with an overlap as high as 35 µm without affecting the hollow structure of the capillary fiber. For heating power corresponding to higher overlap, distortions of the borosilicate fiber tended to appear and the process was no longer repeatable. Still, further inquiries will be presented subsequently in this chapter to ensure that the fabrication process does not affect the structure nor the performances of an actual microstructured DC-HCF.

5.2.3 Optimal fabrication parameters

In order to establish the best suited parameters that maximize the MM transfer from the DCF to the MMF, we once again use the silica capillary fiber of 300 µm outer diameter and 70 µm inner diameter, coupled with a 500 µm outer diameter borosilicate rod as the MMF. Different DCFC with various parameters are fabricated then characterized to determine their MM transfer, using the experimental setup represented in figure 5.8. The source is a homemade supercontinuum that covers the visible spectrum. With it, a bandpass filter allows addressing individual wavelengths. To ensure proper excitation of all guided modes inside the double clad of the capillary fiber, injection is performed using a x40 microscope objective with a NA of 0.65 far higher than the fiber of NA = 0.38, and preceded by an optical diffuser in order to fill the pupil of the microscope objective. The power at the output of both fibers is measured and compared to the input power after cleaving the capillary fiber 10 cm before the coupler start. If not specified, all fiber lengths, before and after the spliced area, are kept identical throughout the results presented hereafter to provide a proper comparison regardless of the propagation loss. Indeed, the following results inherently include the propagation loss of the fibers, which will be addressed hereafter.

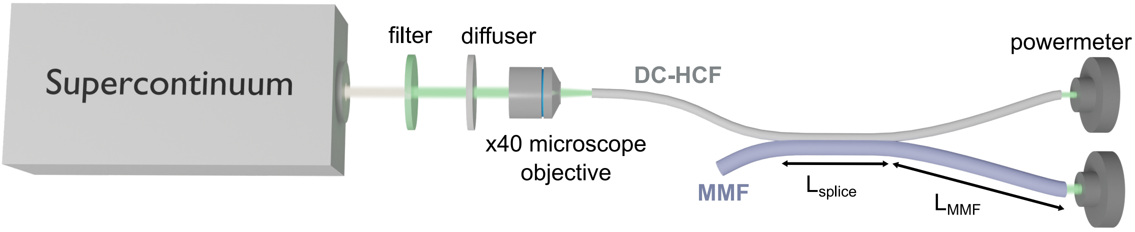

Figure 5.8: *Schematic representation of the experimental setup realized to characterize the HC-DCFC. Injection inside the double clad is performed with a high NA (0.65) microscope objective.*

Recoating of the coupler is performed immediately after fabrication to avoid any external contamination on stripped fibers. However, the recoating process itself could induce losses, due to impurities or air bubbles for instance. Figure 5.9 (b) shows the measured MM transfer over the visible range for a DCFC immediately after fabrication (blue dots) and after the recoating process (green dots). Almost identical performances

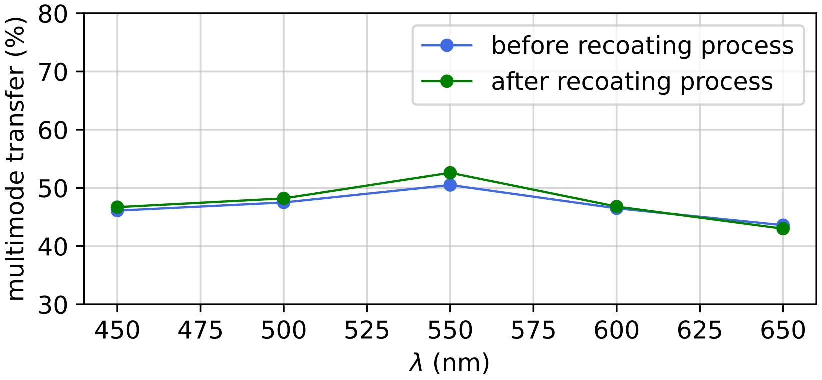

Figure 5.9: *Measured multimode transfer of a DC-HCF with a 300 µm diameter DC-HCF and a 500 µm outer diameter borosilicate MMF before (blue dots) and after (green dots) the recoating process.*

are obtained in both cases, indicating that the recoating process does not lead to any significant additional loss.

As suggested from the BPM simulations, the two main geometrical parameters affecting the performances of the DCFC are the spliced length and the overlap parameter δ. To optimize the fabrication process, we tested each independently. Figure 5.10 (a) shows the MM transfer at 500 nm from the capillary fiber to the MMF with respect to

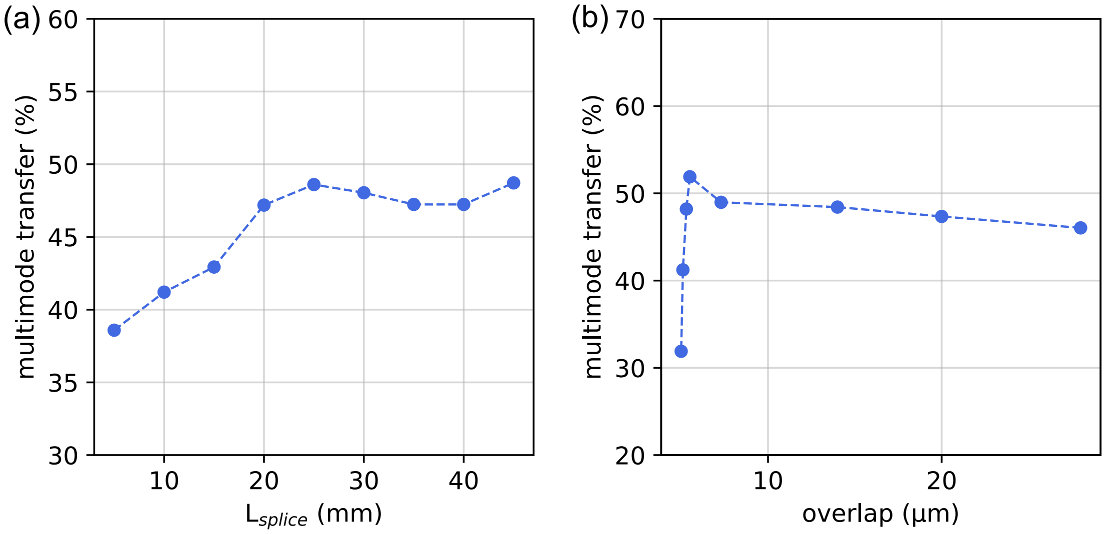

Figure 5.10: *Measured multimode transfer of a HC-DCFC with a 300 µm outer diameter DC-HCF and a 500 µm outer diameter borosilicate MMF as a function of (a) the coupler length L_{splice} and (b) the overlap parameter δ.*

the spliced length L_{splice}. The overlap parameter δ is here fixed at 15 µm. As expected, an increase in MM transfer with the coupler length is observed until an almost constant value, just under 50 %, is reached for $L_{\text{splice}} > 20$ mm. We note that this value is under the expected 70 %, and will address it below. Similarly, we measured the MM transfer as a function of the overlap parameter δ for a fixed spliced length $L_{\text{splice}} = 25$ mm. The results, depicted in figure 5.10 (b), show again an almost constant MM transfer but with a sharp decrease for overlaps smaller than 7 µm. Consequently, an overlap parameter δ of 10 to 30 µm and a coupler length of 20 to 50 mm should provide optimal performances of the coupler in terms of MM transfer to the borosilicate MMF. Fixing parameters in these ranges should also allow for repeatable efficiency. Therefore, all subsequent results presented here will concern a DCFC with $\delta = 15$ µm and $L_{\text{splice}} = 25$ mm.

Even though replacing the silica rod by a borosilicate fiber allowed us to successfully fabricate a HC-DCFC, its material losses in the visible range, of interest to us here, remains an issue. Figure 5.11 (a) shows the propagation losses of a borosilicate rod of 500 µm outer diameter, measured with an experimental setup similar to the one in figure 5.8. Losses in the order of 10 dB/m are measured across the range of interest, meaning that only 10 % of the power remains after 1 m of propagation. In figure 5.11 (b), we illustrate this by measuring the MM transfer to the borosilicate MMF cleaved 20 cm after the coupler (green dots), then when the MMF is cleaved 10 cm after the coupler (blue dots). A very high improvement in MM transfer is observed when removing only 10 cm

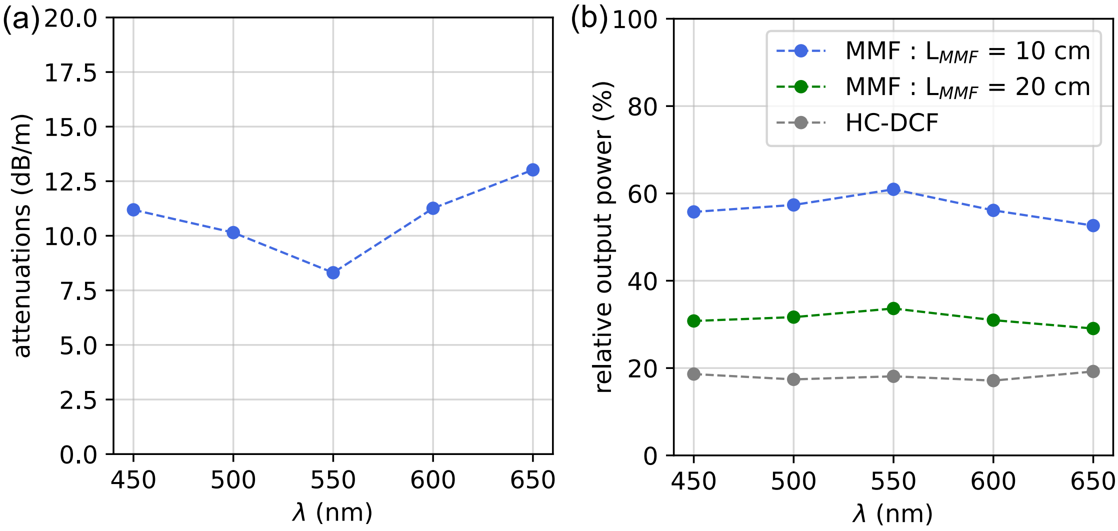

Figure 5.11: *(a) Measured attenuation spectrum of the 500 µm outer diameter borosilicate MMF. (b) Measured multimode transfer after 10 cm (blue dots) or 20 cm (green dots) of propagation inside the borosilicate MMF after the coupler, and residual signal inside the silica clad of the DC-HCF after the same coupler (gray dots).*

of borosilicate fiber, highlighting the significant impact of its propagation losses on the DCFC performances. We found that $L_{\mathrm{MMF}} = 10$ cm is the shortest length that allows to safely separate both fibers and place them on their respective channels (excitation for the DCF and detection for the MMF) without risking breaking them. Nevertheless, figure 5.11 (b) shows that a MM transfer of almost 60 % is achievable across the visible range with this coupler, which should be sufficient to perform a first endoscopic imaging demonstration. Moreover, we note that the power remaining in the double clad of the capillary fiber (marked by gray dots in figure 5.11 (b)) is just a little under 20 %. Hence, 80 % is the theoretical limit of MM transfer to the borosilicate MMF that we could attain with this coupler if free of propagation losses.

5.3 Coupler characterization

We have established that a HC-DCFC is attainable by using a borosilicate fiber in addition to the silica DCF, with multimode coupling from one fiber to the other allowing decent performances. We now fabricate a HC-DCFC with the process and parameters detailed above and replacing the capillary fiber by a double clad hollow core fiber similar to the endoscopic fiber described in chapter 2, of which a SEM is shown in figure 5.12 (a). Hollow core guidance is achieved with seven capillaries of 13.1 µm outer diameter and 350 nm wall thickness. The hollow core has a 34 µm diameter, resulting in a measured fundamental mode MFD of 30.5 µm. The first transmission band covers a large spectrum in the near infrared (NIR), from 800 nm to more than 1.8 µm, with propagation losses in the range of 0.6 dB/m. The fiber outer diameter is 200 µm, and it is spliced to a 500 µm outer diameter borosilicate rod over a 25 mm length and with a 15 µm overlap between fibers.

5.3.1 Multimode transfer

In section 5.2.3, we chose a capillary fiber with a design close to the double clad of the fiber previously mentioned to fabricate the nonlinear endoscope. Consequently, we observe similar performances with the full coupler fabricated. Still, because the DC-HCF is here slightly thinner (200 µm outer diameter), the size difference between fibers is larger. Hence, improved performances can be expected. With the borosilicate MMF cleaved 10 cm away from the coupler, we measure a MM transfer from the double clad of the DC-HCF to the MMF slightly above 60 % across the visible spectral range, alike figure 5.11 (b).

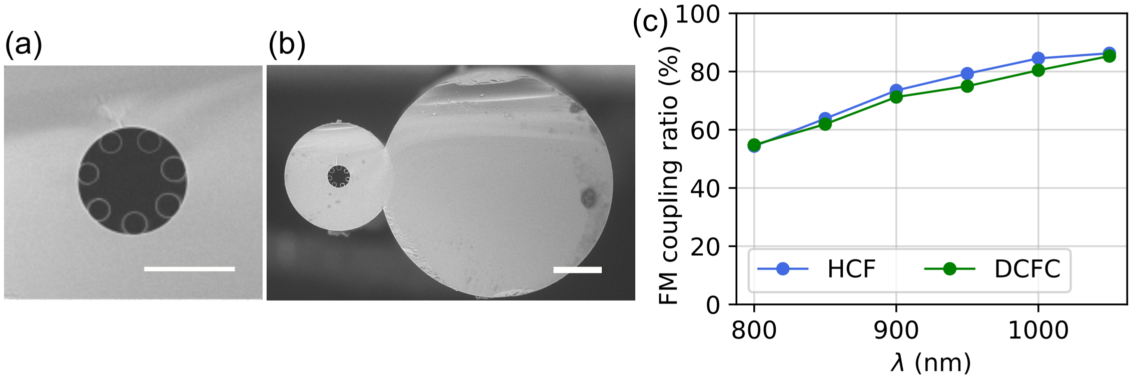

Figure 5.12: *Scanning electron micrograph of (a) the 7 capillary tubular DC-HCF and (b) the HC-DCFC fabricated with a 500 µm outer diameter borosilicate MMF. (c) Hollow core fundamental mode (FM) coupling ratio of the DC-HCF before (blue dots) and after (green dots) fabrication of the coupler.*

5.3.2 Hollow core transmission

Figure 5.12 (b) is a scanning electron micrograph (SEM) of the HC-DCFC fabricated. Geometrical properties of the microstructure were measured and less than 5 % difference from the original DC-HCF was observed. We can safely assure from this that the hollow microstructure of the fiber is unaltered by the coupler fabrication process, even with a heating step. The transmission properties of the hollow core are inquired by measuring the FM coupling ratio, *i.e.* the ratio of power at the output of the fiber to the power before injection to the core FM. Results in the NIR range are depicted in figure 5.12 (c) for the DC-HCF alone (blue dots) and after being spliced to the MMF (green dots). No significant drop of FM coupling ratio is observed after fabrication of the fiber, which states that the hollow core transmission properties are indeed not affected by the coupler fabrication.

We further highlight this by imaging the hollow core FM in figure 5.13 for the fiber before (a) and after (c) fabricating the coupler. The mode profile is also plotted along the dashed line for each (b and d), and a Gaussian fit is added (gray solid line) to certify the proper shape of the fundamental mode.

We fabricated a HC-DCFC that allows to retrieve about 60 % of the MM power from the double clad of the endoscopic fiber to a separate fiber, without affecting the excitation mode nor its transmission ratio. We now need to prove the applicability to an endoscopic setup, for nonlinear signal collection and detection.

5.3.3 Nonlinear signal collection in an endoscopic setup

The HC-DCFC performances are compared to the standard dichroic mirror separation of the excitation and collection channels in a real endoscopic setup. The experimental setup described in figure 5.1 (a) is realized, only without an endoscopic head. 166 fs excitation pulses at 920 nm with a 80 MHz repetition rate are provided by a Ti:Sa laser (Chameleon, Coherent) and injected to the DC-HCF core. On the distal end of the fiber, this excitation pulses generate a 2PEF signal on 2 µm fluorescent beads, placed on the surface of a coverslip as described in section 4.1.4. The 2PEF signal is separated from the excitation by a 850 nm dichroic mirror (Semrock) and isolated by a 565±66 nm bandpass filter, before detection by a photo-multiplier (PM, H7422-40, Hamamatsu). The fluorescent signal detected with respect to the excitation average power, measured before injection into the DC-HCF, is represented by the blue dots in figure 5.14 (a). A quadratic fit is included (gray solid line) to confirm the proper trend is measured.

Afterwards, the same fiber is used to fabricate a HC-DCFC with the process and parameters detailed above. The same experiment is repeated, following the setup of figure 5.1 (b) to generate and collect the 2PEF signal from 2 µm fluorescent beads. The green dots in figure 5.14 (a) show the dependence on excitation power of the signal detected. Although it is about 20 % lower than the signal detected with the dichroic mirror based setup, it is still in the same order which indicates that endoscopic imaging should be attainable. It should be noted that the sample used is rather homogeneous,

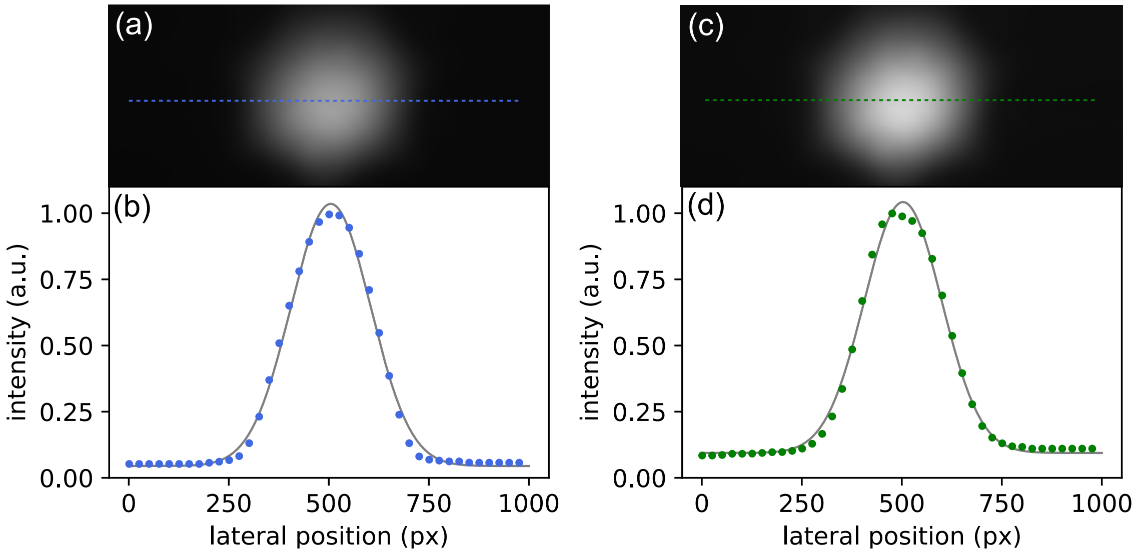

Figure 5.13: *Imaged hollow core FM of the DC-HCF before (a) and after (b) fabrication of the coupler, with (b, d) a profile plot along the marked horizontal dashed line and a Gaussian fit (gray solid line).*

but to avert any inconsistency that can be caused by a weakly emitting area on a specific position of the sample, each point in figure 5.14 (a) is a mean value of 5 acquisitions corresponding to different positions on the sample.

Moreover, the ratio of 2PEF signal measured with the HC-DCFC to the one measured with dichroic mirror with respect to the excitation power is depicted in figure 5.14 (b). Performances of the HC-DCFC setup are in the 65-75 % range from the more standard dichroic setup. It is higher than expected from the results acquired heretofore, which can be explained by avoidance of some losses when using a dichroic mirror and collection optics, namely absorption and reflection inside these optics, potential clipping if the beam is too large because of the high double clad NA, and because the dichroic mirror reflection rate is inherently < 1. We also note that performances seems almost identical for very low excitation average power (< 5 mW), which is actually caused by a SNR decrease to almost 1.

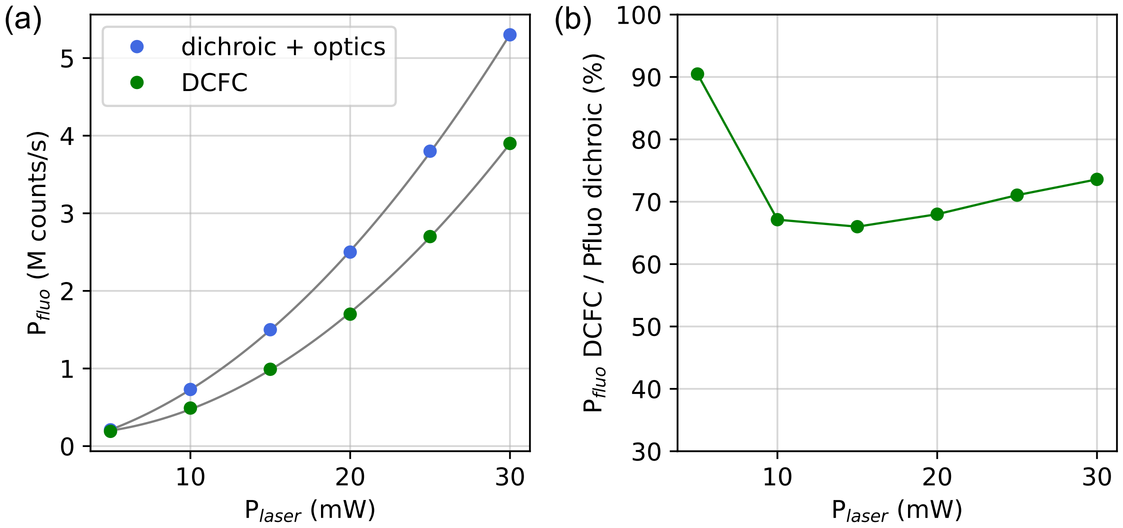

Figure 5.14: *(a) 2PEF signal generated on a sample of 2 µm fluorescent beads at the output of the DC-HCF, with* λ_{exc} *= 920 nm, and collected by the double clad of the same fiber, as a function of the excitation power. Collected signal is separated from the excitation either by a dichroic mirror and appropriate optics (blue dots) or by a DCFC with a 500 µm outer diameter borosilicate MMF (green dots), and (b) power ratio between both.*

5.3.4 Nonlinear imaging

Finally, we investigate the ability of the HC-DCF to be implemented in an actual nonlinear endoscope. For this, we functionalized the distal end of the hollow core with a 160 µm long GRIN lens of 60 µm core diameter. A commercial GRIN fiber based micro-objective (GRINTECH GmbH) added to the endoscope head allows to obtain a

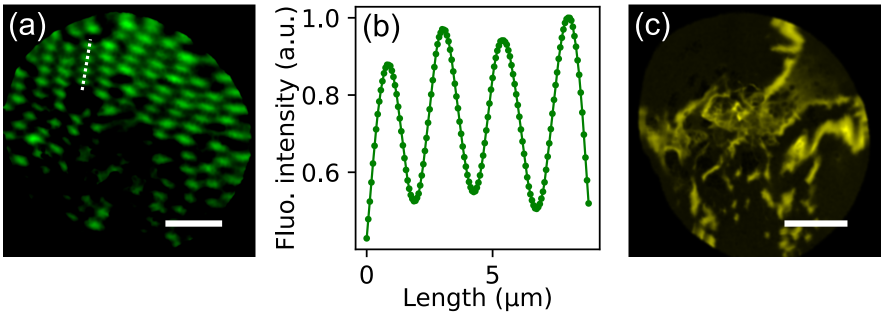

Figure 5.15: *(a) 2PEF image of 2 µm fluorescent beads with (b) an intensity plot along the white line (λ_{exc} = 920 nm), scale bar is 20 µm. (c) SHG image of unstained mouse skin (λ_{exc} = 920 nm), scale bar is 50 µm. Images have been acquired with a 2 fps acquisition rate and averaged over 5 images.*

1.3 µm PSF at the output of the endoscope, as well as a doubly resonant piezoelectric tube, providing performances similar to the endoscope characterized in the previous chapters.

We first demonstrate 2PEF imaging of 2 µm fluorescent beads in figure 5.15 (a) with an excitation wavelength of λ_{exc} = 920 nm. Alike imaging performed above, a 565±66 nm bandpass filter is preceding the detector to isolate the 2PEF signal. Figure 5.15 (b) displays a plot along the white dashed line in figure 5.15 (a). It shows that even with a weaker signal detection, a decent contrast is achieved, with beads contours well-defined.

We further emphasize on the imaging performances by providing a biological image of unstained mouse skin using SHG in figure 5.15 (c). Collagen fibrils, arranged in a rather disorganized manner, are undoubtedly emerging, as collagen is known to be a strong SHG emitter. Excitation is still realized at λ_{exc} = 920 nm and SHG signal is now detected using a 447±60 nm bandpass filter.

Conclusion

A hollow core double clad fiber coupler is demonstrated for endoscopic applications. The fabrication is made possible, including a fusion process, by combining two fibers of different materials, in our case silica and borosilicate glass. A 60 % multimode transfer from the double clad of the silica fiber to the borosilicate MMF and a 70 % nonlinear signal detected as compared to a similar setup without coupler are obtained, notably by designing an asymmetric coupler geometry. The main restraining issue is the high absorption losses of borosilicate in the visible range. Alternative materials can be used, as long as its fusion temperature is below silica and its refractive index is higher.

Nonlinear imaging is performed, even on unstained biological samples, demonstrating the applicability of this device to nonlinear endoscopy, which offers a simpler and more robust alignment, crucial for such applications.

Conclusions and perspectives

This thesis outlines the various nonlinear imaging modalities and their use cases for biological investigations. These techniques are useful because of their chemical specificity, improved resolution and penetration depth of the excitation source, ideal for endoscopy though it is still predominantly present in tabletop microscopy. We presented the requirements to transfer this technology to endoscopy, specifically to integrate 3PEF into the endoscope scheme. The delivery of high power ultrashort pulses to the sample is realized by a negative curvature hollow core fiber. To form a highly multimodal endoscope, the first transmission band ranges from 850 nm to more than 1750 nm, covering typical excitation wavelengths, with propagation losses under 0.7 dB/m and group velocity dispersion under 2 ps/nm/km. Collection and back propagation of the signal is performed by the same fiber, via a silica double clad with a large surface and high NA. The fiber is functionalized at its distal tip to reduce the large output mode, which improves the imaging resolution. It is carried out by either inserting a silica bead inside the hollow core, or splicing a GRIN lens to its endface. Although, we demonstrated that the GRIN lens functionalization allows to increase the imaging contrast by reducing the parasitic noise generated inside the endoscope.

Scanning is realized by a piezoelectric tube, exciting resonantly the fiber tip in two orthogonal directions to create a spiral pattern, with a field of view up to 600 µm with the micro-lens objective or 200 µm with the GRIN fiber objective. This objective is also added to the distal end, resulting in a working distance of 600 µm or 300 µm respectively. Distal parts of the endoscope are encased inside a 3 mm large and 40 mm long steel tube forming the endoscope head. Separation of the collection and excitation signals is performed at the proximal end of the fiber by a dichroic mirror and lenses for injection and collection. Although, an alternative solution is proposed with the first demonstration of a hollow core double clad fiber coupler. Its fabrication, with fusion from a CO_2 laser, is permitted by the use of two different materials, namely silica for the endoscopic DC-HCF and borosilicate glass for the collection multimode fiber. Despite the high propagation losses of the borosilicate glass in the visible range, a 60 % multimode transfer from the double clad fiber to the borosilicate MMF is measured, and a 70 % signal collection with respect to the alternative dichroic mirror based setup.

3PEF endoscopic imaging on unstained biological tissues is demonstrated for the first time, and adds to 2PEF, SHG, THG and CARS imaging modalities to form a highly multimodal endoscope. It is also, to our knowledge, the first demonstration of a nonlinear endoscope integrating all these imaging modalities. Moreover, CARS images obtained with the endoscope inserted 3 mm deep inside a fresh ox liver tissue demonstrated the usability of the endoscope. We have yet to demonstrate *in vivo* 3PEF imaging using this endoscope, but results presented in this work support the feasibility of such investigations, and 2PEF *in-vivo* images of neuronal activities inside a freely moving mouse have been attained recently. Yet some issues still need to be addressed. The working distance provided by the commercial micro-objective remains far from the performances of NLOMs, and increasing this would allow accessing the full potential of 3PEF imaging. Furthermore, we performed CARS imaging with sub-ps excitation pulses, which allowed us to take advantage of the dispersion inside the objective to temporally overlap both pulses only at the output of the endoscope. On the other hand, CARS imaging is often performed with longer excitation pulses to increase the spectral resolution, which has yet to be demonstrated with our endoscope design. Parasitic FWM generated inside the objective could rise due to a stronger temporal overlap of the pump and Stokes pulses, and hinder CARS imaging contrast.

Finally, because of the recent interest in 3PEF imaging and the versatility of a highly multimodal endoscope, many fields could benefit from such a device. In this scope, nonlinear micro-endoscope are destined to be commercialized to benefit lab research, and in term clinical investigations. In fact, commercialization is already in progress by a company called Lightcore Technologies, and development is under way, including in due time the hollow core double clad fiber coupler.

Author bibliography

Publications

- A. Kudlinski, A. Cassez, O. Vanvincq, D. Septier, A. Pastre, R. Habert, K. Baudelle, M. Douay, V. Mytskaniuk, V. Tsvirkun, H. Rigneault, G. Bouwmans, Double clad tubular anti-resonant hollow core fiber for nonlinear microendoscopy, *Optics Express* (2020).
- D. Septier, V. Mytskaniuk, R. Habert, D. LABAT, K. Baudelle, A. Cassez, G. Brevalle, M. Conforti, G. Bouwmans, H. Rigneault, A. Kudlinski, Label-free highly multimodal nonlinear endoscope, *Optics Express* (2022).
- D. Septier, A. Pastre, R. Bernard, G. Brevalle, D. LABAT, H. Rigneault, G. Bouwmans, A. Kudlinski, Hollow-core double-clad fiber coupler for nonlinear microendoscopy, in preparation.
- D. Septier, A. Cassez, G. Bouwmans, A. Kudlinski, Large hollow core multimode fiber, in preparation (work not presented in this thesis).

Communications (oral)

(speaker is underlined)

- D. Septier, G. Brévalle, G. Bouwmans, K. Baudelle, A. Cassez, D. Labat, R. Habert, V. Mytskaniuk, H. Rigneault, A. Kudlinski, Hollow core fibers for nonlinear microendoscopy. *ICPAMS-13* (**invited**).
- D. Septier, V. Mytskaniuk, R. Habert, D. Labat, K. Baudelle, A. Cassez, G. Bouwmans, H. Rigneault, A. Kudlinski, Functionalized double clad anti-resonant hollow core fiber designed for two and three photon nonlinear endoscopy. *Workshop GDR-ELIOS 2021.*
- D. Septier, G. Brévalle, G. Bouwmans, R. Habert, D. Labat, A. Cassez, K. Baudelle,

V. Mytskaniuk, H. Rigneault, A. Kudlinski, Flexible miniature 3-photon micro-endoscope using a functionalized hollow core fiber. *Photonics West (SPIE)*.

- D. Septier, V. Mytskaniuk, R. Habert, D. LABAT, K. Baudelle, A. Cassez, G. Brevalle, M. Conforti, G. Bouwmans, H. Rigneault, A. Kudlinski, *CLEO US (Optica)*
- D. Septier, V. Mytskaniuk, R. Habert, D. Labat, K. Baudelle, A. Cassez, G. Brévalle-Wasilewski, M. Conforti, G. Bouwmans, H. Rigneault, A. Kudlinski, Micro - endoscopie multimodale à trois photons sur tissus non marqués. *Optique Nice 2022 (SFO)*

Communications (poster)

- D. Septier, R. Habert, D. Labat, M. Conforti, A. Kudlinski, G. Bouwmans, Ajustement de la taille de mode de sortie d'une fibre à cœur creux à l'aide d'une fibre GRIN. *Optique Dijon 2021 (SFO)*

Bibliography

[1] W. Denk, J. H. Strickler, and W. W. Webb, Two-Photon Laser Scanning Fluorescence Microscopy, *Science* **248**, 73–76 (1990).

[2] M. Wagner, C. Redaelli, M. Lietz, C. A. Seiler, H. Friess, and M. W. Büchler, Curative Resection Is the Single Most Important Factor Determining Outcome in Patients with Pancreatic Adenocarcinoma, *British Journal of Surgery* **91**, 586–594 (2004).

[3] M. Jain, N. Narula, A. Aggarwal, B. Stiles, M. M. Shevchuk, J. Sterling, B. Salamoon, V. Chandel, W. W. Webb, N. K. Altorki, and S. Mukherjee, Multiphoton Microscopy: A Potential "Optical Biopsy" Tool for Real-Time Evaluation of Lung Tumors Without the Need for Exogenous Contrast Agents, *Archives of Pathology & Laboratory Medicine* **138**, 1037–1047 (2013).

[4] T. Pham, B. Banerjee, B. Cromey, S. Mehravar, B. Skovan, H. Chen, and K. Kieu, Feasibility of Multimodal Multiphoton Microscopy to Facilitate Surgical Margin Assessment in Pancreatic Cancer, *Applied Optics* **59**, G1–G7 (2020).

[5] R. Boyd, Nonlinear Optics, Elsevier, (2020).

[6] N. Horton, K. Wang, D. Kobat, C. Clark, F. Wise, C. Schaffer, and C. Xu, In Vivo Three-Photon Microscopy of Subcortical Structures within an Intact Mouse Brain, *Nature Photonics* **7**, 205–209 (2013).

[7] W. R. Zipfel, R. M. Williams, R. Christie, A. Y. Nikitin, B. T. Hyman, and W. W. Webb, Live Tissue Intrinsic Emission Microscopy Using Multiphoton-Excited Native Fluorescence and Second Harmonic Generation, *Proceedings of the National Academy of Sciences* **100**, 7075–7080 (2003).

[8] H. Rigneault and P. Berto, Tutorial: Coherent Raman Light Matter Interaction Processes, *APL Photonics* **3**, 091101 (2018).

[9] K. Harpel, R. D. Baker, B. Amirsolaimani, S. Mehravar, J. Vagner, T. O. Matsunaga, B. Banerjee, and K. Kieu, Imaging of Targeted Lipid Microbubbles to Detect Cancer Cells Using Third Harmonic Generation Microscopy, *Biomedical Optics Express* **7**, 2849 (2016).

[10] N. V. Kuzmin, P. Wesseling, P. C. d. W. Hamer, D. P. Noske, G. D. Galgano, H. D. Mansvelder, J. C. Baayen, and M. L. Groot, Third Harmonic Generation Imag-

ing for Fast, Label-Free Pathology of Human Brain Tumors, *Biomedical Optics Express* **7**, 1889 (2016).

[11] S. Mehravar, B. Banerjee, H. Chatrath, B. Amirsolaimani, K. Patel, C. Patel, R. A. Norwood, N. Peyghambarian, and K. Kieu, Label-Free Multi-Photon Imaging of Dysplasia in Barrett's Esophagus, *Biomedical Optics Express* **7**, 148 (2016).

[12] S. Witte, A. Negrean, J. C. Lodder, C. P. J. de Kock, G. Testa Silva, H. D. Mansvelder, and M. Louise Groot, Label-Free Live Brain Imaging and Targeted Patching with Third-Harmonic Generation Microscopy, *Proceedings of the National Academy of Sciences* **108**, 5970–5975 (2011).

[13] Y. Wu, Y. Leng, J. Xi, and X. Li, Scanning All-Fiber-Optic Endomicroscopy System for 3D Nonlinear Optical Imaging of Biological Tissues, *Optics Express* **17**, 7907 (2009).

[14] K. Murari, Y. Zhang, S. Li, Y. Chen, M.-J. Li, and X. Li, Compensation-Free, All-Fiber-Optic, Two-Photon Endomicroscopy at 155 Mm, *Optics Letters* **36**, 1299 (2011).

[15] G. Ducourthial, P. Leclerc, T. Mansuryan, M. Fabert, J. Brevier, R. Habert, F. Braud, R. Batrin, C. Vever-Bizet, G. Bourg-Heckly, L. Thiberville, A. Druilhe, A. Kudlinski, and F. Louradour, Development of a Real-Time Flexible Multiphoton Microendoscope for Label-Free Imaging in a Live Animal, *Scientific Reports* **5**, 1–9 (2015).

[16] H. Guan, D. Li, H.-c. Park, A. Li, Y. Yue, Y. A. Gau, M.-J. Li, D. E. Bergles, H. Lu, and X. Li, Deep-Learning Two-Photon Fiberscopy for Video-Rate Brain Imaging in Freely-Behaving Mice, *Nature Communications* **13**, 1534 (2022).

[17] T. A. Birks, P. J. Roberts, P. S. J. Russell, D. M. Atkin, and T. J. Shepherd, Full 2-D Photonic Bandgaps in Silica/Air Structures, *Electronics Letters* **31**, 1941–1943 (1995).

[18] F. Benabid, J. C. Knight, G. Antonopoulos, and P. S. J. Russell, Stimulated Raman Scattering in Hydrogen-Filled Hollow-Core Photonic Crystal Fiber, *Science (New York, N.Y.)* **298**, 399–402 (2002).

[19] A. Lombardini, V. Mytskaniuk, S. Sivankutty, E. R. Andresen, X. Chen, J. Wenger, M. Fabert, N. Joly, F. Louradour, A. Kudlinski, and H. Rigneault, High-Resolution Multimodal Flexible Coherent Raman Endoscope, *Light-Science & Applications* **7**, 10 (2018).

[20] A. D. Pryamikov, A. S. Biriukov, A. F. Kosolapov, V. G. Plotnichenko, S. L. Semjonov, and E. M. Dianov, Demonstration of a Waveguide Regime for a Silica Hollow - Core Microstructured Optical Fiber with a Negative Curvature of the Core Boundary in the Spectral Region > 3.5 Mm, *Optics Express* **19**, 1441–1448 (2011).

[21] A. Kudlinski, A. Cassez, O. Vanvincq, D. Septier, A. Pastre, R. Habert, K. Baudelle, M. Douay, V. Mytskaniuk, V. Tsvirkun, H. Rigneault, and G. Bouwmans, Double

Clad Tubular Anti-Resonant Hollow Core Fiber for Nonlinear Microendoscopy, *Optics Express* **28**, 15062–15070 (2020).

[22] D. Septier, V. Mytskaniuk, R. Habert, D. Labat, K. Baudelle, A. Cassez, G. Brévalle-Wasilewski, M. Conforti, G. Bouwmans, H. Rigneault, H. Rigneault, and A. Kudlinski, Label-Free Highly Multimodal Nonlinear Endoscope, *Optics Express* **30**, 25020–25033 (2022).

[23] S. W. Hell, K. Bahlmann, M. Schrader, A. Soini, H. M. Malak, I. Gryczynski, and J. R. Lakowicz, Three-Photon Excitation in Fluorescence Microscopy, *Journal of Biomedical Optics* **1**, 71–74 (1996).

[24] D. L. Wokosin, V. E. Centonze, S. Crittenden, and J. White, Three-Photon Excitation Fluorescence Imaging of Biological Specimens Using an All-Solid-State Laser, *Bioimaging* **4**, 208–214 (1996).

[25] C. Xu, W. Zipfel, J. B. Shear, R. M. Williams, and W. W. Webb, Multiphoton Fluorescence Excitation: New Spectral Windows for Biological Nonlinear Microscopy, *Proceedings of the National Academy of Sciences* **93**, 10763–10768 (1996).

[26] C. Xu and W. W. Webb, Measurement of Two-Photon Excitation Cross Sections of Molecular Fluorophores with Data from 690 to 1050 Nm, *JOSA B* **13**, 481–491 (1996).

[27] P. Theer, M. T. Hasan, and W. Denk, Two-Photon Imaging to a Depth of 1000 Mm in Living Brains by Use of a Ti:Al_2O_3 Regenerative Amplifier, *Optics Letters* **28**, 1022–1024 (2003).

[28] D. G. Ouzounov, T. Wang, M. Wang, D. D. Feng, N. G. Horton, J. C. Cruz-Hernández, Y.-T. Cheng, J. Reimer, A. S. Tolias, N. Nishimura, and C. Xu, In Vivo Three-Photon Imaging of Activity of GCaMP6-labeled Neurons Deep in Intact Mouse Brain, *Nature Methods* **14**, 388–390 (2017).

[29] T. Wang, D. G. Ouzounov, C. Wu, N. G. Horton, B. Zhang, C.-H. Wu, Y. Zhang, M. J. Schnitzer, and C. Xu, Three-Photon Imaging of Mouse Brain Structure and Function through the Intact Skull, *Nature Methods* **15**, 789–792 (2018).

[30] M. Yildirim, H. Sugihara, P. T. C. So, and M. Sur, Functional Imaging of Visual Cortical Layers and Subplate in Awake Mice with Optimized Three-Photon Microscopy, *Nature Communications* **10**, 177 (2019).

[31] A. Klioutchnikov, D. J. Wallace, M. H. Frosz, R. Zeltner, J. Sawinski, V. Pawlak, K.-M. Voit, P. S. J. Russell, and J. N. D. Kerr, Three-Photon Head-Mounted Microscope for Imaging Deep Cortical Layers in Freely Moving Rats, *Nature Methods* **17**, 509–513 (2020).

[32] T. Wang, T. Wang, and C. Xu, Three-Photon Neuronal Imaging in Deep Mouse Brain, *Optica* **7**, 947–960 (2020).

[33] B. I. Hirschowitz, L. E. Curtiss, C. W. Peters, and H. M. Pollard, Demonstration of a New Gastroscope, the “Fiberscope”, *Gastroenterology* **35**, 50–53 (1958).

[34] M. Göppert-Mayer, Über Elementarakte Mit Zwei Quantensprüngen, *Annalen der Physik* **401**, 273–294 (1931).

[35] A. Lombardini, Nonlinear Optical Endoscopy with Micro-Structured Photonic Crystal Fibers, Aix-Marseille Université (2016).

[36] V. I. Mytskaniuk, Endoscopie Non-Linéaire : Instrumentation et Applications, Aix-Marseille (2018).

[37] M. Strupler, A.-M. Pena, M. Hernest, P.-L. Tharaux, J.-L. Martin, E. Beaurepaire, and M.-C. Schanne-Klein, Second Harmonic Imaging and Scoring of Collagen in Fibrotic Tissues, *Optics Express* **15**, 4054–4065 (2007).

[38] S. V. Plotnikov, A. C. Millard, P. J. Campagnola, and W. A. Mohler, Characterization of the Myosin-Based Source for Second-Harmonic Generation from Muscle Sarcomeres, *Biophysical Journal* **90**, 693–703 (2006).

[39] D. A. Dombeck, K. A. Kasischke, H. D. Vishwasrao, M. Ingelsson, B. T. Hyman, and W. W. Webb, Uniform Polarity Microtubule Assemblies Imaged in Native Brain Tissue by Second-Harmonic Generation Microscopy, *Proceedings of the National Academy of Sciences* **100**, 7081–7086 (2003).

[40] D. Débarre, W. Supatto, A.-M. Pena, A. Fabre, T. Tordjmann, L. Combettes, M.-C. Schanne-Klein, and E. Beaurepaire, Imaging Lipid Bodies in Cells and Tissues Using Third-Harmonic Generation Microscopy, *Nature Methods* **3**, 47–53 (2006).

[41] R. Genthial, E. Beaurepaire, M.-C. Schanne-Klein, F. Peyrin, D. Farlay, C. Olivier, Y. Bala, G. Boivin, J.-C. Vial, D. Débarre, and A. Gourrier, Label-Free Imaging of Bone Multiscale Porosity and Interfaces Using Third-Harmonic Generation Microscopy, *Scientific Reports* **7**, 3419 (2017).

[42] S. Saint-Jalm, Sources Optiques Fibrées Solitoniques Pour La Spectroscopie et La Microscopie Non Linéaires, Aix-Marseille (2014).

[43] S. Brustlein, P. Ferrand, N. Walther, S. Brasselet, C. Billaudeau, D. Marguet, and H. Rigneault, Optical Parametric Oscillator-Based Light Source for Coherent Raman Scattering Microscopy: Practical Overview, *Journal of Biomedical Optics* **16**, 021106 (2011).

[44] J.-X. Cheng, L. D. Book, and X. S. Xie, Polarization Coherent Anti-Stokes Raman Scattering Microscopy, *Optics Letters* **26**, 1341–1343 (2001).

[45] A. Volkmer, L. D. Book, and X. S. Xie, Time-Resolved Coherent Anti-Stokes Raman Scattering Microscopy: Imaging Based on Raman Free Induction Decay, *Applied Physics Letters* **80**, 1505–1507 (2002).

[46] F. Ganikhanov, C. L. Evans, B. G. Saar, and X. S. Xie, High-Sensitivity Vibrational Imaging with Frequency Modulation Coherent Anti-Stokes Raman Scattering (FM CARS) Microscopy, *Optics Letters* **31**, 1872–1874 (2006).

[47] E. O. Potma, C. L. Evans, and X. S. Xie, Heterodyne Coherent Anti-Stokes Raman Scattering (CARS) Imaging, *Optics Letters* **31**, 241–243 (2006).

[48] FPbase : The Fluorescent Protein Database, https://www.fpbase.org/.

[49] E. F. Schubert, Light-Emitting Diodes, Cambridge University Press, Cambridge, second edition, (2006).

[50] Optical fibers and optical fiber cables, https://sumitomoelectric.com/products/optical-fibers-and-optical-fiber-cables.

[51] G. Agrawal, Appendix B - Numerical Code for the NLS Equation, in G. Agrawal, editor, *Nonlinear Fiber Optics (Fifth Edition)*, Optics and Photonics, pages 615–617, Academic Press, Boston, fifth edition edition, (2013).

[52] F. Akhoundi, Y. Qin, N. Peyghambarian, J. K. Barton, and K. Kieu, Compact Fiber-Based Multi-Photon Endoscope Working at 1700 Nm, *Biomedical Optics Express* **9**, 2326–2335 (2018).

[53] O. E. Martinez, J. P. Gordon, and R. L. Fork, Negative Group-Velocity Dispersion Using Refraction, *JOSA A* **1**, 1003–1006 (1984).

[54] M. T. Myaing, D. J. MacDonald, and X. Li, Fiber-Optic Scanning Two-Photon Fluorescence Endoscope, *Optics Letters* **31**, 1076 (2006).

[55] D. R. Rivera, C. M. Brown, D. G. Ouzounov, I. Pavlova, D. Kobat, W. W. Webb, and C. Xu, Compact and Flexible Raster Scanning Multiphoton Endoscope Capable of Imaging Unstained Tissue, *Proceedings of the National Academy of Sciences* **108**, 17598–17603 (2011).

[56] E. Treacy, Optical Pulse Compression with Diffraction Gratings, *IEEE Journal of Quantum Electronics* **5**, 454–458 (1969).

[57] R. L. Fork, O. E. Martinez, and J. P. Gordon, Negative Dispersion Using Pairs of Prisms, *Optics Letters* **9**, 150–152 (1984).

[58] S. W. Clark, F. Ö. Ilday, and F. W. Wise, Fiber Delivery of Femtosecond Pulses from a Ti:Sapphire Laser, *Optics Letters* **26**, 1320–1322 (2001).

[59] C. Lefort, Transport d'impulsions Femtosecondes Par Fibres Optiques Pour Des Applications à La Biophotonique, Université de Limoges, (2012).

[60] P. Tournois, New Diffraction Grating Pair with Very Linear Dispersion for Laser Pulse Compression, *Electronics Letters* **29**, 1414–1415 (1993).

[61] S. Kane and J. Squier, Grism-Pair Stretcher–Compressor System for Simultaneous Second- and Third-Order Dispersion Compensation in Chirped-Pulse Amplification, *JOSA B* **14**, 661–665 (1997).

[62] E. A. Gibson, D. M. Gaudiosi, H. C. Kapteyn, R. Jimenez, S. Kane, R. Huff, C. Durfee, and J. Squier, Efficient Reflection Grisms for Pulse Compression and Dispersion Compensation of Femtosecond Pulses, *Optics Letters* **31**, 3363–3365 (2006).

[63] A. Ibrahim, F. Poulon, R. Habert, C. Lefort, A. Kudlinski, and D. A. Haidar, Characterization of Fiber Ultrashort Pulse Delivery for Nonlinear Endomicroscopy, *Optics Express* **24**, 12515–12523 (2016).

[64] W. Liang, G. Hall, B. Messerschmidt, M.-J. Li, and X. Li, Nonlinear Optical Endomicroscopy for Label-Free Functional Histology in Vivo, *Light: Science & Applications* **6**, e17082–e17082 (2017).

[65] C. Lefort, M. Kalashyan, G. Ducourthial, T. Mansuryan, R. P. O'Connor, and F. Louradour, Sub-30-Fs Pulse Compression and Pulse Shaping at the Output of a 2-m-Long Optical Fiber in the near-Infrared Range, *JOSA B* **31**, 2317–2324 (2014).

[66] C. Xu and F. W. Wise, Recent Advances in Fibre Lasers for Nonlinear Microscopy, *Nature Photonics* **7**, 875–882 (2013).

[67] S. Saint-Jalm, E. R. Andresen, P. Ferrand, A. Bendahmane, A. Mussot, O. Vanvincq, G. Bouwmans, A. Kudlinski, and H. Rigneault, Fiber-Based Ultrashort Pulse Delivery for Nonlinear Imaging Using High-Energy Solitons, *Journal of Biomedical Optics* **19**, 086021 (2014).

[68] M. Lelek, E. Suran, F. Louradour, A. Barthelemy, B. Viellerobe, and F. Lacombe, Coherent Femtosecond Pulse Shaping for the Optimization of a Non-Linear Micro-Endoscope, *Optics Express* **15**, 10154–10162 (2007).

[69] W. Piyawattanametha, E. D. Cocker, L. D. Burns, R. P. J. Barretto, J. C. Jung, H. Ra, O. Solgaard, and M. J. Schnitzer, *In Vivo* Brain Imaging Using a Portable 2.9 g Two-Photon Microscope Based on a Microelectromechanical Systems Scanning Mirror, *Optics Letters* **34**, 2309–2311 (2009).

[70] W. Zong, R. Wu, M. Li, Y. Hu, Y. Li, J. Li, H. Rong, H. Wu, Y. Xu, Y. Lu, H. Jia, M. Fan, Z. Zhou, Y. Zhang, A. Wang, L. Chen, and H. Cheng, Fast High-Resolution Miniature Two-Photon Microscopy for Brain Imaging in Freely Behaving Mice, *Nature Methods* **14**, 713–719 (2017).

[71] H. Mehidine, H. Mehidine, L. Pinot, M. Li, M. Li, F. Bouvet, C. Esnault, H. Xie, D. A. Haidar, and D. A. Haidar, An in vivo two photon fluorescence endomicroscopic probe based on a 2-axis electrothermal MEMS mirror, in *Clinical and Preclinical Optical Diagnostics II (2019), Paper 11079_14*, 11079_14, Optica Publishing Group, (2019).

[72] G. J. Tearney, R. H. Webb, and B. E. Bouma, Spectrally Encoded Confocal Microscopy, *Optics Letters* **23**, 1152 (1998).

[73] G. J. Tearney, M. Shishkov, and B. E. Bouma, Spectrally Encoded Miniature Endoscopy, *Optics Letters* **27**, 412 (2002).

[74] D. Yelin, B. E. Bouma, N. Iftimia, and G. J. Tearney, Three-Dimensional Spectrally Encoded Imaging, *Optics Letters* **28**, 2321–2323 (2003).

[75] D. Yelin, I. Rizvi, W. M. White, J. T. Motz, T. Hasan, B. E. Bouma, and G. J. Tearney, Three-Dimensional Miniature Endoscopy, *Nature* **443**, 765–765 (2006).

[76] E. J. Seibel, Q. Y. J. Smithwick, J. A. Myers, R. S. Johnston, and C. D. Melville, Compact scanning fiber device, (US20080249369A1), (2008).

[77] C. J. Engelbrecht, R. S. Johnston, E. J. Seibel, and F. Helmchen, Ultra-Compact Fiber-Optic Two-Photon Microscope for Functional Fluorescence Imaging in Vivo, *Optics Express* **16**, 5556–5564 (2008).

[78] E. Seibel, X. Li, and X. Liu, Optical fiber scanner for performing multimodal optical imaging, (US7616986B2), (2009).

[79] Y. Zhao, H. Nakamura, and R. J. Gordon, Development of a Versatile Two-Photon Endoscope for Biological Imaging, *Biomedical Optics Express* **1**, 1159–1172 (2010).

[80] Y. Zhang, M. L. Akins, K. Murari, J. Xi, M.-J. Li, K. Luby-Phelps, M. Mahendroo, and X. Li, A Compact Fiber-Optic SHG Scanning Endomicroscope and Its Application to Visualize Cervical Remodeling during Pregnancy, *Proceedings of the National Academy of Sciences* **109**, 12878–12883 (2012).

[81] G. Ducourthial, Développement d'un Endomicroscope Multiphotonique Compact et Flexible Pour l'imagerie in Vivo Haute Résolution de Tissus Biologiques Non Marqués, Limoges (2014).

[82] C.-H. Hage, P. Leclerc, M. Fabert, S. M. Bardet, J. Brevier, G. Ducourthial, T. Mansuryan, A. Leray, A. Kudlinski, and F. Louradour, A Readily Usable Two-Photon Fluorescence Lifetime Microendoscope, *Journal of Biophotonics* **12**, e201800276 (2019).

[83] W. Wadsworth, R. Percival, G. Bouwmans, J. Knight, T. Birks, T. Hedley, and P. Russell, Very High Numerical Aperture Fibers, *IEEE Photonics Technology Letters* **16**, 843–845 (2004).

[84] J. D. Shephard, J. D. C. Jones, D. P. Hand, G. Bouwmans, J. C. Knight, P. S. J. Russell, and B. J. Mangan, High Energy Nanosecond Laser Pulses Delivered Single-Mode through Hollow-Core PBG Fibers, *Optics Express* **12**, 717–723 (2004).

[85] Y. Y. Wang, X. Peng, M. Alharbi, C. F. Dutin, T. D. Bradley, F. Gérôme, M. Mielke, T. Booth, and F. Benabid, Design and Fabrication of Hollow-Core Photonic Crystal Fibers for High-Power Ultrashort Pulse Transportation and Pulse Compression, *Optics Letters* **37**, 3111–3113 (2012).

[86] J. C. Knight, T. A. Birks, P. S. J. Russell, and D. M. Atkin, All-Silica Single-Mode Optical Fiber with Photonic Crystal Cladding, *Optics Letters* **21**, 1547–1549 (1996).

[87] J. C. Knight, J. Broeng, T. A. Birks, and P. S. J. Russell, Photonic Band Gap Guidance in Optical Fibers, *Science* **282**, 1476–1478 (1998).

[88] F. Couny, F. Benabid, P. J. Roberts, P. S. Light, and M. G. Raymer, Generation and Photonic Guidance of Multi-Octave Optical-Frequency Combs, *Science* **318**, 1118–1121 (2007).

[89] P. J. Roberts, F. Couny, H. Sabert, B. J. Mangan, D. P. Williams, L. Farr, M. W. Mason, A. Tomlinson, T. A. Birks, J. C. Knight, and P. S. J. Russell, Ultimate Low Loss of Hollow-Core Photonic Crystal Fibres, *Optics Express* **13**, 236–244 (2005).

[90] A. N. Kolyadin, G. K. Alagashev, A. D. Pryamikov, L. Mouradian, A. Zeytunyan, H. Toneyan, A. F. Kosolapov, and I. A. Bufetov, Negative Curvature Hollow-core

Fibers: Dispersion Properties and Femtosecond Pulse Delivery, *Physics Procedia* **73**, 59–66 (2015).

[91] B. Debord, A. Amsanpally, M. Chafer, A. Baz, M. Maurel, J. M. Blondy, E. Hugonnot, F. Scol, L. Vincetti, F. Gérôme, and F. Benabid, Ultralow Transmission Loss in Inhibited-Coupling Guiding Hollow Fibers, *Optica* **4**, 209–217 (2017).

[92] F. Couny, F. Benabid, and P. S. Light, Large-Pitch Kagome-Structured Hollow-Core Photonic Crystal Fiber, *Optics Letters* **31**, 3574–3576 (2006).

[93] F. Benabid and P. J. Roberts, Linear and Nonlinear Optical Properties of Hollow Core Photonic Crystal Fiber, *Journal of Modern Optics* **58**, 87–124 (2011).

[94] C. Wei, R. J. Weiblen, C. R. Menyuk, and J. Hu, Negative Curvature Fibers, *Advances in Optics and Photonics* **9**, 504–561 (2017).

[95] M. A. Duguay, Y. Kokubun, T. L. Koch, and L. Pfeiffer, Antiresonant Reflecting Optical Waveguides in SiO2-Si Multilayer Structures, *Applied Physics Letters* **49**, 13–15 (1986).

[96] F. Yu, M. Xu, and J. C. Knight, Experimental Study of Low-Loss Single-Mode Performance in Anti-Resonant Hollow-Core Fibers, *Optics Express* **24**, 12969–12975 (2016).

[97] B. Debord, M. Alharbi, T. Bradley, C. Fourcade-Dutin, Y. Y. Wang, L. Vincetti, F. Gérôme, and F. Benabid, Hypocycloid-Shaped Hollow-Core Photonic Crystal Fiber Part I: Arc Curvature Effect on Confinement Loss, *Optics Express* **21**, 28597–28608 (2013).

[98] F. Gérôme, R. Jamier, J.-L. Auguste, G. Humbert, and J.-M. Blondy, Simplified Hollow-Core Photonic Crystal Fiber, *Optics Letters* **35**, 1157–1159 (2010).

[99] Y. Wang, M. I. Hasan, M. R. A. Hassan, and W. Chang, Effect of the Second Ring of Antiresonant Tubes in Negative-Curvature Fibers, *Optics Express* **28**, 1168–1176 (2020).

[100] Y. Y. Wang, F. Couny, P. J. Roberts, and F. Benabid, Low loss broadband transmission in optimized core-shape Kagome hollow-core PCF, in *CLEO/QELS: 2010 Laser Science to Photonic Applications*, pages 1–2, (2010).

[101] P. Uebel, M. C. Günendi, M. H. Frosz, G. Ahmed, N. N. Edavalath, J.-M. Ménard, and P. S. J. Russell, Broadband Robustly Single-Mode Hollow-Core PCF by Resonant Filtering of Higher-Order Modes, *Optics Letters* **41**, 1961–1964 (2016).

[102] W. Ding, Y.-Y. Wang, S.-F. Gao, M.-L. Wang, and P. Wang, Recent Progress in Low-Loss Hollow-Core Anti-Resonant Fibers and Their Applications, *IEEE Journal of Selected Topics in Quantum Electronics* **26**, 1–12 (2020).

[103] Y. Wang and W. Ding, Confinement Loss in Hollow-Core Negative Curvature Fiber: A Multi-Layered Model, *Optics Express* **25**, 33122–33133 (2017).

[104] L. Vincetti and L. Rosa, A Simple Analytical Model for Confinement Loss Estimation in Hollow-Core Tube Lattice Fibers, *Optics Express* **27**, 5230–5237 (2019).

[105] M. Tateda, N. Shibata, and S. Seikai, Interferometric Method for Chromatic Dispersion Measurement in a Single-Mode Optical Fiber, *IEEE Journal of Quantum Electronics* **17**, 404–407 (1981).

[106] P. Ferrand, J. Wenger, A. Devilez, M. Pianta, B. Stout, N. Bonod, E. Popov, and H. Rigneault, Direct Imaging of Photonic Nanojets, *Optics Express* **16**, 6930–6940 (2008).

[107] P. Ghenuche, H. Rigneault, and J. Wenger, Photonic Nanojet Focusing for Hollow-Core Photonic Crystal Fiber Probes, *Applied Optics* **51**, 8637–8640 (2012).

[108] K. Iga, Theory for Gradient-Index Imaging, *Applied Optics* **19**, 1039–1043 (1980).

[109] T. Hansson, A. Tonello, T. Mansuryan, F. Mangini, M. Zitelli, M. Ferraro, A. Niang, R. Crescenzi, S. Wabnitz, S. Wabnitz, and V. Couderc, Nonlinear Beam Self-Imaging and Self-Focusing Dynamics in a GRIN Multimode Optical Fiber: Theory and Experiments, *Optics Express* **28**, 24005–24021 (2020).

[110] M. Guizar-Sicairos and J. C. Gutiérrez-Vega, Computation of Quasi-Discrete Hankel Transforms of Integer Order for Propagating Optical Wave Fields, *JOSA A* **21**, 53–58 (2004).

[111] D. Gloge and E. A. J. Marcatili, Multimode Theory of Graded-Core Fibers, *The Bell System Technical Journal* **52**, 1563–1578 (1973).

[112] E. Pshenay-Severin, H. Bae, K. Reichwald, G. Matz, J. Bierlich, J. Kobelke, A. Lorenz, A. Schwuchow, T. Meyer-Zedler, M. Schmitt, B. Messerschmidt, and J. Popp, Multimodal Nonlinear Endomicroscopic Imaging Probe Using a Double-Core Double-Clad Fiber and Focus-Combining Micro-Optical Concept, *Light: Science & Applications* **10**, 207 (2021).

[113] D. Huland, K. Charan, D. Ouzounov, J. Jones, N. Nishimura, and C. Xu, Three-Photon Excited Fluorescence Imaging of Unstained Tissue Using a GRIN Lens Endoscope, *Biomedical Optics Express* **4**, 652–658 (2013).

[114] I. Raymond, A. Vila, U.-C. Huynh, and N. Brecha, Cyan Fluorescent Protein Expression in Ganglion and Amacrine Cells in a Thy1-CFP Transgenic Mouse Retina, *Molecular vision* **14**, 1559–74 (2008).

[115] T. Vardi, M. Fina, L. Zhang, A. Dhingra, and N. Vardi, mGluR6 Transcripts in Non-neuronal Tissues, *The journal of histochemistry and cytochemistry : official journal of the Histochemistry Society* **59**, 1076–86 (2011).

[116] A. Lombardini, E. R. Andresen, A. Kudlinski, I. Rimke, and H. Rigneault, Origin and Suppression of Parasitic Signals in Kagomé Lattice Hollow Core Fibers Used for SRS Microscopy and Endoscopy, *Optics Letters* **42**, 1824–1827 (2017).

[117] L. Wang, H. Y. Choi, Y. Jung, B. H. Lee, and K.-T. Kim, Optical Probe Based on Double-Clad Optical Fiber for Fluorescence Spectroscopy, *Optics Express* **15**, 17681–17689 (2007).

[118] S.-Y. Ryu, H.-Y. Choi, M.-J. Ju, J.-H. Na, W.-J. Choi, and B.-H. Lee, The Development of Double Clad Fiber and Double Clad Fiber Coupler for Fiber Based Biomedical Imaging Systems, *Journal of the Optical Society of Korea* **13**, 310–315 (2009).

[119] H. Bao, S. Y. Ryu, B. H. Lee, W. Tao, and M. Gu, Nonlinear Endomicroscopy Using a Double-Clad Fiber Coupler, *Optics Letters* **35**, 995–997 (2010).

[120] S. Lemire-Renaud, M. Rivard, M. Strupler, D. Morneau, F. Verpillat, X. Daxhelet, N. Godbout, and C. Boudoux, Double-Clad Fiber Coupler for Endoscopy, *Optics Express* **18**, 9755–9764 (2010).

[121] W.-J. Madore, E. D. Montigny, O. Ouellette, S. Lemire-Renaud, M. Leduc, X. Daxhelet, N. Godbout, and C. Boudoux, Asymmetric Double-Clad Fiber Couplers for Endoscopy, *Optics Letters* **38**, 4514–4517 (2013).

[122] E. D. Montigny, W.-J. Madore, O. Ouellette, G. Bernard, M. Leduc, M. Strupler, C. Boudoux, and N. Godbout, Double-Clad Fiber Coupler for Partially Coherent Detection, *Optics Express* **23**, 9040–9051 (2015).

[123] A. Lukic, S. Dochow, H. Bae, G. Matz, I. Latka, B. Messerschmidt, M. Schmitt, and J. Popp, Endoscopic Fiber Probe for Nonlinear Spectroscopic Imaging, *Optica* **4**, 496–501 (2017).

[124] M. Koshiba, K. Hayata, and M. Suzuki, Approximate Scalar Finite-Element Analysis of Anisotropic Optical Waveguides, *Electronics Letters* **18**, 411–413 (1982).